Dissertation zur Erlangung des Doktorgrades
der Fakultät für Chemie und Pharmazie
der Ludwig-Maximilians-Universität München

Mechanistic Investigation of Eukaryotic Quality Control Factors RQT and Mbf1

Katharina Marion Best
aus
Dachau, Deutschland

2023

Erklärung

Diese Dissertation wurde im Sinne von § 7 der Promotionsordnung vom 28. November 2011 von Herrn Prof. Dr. Roland Beckmann betreut.

Eidesstattliche Versicherung

Diese Dissertation wurde eigenständig und ohne unerlaubte Hilfe erarbeitet.

München, 13.12.2022 _____

(Katharina Best)

Dissertation eingereicht am: 23.01.2023

1. Gutachter: Prof. Dr. Roland Beckmann

2. Gutachter: Prof. Dr. Klaus Förstemann

Mündliche Prüfung am: 27.04.2023

List of publications

EDF1 coordinates cellular responses to ribosome collisions

Niladri K Sinha*, Alban Ordureau*, Katharina Best*, James A Saba, Boris Zinshteyn, Elayanambi Sundaramoorthy, Amit Fulzele, Danielle M Garshott, Timo Denk, Matthias Thoms, Joao A Paulo, J Wade Harper, Eric J Bennett, Roland Beckmann, Rachel Green

eLife 2020 9:e58828; doi: https://doi.org/10.7554/eLife.58828

Clearing of ribosome collisions by the ribosome quality control trigger complex RQT

Katharina Best, Ken Ikeuchi, Lukas Kater, Daniel Best, Joanna Musial, Yoshitaka Matsuo, Otto Berninghausen, Thomas Becker, Toshifumi Inada, Roland Beckmann

Nat Commun 14, 921 (2023). https://doi.org/10.1038/s41467-023-36230-8

* These authors contributed equally to this work.

Summary

Translation is a central cellular process and thus tightly regulated by quality control mechanisms. Monitoring the ribosome during translation is an elegant way to track the progress and to catch a variety of errors before they lead to detrimental effects in the cell. Recently, ribosomal collisions have emerged as a trigger for such quality control pathways, and various collision sensors have been identified. One of those pathways called ribosome associated quality control (RQC) deals with ribosomes stuck on an open reading frame (e.g. due to stable mRNA structures or inhibitory codons). Here, ubiquitination of ribosomal proteins serves as a signal for dissociation of the stuck ribosome by the RQC-trigger (RQT) complex. Subsequently the aberrant mRNA and the truncated nascent peptide are degraded and intact components such as ribosomal subunits or tRNAs can be recycled. Although this pathway has been studied in detail over the last years, the exact mechanism by which RQT leads to dissociation of stalled ribosomes remains unclear.

This thesis aimed to elucidate the RQT-mediated dissociation mechanism by setting up an *in vitro* splitting system and subsequent cryo-EM analysis of the splitting reactions. To generate suitable substrates for the dissociation process, collisions were generated using known ribosome stalling sequences in a cell free *in vitro* translation system. Splitting assays showed that an *in vitro* ubiquitination step for collided ribosomes is crucial for splitting. Moreover, such assays revealed that efficient splitting is dependent on ATPase activity of the N-terminal helicase cassette of RQT component Slh1, on the presence of a neighboring ribosome and on availability of a 3' mRNA overhang. Structural analysis of the ribosome-bound RQT complex divulged stable positioning of RQT on the lead ribosome of a collided 'disome' unit, as well as on 80S and 40S. The 80S-RQT complex was observed in two different states located in close proximity to the entry of the mRNA channel. Together with the observed requirement of available 3'mRNA and helicase activity of Slh1, this suggests that Slh1 can pull on the mRNA, leading to an initial model for ribosome dissociation.

Ribosome stalling and subsequent collisions increase the probability of frameshifting and thus translation of an aberrant protein. Structural analysis of three collided ribosomes, so called trisomes, revealed the presence of multiprotein bridging factor (Mbf1), previously identified as a frameshift inhibitor. This small protein was found on the second and third colliding ribosomes, positioned between beak and body of the 40S subunit. Comparison with the human homolog EDF1, which was found to be recruited to emetine induced collisions, showed that those proteins bind in the exact same fashion. The position on the 40S subunit of the collided ribosomes suggests that both proteins interact directly with the mRNA to prevent frameshifting, probably in combination with preventing conformational changes required for translocation of the ribosome.

In conclusion, high resolution cryo-EM structures of both RQT and Mbf1 on ribosomes enabled detailed insights into the intricate quality control network targeting collisions in the cell. From this, molecular models for both a helicase driven dissociation mechanism by RQT and the frameshifting inhibition by Mbf1 could be derived. These results, together with the developed optimization strategies, provide the basis for future works, leading to a detailed understanding of these pathways.

Contents

Table of Abbreviations

AAP	arginine attenuator peptide
ADP	adenosine diphosphate
A-site	aminoacyl site
ATP	adenosine triphosphate
CCD	charge coupled device
CMOS	complementary metal oxide semiconductor
CP	central protuberance
cryo-EM	cryogenic electron microscopy
cryo-ET	cryogenic electron tomography
CTC	C-terminal cassette
CTF	contrast transfer function
CUE	coupling ubiquitin to ER degradation
DED	direct electron detector
DNA	deoxyribonucleic acid
ER	endoplasmatic reticulum
E-site	exit site
FEG	field emission gun
FSC	Fourier shell correlation
GAC	GTPase-associated center
GSFSC	gold standard FSC
GTP	guanosine triphosphate
HhH	helix-hairpin-helix
HTH	helix-turn-helix
IF	initiation factor
ISR	integrated stress response
LSU	large subunit
mRNA	messenger RNA
NC	nascent chain
NGD	no-go decay
NMD	nonsense mediated decay
NMR	nuclear magnetic resonance

NSD	no-stop decay
NTC	N-terminal cassette
NTP	nucleoside triphosphate
NTR	N-terminal region
ORF	open reading frame
PBS	phosphate-buffered saline
PDB	protein database
PIC	pre-initiation complex
POST	post-translocation
PRE	pre-translocation
P-site	peptidyl site
PTC	peptidyl-transfer center
PVDF	polyvinylidene difluoride
RING	really interesting new gene
RNA	ribonucleic acid
RNC	ribosome nascent chain complex
RQC	ribosome associated quality control
RQT	RQC trigger
rRNA	ribosomal RNA
RSR	ribotoxic stress response
SDS	sodium dodecyl sulfate
SDS-PAGE	SDS polyacrylamide gel electrophoresis
SNR	signal-to-noise ratio
SPA	single particle analysis
SRP	signal recognition particle
SSU	small subunit
TBS	tris-buffered saline
tRNA	transfer RNA
WH	winged helix
wt	wild type
ZnF	zinc-finger

List of Figures

Introduction

The relationship between structure and function of molecules can be used to gain a better understanding of biological processes: Direct visualization of molecular structures often allows us to deduct information about the underlying mechanisms. To understand fundamental processes in the cell, such as translation, mechanistic insights are invaluable and historically go hand in hand with the development of methods for structural determination. This is reflected by the sheer amount of related Nobel prizes in the last 120 years. For the development of methods which enable structure determination, 11 Nobel prizes have been awarded so far, and many more for projects that subsequently applied these methods to make fundamental discoveries. At the moment, there are three main techniques for structure determination: X-ray crystallography, NMR-spectroscopy and cryogenic-electron microscopy (cryo-EM).

Cryo Electron Microscopy

Undoubtedly, X-ray crystallography has been the most efficient way of analyzing structures in detail for most of the 20th century. As of now (2022), more than 168,000 structures solved by crystallography have been deposited at the central protein database (PDB), compared to only around 12,000 for cryo-EM. However, recent advances in the field of cryo-EM, especially the ability to obtain higher resolutions and broader applicability combined with higher throughput, vastly increased its popularity. Cryo-EM has some advantages compared to X-ray crystallography. One is the independence of determining growing conditions for crystals and therefore often the smaller necessary amount of purified sample. Other advantages include the less stringent required sample purity and the ability to observe multiple states per sample. Nevertheless, sample preparation in cryo-EM comes with its own challenges and pitfalls (see below). With modern methods in electron microscopy, it is possible to observe complexes in a more native environment (single particle analysis, SPA) and very recently also in the native cellular environment (cryo-ET). With increasing computational power and faster data collection, the purity of the sample is getting less and less significant. Although an optimal sample will still have a high degree of homogeneity (e.g. consists mostly of ribosomes), it is possible to capture and distinguish snapshots of multiple conformationally or compositionally distinct states.

Sample preparation

To obtain a sample of decent homogeneity, purification steps need to be performed. A sample can be generated by tagging endogenous proteins of interest, or overexpression of tagged recombinant proteins, which either form stable complexes that are purified together, or can be assembled *in vitro* in reconstitutions. Often, extensive efforts have to be made to optimize this procedure in order to obtain and stabilize the optimal, biologically relevant state of a sample.

If the reactions of interest involve transient interactions, they might need fixing by chemical crosslinking (e.g. GraFix) or in the case of nucleotide dependent reactions, employing non-hydrolysable, or transition state NTP analogs. For every given sample, this optimization process varies, making sample preparation a time consuming and challenging step (Weissenberger *et al.*, 2021).

Recording images of protein complexes in a transmission electron microscope (TEM) poses certain challenges due to the high vacuum in the TEM column and the radiation damage caused by the electron illumination (Marton, 1934). To address this, samples can either be embedded and dried in a heavy metal solution (e.g. uranyl acetate)(Horne, 1964; Ohi *et al*., 2004) or vitrified by plunge freezing in a cryogen (Dubochet *et al.*, 1988; J. Dubochet, 1981). While the first method gives high contrast and is independent of keeping the sample frozen, the staining and drying in heavy metal solution often leads to damage to the sample (e.g. flattening due to dehydration) or disintegration of complexes. Additionally, only the outside of the sample will be visible after staining, resulting in loss of information regarding the interior properties of a specimen. Nevertheless, negative staining is a quick and easy method, often employed for initial characterization of samples and important for optimizing sample preparation conditions, such as concentrations.

A more sophisticated approach protects the sample by freezing it in an aqueous environment, which can resemble the native conditions of a complex. To prevent the formation of crystalline ice, which would disrupt the protein structure, samples are rapidly cooled in liquid ethane or a propane/ethane mixture which has a high cooling rate. By plunge freezing, the sample is completely frozen in the range of milliseconds, forming a glass-like, amorphous, non-crystalline solid, also referred to as vitrious ice. For this vitrification process to be so fast and efficient, the sample is applied to plasma cleaned small metal discs (‘grids’), which only have a limited heat capacity, blotted into a thin film (usually 10-100 nm thick) before being plunged into the cryogen. Blotting of the sample to a thin film is needed to allow electrons to pass the sample without too much scattering in the subsequent data collection, but also helps to overcome the heat conductivity of water present in the sample, an otherwise limiting factor in the vitrification process. As their name implies, grids have a grate structure formed by conductive material (e.g. copper or gold) which is coated with a thin layer of perforated carbon or gold for support (Ermantraut *et al.*, 1998; Russo and Passmore, 2014). The holes in the support layer serve as the sites for image acquisition. Here, the electron beam will only encounter the present particles and vitrious ice. An optimal grid should have a uniform distribution of mono-disperse particles throughout the holes, however, this is dependent on sufficient concentration and overall sample properties. Often particles tend to stick rather to the support layer, than being optimally distributed over the holes. To improve the number of particles, present in the holes after sample preparation, a grid can have a very thin and therefore nearly electron transparent, continuous (2-3 nm) carbon film on top of the support. This helps with particle distribution but reduces image contrast due to increased background scattering.

To render the surface of such grids hydrophilic, a plasma cleaning step is usually employed (Dubochet *et al.*, 1971). Plasma is generated in a vacuum by ionization of a gas (e.g. air or argon). Upon interaction with the grid it renders the surface hydrophilic, leading to a more conform spread of the sample on the grid and a better blotting efficiency (Gan *et al.*, 2008). To enhance contrast, the thin carbon film can also be substituted by a (mono-)layer of graphene or graphene-oxide (Pantelic *et al*., 2021). After successful plunge freezing, samples can be stored in liquid nitrogen until they are analyzed in the microscope.

The vitrification of samples is an established process, but there are still common problems arising. There is a broad range of parameters that influence the sample preparation, such as concentration of the sample or buffer composition, but also subtler ones such as humidity and temperature at the time of grid preparation or the duration between glow-discharging, sample application and subsequent freezing. Although newer plunge freezers blot the grid automatically, therefore keeping force and time constant, and usually have a chamber for keeping temperature and humidity at a constant level, not all of these parameters can be perfectly controlled, affecting the reproducibility of samples. Another problem encountered during sample preparation is the accumulation of proteins at the air-water interface (Glaeser, 2018). This has mainly two effects: the increased concentration at the interface can lead to aggregation and degradation of the sample (James and Augenstein, 1966), or the molecules arrange themselves all in the same 'preferred' orientation (Lu *et al*., 1999). The last one is especially bad, since, from a limited number of different views, no meaningful 3D volumes can be reconstructed. Although this can be mitigated by the addition of detergents or using grids with a continuous support, using these might introduce yet different challenges regarding sample stability.

Newer approaches try to address such problems by employing inkjet-heads that can apply tiny amounts of sample on a falling grid or 'writing' samples onto a grid (Jain *et al*., 2012; Rima *et al., 2022)*. The essential idea is, to not only place the sample on a precise location on a grid, thereby in principle allowing the application of multiple samples, but also to reduce the sample volume and remove the need for blotting (Jain *et al.*, 2012; Razinkov *et al*., 2016). An additional effect would be the shorter exposure of the sample to the air-water interface which addresses the above-described issues. Recently, also self-blotting grids (Razinkov *et al.*, 2016) or affinity grids for direct sample purification (Kelly *et al.*, 2010) were reported. With these options becoming more wide-spread, samples that may have failed due to problems during sample preparation might get solvable by cryo-EM in the future.

Image formation

The schematics of an electron microscope are very similar to a standard light microscope (reviewed by Cheng *et al*., 2015; Orlova and Saibil, 2011). Instead of glass lenses focusing light waves, magnetic lenses focus or shape an electron beam. To prevent interaction of the electrons with gas ions, transmission electron microscopy needs to occur in vacuum. In the high-end setup, the electron beam is generated from a field emission gun (FEG). A tungsten crystal serves as a cathode at high negative voltage (200-300 kV) and is coupled to a magnetic field, which increases spatial coherence of the emitted electrons, resulting in a very bright electron beam. This beam is shaped by an arrangement of magnetic condenser lenses before it passes through the grid/sample. Behind the sample, there is another array of lenses, responsible for magnification and projection of the final image onto a detector (e.g., a fluorescent screen or a camera). When passing through the specimen, a subset of electrons interacts with the sample and is scattered.

Interaction without a change in energy is called elastic scattering, if energy is transferred to the sample, electrons are in-elastically scattered. The later especially contributes to noise in the obtained images and to the damage of the sample during measurements, by effects such as X-ray emission, ionization, destruction of chemical bonds and induction of secondary scattering. In the obtained image, the scattering of electrons gives rise to two different types of contrast: amplitude and phase contrast. Amplitude contrast is produced by loss of electrons. Too broadly elastically scattered and in-elastically scattered electrons do not pass the sample. Essentially, the sample is not transparent for these electrons, directly changing the amplitude of the emerging electron wave. However, biological molecules mostly consist of light atoms that do not absorb electrons in such a fashion, but rather deflect them, leading to a very weak contribution of amplitude contrast. A larger effect comes from elastic scattering, which leads to a small phase shift in the electron wave according to the coulomb potential distribution encountered within the sample. Such elastically scattered electrons then interfere with the un-scattered electrons, changing the measured amplitude and forming phase contrast. After passing the sample, the electrons pass through a lens, transforming the arriving plane wave into a spherical wave. Since there are no ideal lenses, there are multiple defects that distort the obtained image and have to be accounted for after imaging. Electrons passing the periphery of the lens are refracted stronger than ones passing through the middle, leading to slight differences in focal lengths, an effect called spherical aberration (Wade, 1992). Chromatic aberration is caused by a similar effect of the lens on electrons with different wavelengths (e.g. resulting from fluctuations in the electron source or inelastic scattering). Another effect that distorts the obtained image is astigmatism. Here, imperfections in the magnetic field of the lenses lead to an elongation of the beam in one direction. In total, these effects lead to a ‘blurring’ of the EM image compared to the real object encountered by the electron beam.

The contrast transfer function (CTF, or point spread function of which the CTF is the Fourier transform) describes the modification of an acquired image by such effects, especially considering defocus and spherical aberration (Zhu *et al.*, 1997), leading to amplitude modulations and phase reversals. These are visible as thon rings in power spectra (Thon, 1966). By estimating the CTF, one can calculate back to the 'real' sample that was encountered by the electron beam. The CTF for phase contrast is mathematically represented by a sine wave.

$$CTF(\lambda, g, \Delta f, C_s) = -\sin\left[\pi\lambda|g|^2\left(\Delta f - \frac{1}{2}\lambda^2|g|^2 C_s\right)\right] \qquad (1)$$

Where λ is the electron wavelength, g the spatial frequency vector, Δf the defocus and C_s the spherical aberration (Mindell and Grigorieff, 2003; Wade, 1992; Zhu *et al.*, 1997). The CTF describes the information content in terms of spatial frequency, which corresponds to the angle of scattering of the electrons. Low spatial frequencies correspond to low-resolution information (=rough shape of a particle), and high spatial frequencies to high-resolution information. The CTF starts at zero and then oscillates between positive and negative values. If the microscope had a perfect lens system and the sample would be imaged 'in focus' (Δf =0), the scattered electrons would encounter a 90 degrees' phase shift. Adding the scattered and un-scattered wave together does therefore not result in large changes in amplitude. Thus, in focus there is almost no phase information, which equals no information on the coulomb potential of the sample. Since we do not have perfect lenses (see spherical aberration described above) and due to effects such as inelastic scattering (amplitude contrast), there is still a residual weak contrast, but the CTF remains (very close to) zero for low spatial frequencies. Although in principle high-resolution information is present in the images, without the low-resolution information, no particles can be distinguished from the background. To increase the phase contrast, defocus can be applied. Physically, defocus changes the path length of the electrons through the microscope and thereby adds to the phase shift. At the same time, a higher defocus causes increased fluctuations of the CTF, which leads to more zero crossings, less robust estimations and thereby limits high-resolution information. There is a tradeoff between better overall contrast, which facilitates the discrimination of particles from the background, and obtaining high-resolution information. Due to the periodic nature of the wave function, for some spatial frequencies, the phase shift will always result in zero contrast, however changing defocus can shift these frequencies (Penczek, 2010a; Zhu *et al.*, 1997). In the end, reconstructions will contain particles from images with different defocus values, containing similar information at all special frequencies. In reality, higher frequencies show a weaker signal-to-noise ratio, an effect described by the envelope function (Chiu and Glaeser, 1977). Due to flaws in spatial and temporal coherence (imperfections in direction and energy of electrons), which affects high frequency components stronger than the low frequency ones, the CTF is dampened at higher frequencies, resulting in a resolution limit.

Overall, the image formed by the electron microscope resembles a 2D projection of the encountered 3D object along the electron path, taking into account both distortion of the image described by the CTF and a noise component. This linear relationship is central to most cryo-EM image reconstruction software, for Relion it was described as follows (Scheres, 2012a):

$$X_{ij} = CTF_{ij} \sum_{l=1}^{L} P_{jl}^{\phi} V_l + N_{ij} \qquad (2)$$

Where X_{ij} is the j^{th} (j = 1,…,J) component of the 2D Fourier transform of the i^{th} experimental image X_i (i = 1,…,N), CTF_{ij} is the corresponding CTF component, V_l is the l^{th} (l = 1,…,L) component of the 3D Fourier transform, P^{ϕ} is a J x L matrix of elements P_{jl}^{ϕ} and N_{ij} represents the corresponding noise. The operation $\sum_{l=1}^{L} P_{jl}^{\phi} V_l$ extracts a slice out of the Fourier transformed 3D structure, corresponding to the 2D projection of a 3D volume in real space (Scheres, 2012a). This relationship can later be used to reconstruct the encountered 3D object from the acquired 2D images (see Image processing).

Image acquisition

The theoretical resolution obtainable in cryo-EM is limited by the efficiency of the detector. While early data were recorded on photographic film (Downing and Grano, 1982; Zeitler, 1992), the use of charge coupled devices (CCD, (Brink and Chiu, 1994)) and recently, direct detection of electrons by complementary metal oxide semiconductor based detectors (CMOS) revolutionized cryo-EM (Deptuch *et al*., 2007; Faruqi *et al*., 2003; Milazzo *et al.*, 2005). Initially, electrons could not be detected directly due to the induced radiation damage on the sensors. Instead, they were first converted to photons via a scintillator (e.g., a phosphor screen) and then, via fiber optics, transferred to the detector itself. Increased robustness of the CMOS senor made the coupling to a scintillator unnecessary. This enabled the direct detection of electrons ("counting detectors") in the DEDs (Faruqi and McMullan, 2011; Milazzo *et al*., 2011). Recording of single electron detection events ('counting') decreases the SNR compared to the previously employed integrating mode and results in a better detective quantum efficiency (DQE) (McMullan *et al*., 2009).

For any given sensor, the obtainable resolution for a detector is restricted by the Nyquist limit: the smallest wavelength (highest spatial frequency) must be at least sampled twice, meaning with at least two pixels, resulting in a frequency cutoff at 1/(2*pixel size of the detector). However, newer sensors can overcome this limit by interpolation between neighboring pixels, enabling more precise detection ('super-resolution mode') (Booth, 2012; Li *et al*., 2013b). To enable proper electron counting, especially in 'super-resolution mode', the electron dose needs to be low, otherwise simultaneous detection of electrons too close to each other on the sensor will lower the DQE and thus the image contrast (Li *et al.*, 2013b; Ruskin *et al*., 2013).

However, to acquire an image with decent SNR, a certain dosage of electrons needs to be applied, resulting in longer exposure times. The problems arising from such a prolonged exposure such as drift and beam-induced motion can be solved by the separation of such acquisitions into many single frames, i.e. a movie, which can be averaged and aligned before further processing (See Image processing) (Brilot *et al.*, 2012; Campbell *et al*., 2012; Li *et al.*, 2013a).

For every particular sample (or collection) the imaging parameters can be optimized. The dose of electrons can be adjusted, however, the above-mentioned tradeoff between contrast and loss of high-resolution information due to radiation damage needs to be taken into account (Grant and Grigorieff, 2015). To obtain a more uniform distribution of particle views, data can be collected on tilted grids, improving the later reconstructions (Tan *et al.*, 2017). Last but not least, magnification can be adjusted. The magnification directly influences the pixel size of an obtained micrograph and thus the Nyquist resolution limit. However, although increased magnification also increases high-resolution signal, this comes at the price of a smaller field of view, leading to a decrease in the present number of particles for each micrograph (Feathers *et al*., 2021).

Image processing

To get from the obtained micrographs to a final 3D volume, many steps have to be undertaken. For all of these, a variety of different software solutions are available. For well-known samples, there are often established workflows and even some automated approaches. The next section gives a rough overview about the principle steps.

Motion correction and dose weighting.

To correct for radiation damage and movement of the sample during measurements, motion correction (Brilot *et al.*, 2012; Shigematsu and Sigworth, 2013) and dose weighting can be applied. Due to beam-induced motion of the sample and drift of the microscope, the exact position of a particle varies in between frames in a movie. After correction of this motion, the frames can be averaged, which leads to de-blurring of the image and increased SNR (Bai *et al*., 2013; Li *et al.*, 2013a; Zheng *et al*., 2017; Zivanov *et al*., 2019). While the first frames in the movie show the least radiation damage, due to the low amount of encountered electrons, at the same time the contrast in the sum of these frames is still weak. Later frames have stronger radiation damage, distorting high-resolution features of the sample but are still required to obtain micrographs with sufficient contrast. Dose weighting algorithms enable better information gain by down weighting the contribution of higher frequencies in later frames of one single movie (Scheres, 2014).

CTF estimation.

As described above, an image obtained by the microscope is modified by various effects during the projection process. These modifications are described by the CTF. Thus, it is necessary to model the CTF to get back to the 'real' image without distortions to then be able to solve structures at high-resolution. Since the main contributing effects are spherical aberration and defocus, where the former is constant for a given microscope, mainly the true defocus of an obtained image needs to be estimated individually. To obtain the closest estimation, a simulated model CTF (Mindell and Grigorieff, 2003; Rohou and Grigorieff, 2015; Zhang, 2016) is fitted to an image's power spectrum (Thon, 1966). With the obtained parameters, the 2D class averages and 3D reconstructions can be corrected for the effects of the CTF of the individual particles. In later processing steps (after obtaining homogenous 3D reconstructions), CTF parameters can then be refined to re-estimate defocus and astigmatism, either on a per-micrograph or a per-particle basis (Zivanov *et al*., 2018; Zivanov *et al*., 2020).

Particle picking

From the corrected micrographs, particles have to be picked for downstream structure determination. The first problem is identification of particles on the micrographs. For larger molecules this is easier since they produce more contrast, for smaller molecules the signal-to-noise-ratio is worse and thus they might be quite difficult to distinguish from the background. A large percentage of the available picking (and de-blurring) software uses low pass/high pass filters on the data to enhance contrast. One standard approach (especially for unknown samples) is to pick some particles manually, perform initial 2D classification and use the averages in a template-based picking approach. However, this can introduce a bias towards well visible views, while less distinguishable particle projections may be omitted. Alternatively, 'blob' pickers with a certain radius can be used, however they are less efficient if used on noisy or contaminated micrographs. Using template-based approaches, the user needs to be careful to avoid bias by the template. In case an overly detailed template is used, features of this template can be assembled even when only background noise is picked ('Einstein-from-noise') (Henderson, 2013). Newer approaches (such as crYOLO or Topaz (Bepler *et al*., 2019; Wagner *et al*., 2019)) employ neural networks for the template free identification of particles. After determination of particle locations (coordinates), particles are extracted with a square box, and normalized. The obtained particle stack can then be used in 2D classification.

2D Classification

2D classification is used to curate the picked particles, to get an initial impression of the data and if needed, to generate templates for optimized particle picking. Optimally, the picked particles are oriented randomly on the micrograph, providing various observed projections that cover all of the components of the 3D volume. While single particles have a bad SNR, the signal can be increased by comparing particle images and aligning and averaging similar ones, enabling evaluation of the data.

Most available software tools such as RELION (Scheres, 2012b), cryoSPARC (Punjani *et al*., 2017), SPHIRE (Moriya *et al*., 2017), or cisTEM (Grant *et al*., 2018) use maximum likelihood calculations for classification. The method starts with a random distribution of particles to generate class references. Then it calculates iteratively for every particle the probability of correct rotation, translation and overall match to the reference. In the next step, particles are transformed (rotation and translation is applied) and new averages are created by combining 2D Fourier transforms of the particle images corrected by their respective CTF. After a few iterations, the references provide an overview about the various particles picked from the micrographs (Sigworth, 2016). By this, 2D classification can be used to remove false positive particle picks.

3D Reconstruction and Classification

To obtain a 3D volume from 2D images, back projection is used: as described by the linear image formation model (see Image Formation), the particles observed on the micrographs represent projections of the sample on the grid (Scheres, 2012a). The model sets those projections in relation to the 3D object and can be used to reconstruct a 3D map. In brief, the Fourier transform of a 2D projection corresponds to a slice through the origin of the Fourier transformed 3D volume. By using a similar approach as for 2D classification, the slices can be assigned to positions in the 3D volume, which are then iteratively improved (Sigworth, 2016). To prevent overfitting, reconstruction is performed on two halves of the dataset and the two obtained 'half' maps are compared (see Validation below)(Scheres and Chen, 2012).

Both compositional (e.g., presence/absence of a factor) and conformational heterogeneity in the particles contributing to the 3D maps will lead to worse resolution in the affected areas of the obtained maps since they constitute an average over all particles. For discrete heterogeneity, this can be improved by 3D classification, a process similar to reconstruction, however, with multiple references. Since the available computational power has drastically increased over the last years, classification is especially useful for heterogeneous samples. Looking at biological processes, usually not only one state, but many different states are necessary for fulfilling a biological function, and even very pure cryo-EM samples often contain complexes in various states. In principle it is possible to "purify" such samples computationally. Different states of interest can be sorted from "impurities" (=contaminations or states that are already characterized). To sort for differences in specific areas of a complex, focused refinement or classification can be used. This is done by masking out signals that are outside of the area of interest.

Newer approaches like 'Multi-body-Refinement' can also deal with different parts of a molecule/complex moving (independently), assigning them as separate rigid bodies and refining them individually (Nakane and Scheres, 2021).

Recently, a variety of other tools to resolve such flexibility and provide high-resolution maps of the different variability components, such as 3D variability analysis (Punjani and Fleet, 2021), cryoDRGN (Zhong *et al*., 2021) and Multivariate statistical analysis (MSA) (Heel *et al*., 2016) have been introduced.

A final map can be sharpened according to the B-factor to increase the amplitudes of signal at higher spatial frequencies dampened by the envelope function (Rosenthal and Henderson, 2003). This final map can then be used to generate molecular models of the complex of interest, either by fitting predicted (Jamali *et al*., 2022; Jumper *et al*., 2021; Varadi *et al*., 2022) or known (crystal-) structures into the obtained density, or, if the resolution permits by de novo modelling based on the nucleotide or protein sequence.

Validation

Assigning standard quality hallmarks in cryo-EM is a controversial and much discussed topic. To ensure that the map at the end of processing truly resembles the data is extremely important and thus, various ways of validation have been developed. One important hallmark for estimating with which level of confidence a model can be fit (or build) into a map is the resolution. During the reconstruction of the 3D map, half maps, independently reconstructed from two separate half-sets of the data, are compared to prevent overfitting. From this, Fourier shell correlation (FSC) curves can be calculated, which contain information about SNR levels at different spatial frequencies (Frank and Al-Ali, 1975; Grigorieff, 2000; Harauz and van Heel, 1986; Penczek, 2010b). To compare the overall resolution of different maps, usually a distinct FSC cutoff value is chosen. Proposed values for comparison are an 'gold standard' FSC (GSFSC) of 0.143 (Rosenthal and Henderson, 2003) or a more conservative value of 0.5 (Liao and Frank, 2010). The shape of the curve itself can provide insights on a variety of parameters such as overfitting of noise or remaining heterogeneity (Penczek, 2010b). However, the resolution estimated from the FSC curves represents the global situation of the complex and might not always describe the data completely. To get a better overview, local resolution analysis can be used to estimate resolution for different regions of a map (Cardone *et al*., 2013; Kucukelbir *et al., 2014)*. To estimate how well a model fits to the EM map, a map to model FSC can be calculated. Here, a simulated map of the build/fitted model is compared to the obtained cryo-EM map (Brown *et al.*, 2015a; Rosenthal and Rubinstein, 2015).

The model quality itself can be estimated using scores such as the ones provided by Molprobity (Chen *et al.,* 2010; Davis *et al.*, 2007), which evaluate the atom contacts and geometry using chemical information independent of the underlying cryo-EM map. A newly introduced score, describing how well an atom is resolvable in the cryo-EM map is the Q-score (Pintilie *et al*., 2020).

Ribosomes as targets for structural analysis

Our comprehension of the translational process is closely tied to the progress in structure determination. Due to its relevance, size and ease of purification, the ribosome served as a popular target for crystallography (Ban *et al*., 1998; Ban *et al*., 2000; Cate *et al*., 1999; Clemons *et al.*, 1999; Schluenzen *et al*., 2000; Tocilj *et al*., 1999; Wimberly *et al.*, 2000), as well as cryo-EM (Agrawal *et al.*, 1996; Frank *et al.*, 1995; Spahn *et al.*, 2001). While prokaryotic ribosomes were routinely used for structure determination, crystallization of eukaryotic ribosomes remained challenging for a significant time. The first crystal structure of a eukaryotic yeast ribosome was only solved in 2010 (Ben-Shem *et al*., 2010), quite late compared to the bacterial counterpart (Ban *et al*., 1998). Cryo-EM did not suffer from such limitations on the sample side, but the initial cryo-EM structures only allowed visualization at low-resolution (~15 Å), enabling mainly the docking of previously determined crystal structures into the obtained 3D maps. However, with technical progress, cryo-EM got closer to, and, for distinct cases, even surpassed (Watson *et al.,* 2020*)* X-ray crystallography in resolution, leading not only to the determination of detailed ribosomal structures but also the visualization of various functional ribosome states during the translational process.

Overview of the translational process and involved components

Translation starts from an encoded nucleotide template. The genetic code consists of a sequence of four different bases: adenine, thymine, guanine and cytosine. These bases are conjugated to a pentose sugar and connected by phosphate molecules, forming long DNA strands. To protect the code, the original 'data' stays tucked away safely in the nucleus. Only short-lived RNA transcripts are processed during translation. The production of transcripts also enables the cell to quickly react to changes in its environment (e.g. starvation, stress) by decreasing or increasing the number of transcripts available at a time. In eukaryotes, these messenger RNAs (mRNAs) are transcribed from DNA templates in the nucleus by RNA polymerase II (using uracil instead of thymine), and processed by capping of the 5'end (7-methyl(guanine)-cap), splicing, 3'end cleavage and polyadenylation. The mature mRNA gets exported from the nucleus via the nuclear pore complex to the cytosol, where it is decoded by ribosomes.

Eukaryotic ribosomes are large (> 3.3 MDa) macromolecular complexes, built from RNA and an assembly of proteins (Figure 1). Decoding or translation happens by coordinated action of the small (SSU) and large ribosomal subunit (LSU). The size of ribosomes is commonly described by their sedimentation coefficient in Sverdberg units (S), which corresponds to the size, shape and density of a molecule. In the cytosolic yeast ribosome (80S), the small 40S ribosomal subunit consists of 18S rRNA (1800 base pairs, SGD: RDN37-1) and 33 ribosomal proteins, whereas, the large 60S subunit contains 25S (3396 base pairs, SGD: RDN37-1), 5.8S (158 base pairs, SGD: RDN37-1) and 5S rRNA (119 base pairs, SGD: RDN5-2) as well as additional 46 ribosomal

proteins (Melnikov *et al.*, 2012). The SSU has a distinct shape, where a 'head' structure with a protruding 'beak' and a 'body' structure containing platform, right and left foot are distinguished (Wimberly *et al.*, 2000). Between head and beak, the small ribosomal subunit contains a channel for accommodation of mRNA. The mRNA decoding center is located in this channel on top of rRNA helix 44 (h44) (Yusupova *et al.*, 2001). Hallmarks of the LSU are the central protuberance (CP) on top of the peptidyl-transfer-center (PTC), the L1-stalk, the P0-stalk, which is part of the GTPase-associated center (GAC) and the peptide exit tunnel. The PTC, where amino-acids are joined to form a peptide chain, is the catalytic core of the ribosome and consists solely of RNA. Therefore, the ribosome is an example for a ribozyme (Cech, 2000). The generated peptide chain leaves the ribosome through the largely hydrophilic peptide exit tunnel, starting at the PTC. This exit tunnel is approximately 100 Å long, 10-20 Å in diameter and contains a constriction site between PTC and protein exit (Nissen *et al.*, 2000; Voss *et al.*, 2006).

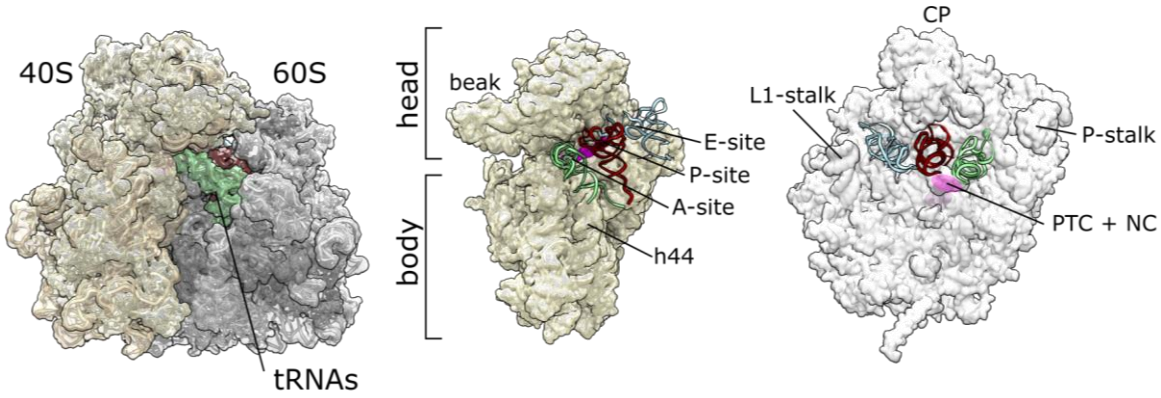

Figure 1: Overview of the eukaryotic 80S ribosome.
(Left) Front view of the ribosome (molecular model from pdbs 6q8y (Tesina et al., 2019) and 7b7d (Ranjan et al., 2021), converted to low-pass filtered densities), 40S is colored in light yellow, 60S in grey, tRNAs are colored in green (A-site tRNA), maroon (P-site tRNA) and light blue (E-Site tRNA). (Middle) View of the intersubunit interface of the 40S. The mRNA is colored in magenta. (Right) Intersubunit interface of the 60S.

Protein synthesis on the ribosome takes place one amino acid at a time, starting with the N-terminus of a protein and finishing with its C-terminus (Dintzis, 1961). The protein encoding region of a mRNA (open reading frame, ORF) is decoded in 5' to 3' direction by small transfer RNA molecules (tRNAs) charged with a specific amino acid dependent on their anticodon sequence (Berg and Offengand, 1958). During the translation process, a tRNA moves through three distinct sites on the ribosome, which span the two subunits: the aminoacyl site (A-site) which binds incoming charged tRNAs, the peptidyl site (P-site), which binds tRNAs after peptide-bond formation and transfer of the nascent chain, and the exit-site (E-site) which binds de-acetylated tRNAs before they dissociate from the ribosome (Agrawal *et al.*, 1996; Rheinberger *et al.*, 1981).

In the A-site of the SSU, each tRNA forms a distinct codon-anti-codon structure (A-helix) with a stretch of three mRNA nucleotides which are accessible in the decoding center on the small ribosomal subunit (described in detail below) (Berg and Offengand, 1958; Carter *et al.*, 2000; Crick *et al.*, 1961; Ogle *et al.*, 2001). Due to the three-letter nature, 64 different nucleotide combinations are possible. Three codons serve as a signal for translation termination, leaving 61 codons encoding 20 different amino acids (Nirenberg, 2004). This degeneration of the genetic code leads to different codon combinations encoding the same amino acid (Lagerkvist, 1978). However, there are differences (especially between species) in the availability of tRNAs and speed of decoding. Some codons are decoded/translated with a higher efficiency (are more optimal) than others. Thus, using synonymous codons with different optimality can serve as a layer of control over translation speed. Decoding proceeds via base pairing of codon and anti-codon, but the number of distinct tRNAs in a cell (~45) is lower than the 61 codons possible on the mRNA. As a consequence, some codons have to be recognized by more than one tRNA (Agris, 1991; Crick, 1966). This occurs by wobble base pairing between the third base in a codon and the corresponding anti-codon. To that end, adenosine can be chemically modified to inosine (Gerber and Keller, 1999), which can pair with cytidine, uridine and adenosine in the wobble-position. Overall, wobble decoding leads to slower translation of such codons (Lareau *et al.*, 2014; Sorensen and Pedersen, 1991; Stadler and Fire, 2011).

The eukaryotic translation cycle

The translational process can be divided into four distinct steps: Initiation, elongation, termination and recycling. Since ribosome synthesis is an (energy-) expensive process for the cell they are usually used for multiple rounds of translation requiring a recycling step before the next round of translation can be initiated. Due to its importance for the cell, the translational cycle is well conserved (especially regarding elongation), but also tightly regulated. Another requirement for this process is a certain flexibility: The cell needs to be able to adjust translation of specific proteins in response to environmental factors such as stress or starvation. Overall, translation takes place in the cytoplasm or across the endoplasmatic reticulum (ER) membrane and in mitochondria.

Initiation

To start translation of a protein, both ribosomal subunits, together with an initiator tRNA need to assemble on an mRNA. This involves recognition of the 5’ mRNA cap and 3’ poly(A)-tail to ensure that only intact, mature mRNAs are translated. In eukaryotes, the rate-limiting initiation process involves at least twelve initiation factors (IFs), that coordinate the correct assembly of a ribosome at the start of an ORF (Aitken and Lorsch, 2012; Aylett and Ban, 2017).

Initially, a ternary complex (TC) consisting of initiation factor eIF2, GTP and an initiator Met-tRNA (eIF2•GTP•$tRNA_i^{Met}$) is formed, which subsequently binds the small ribosomal subunit. The assembly of this 43S pre-initiation complex (PIC, consisting of TC and 40S) is promoted by initiation factors eIF1, eIF1A, eIF3 and eIF5. Meanwhile, the mRNA cap is bound by the eIF4F complex (eIF4A, eIF4B, eIF4G, eIF4E) which leads to circularization of the mRNA via interaction with the poly(A)-binding protein Pab1 (Archer *et al*., 2015; Merrick, 2015). eIF4G interacts with the previously formed 43S, resulting in the formation of the 48S initiation complex.

The small ribosomal subunit and mRNA are now joined and the mRNA can be scanned 5'-to-3' for the start codon. Identification of the start codon (AUG) happens via its surrounding Kozak-sequence (Kozak, 1986). The initiator tRNA can form a base-pair with the AUG codon in the P-site forming the closed 48S conformation (Llacer *et al*., 2015). AUG recognition leads to hydrolysis of GTP on eIF2, promoted by eIF5 and eIF5B (Algire *et al*., 2005). In the final step, the 60S subunit joins and all initiation factors are released, denoting the start of the elongation cycle. As soon as the ribosome has moved far enough from the initiation site, the next ribosome can initiate translation on the same mRNA, leading to the occupancy of a single mRNA by multiple translating ribosomes at any given time, dependent on the speed of initiation.

Elongation

After formation of the 80S initiation complex, the ribosome moves along the mRNA in 5' to 3' direction, sequentially adding amino acids to the protein chain. There are three basic steps in this elongation process: decoding, peptide bond formation and translocation (reviewed in (Dever *et al*., 2018)). Initially, the Met-$tRNA_i$ is situated on the start codon in the P-site, and the unoccupied A-site exhibits the second codon of the ORF.

Charged aminoacyl-tRNAs are delivered by eukaryotic elongation factor 1A (eEF1A), in complex with GTP (ternary eEF1A•GTP•tRNA complex). This complex binds to the ribosome at the GTPase-associated center (GAC) at the P-stalk, a common binding site for GTPases such as eEF1A, EF-G, eEF2 and eRF3, then probes the A-site. If it's a cognate tRNA, the anti-codon fits the displayed codon, which leads to base-pairing of the first two bases with Watson-Crick geometry (Crick, 1966) forming a short A-helix. In addition to correct base pairing, decoding involves a geometric check of this helix by 18S rRNA helix 44. Here, conserved residues A1755, A1756 and G577 (in yeast, mammalian: A1824, A1825 and G626, bacteria: A1492, A1493 and G530) are interacting with the minor groove formed by the codon-anticodon A-helix (Loveland *et al*., 2017; Ogle *et al.*, 2001; Shao *et al*., 2016). A recent study in bacteria found these residues also interacting with near cognate tRNAs (Demeshkina *et al.*, 2012) and G530 was proposed to be responsible for locking the A-helix in the decoding center in case of a 'true' cognate tRNA (Loveland *et al.*, 2017). Activation of eEF1A (by GTP hydrolysis) and release of eEF1A•GDP leads to full accommodation of the tRNA into the A-site (PRE-state), with the acceptor stem reaching into the PTC. Decoding is followed by peptide bond formation and peptide transfer.

In the peptidyl transferase center on the 60S subunit, the amino group of the amino acid on the newly accommodated tRNA performs a nucleophilic attack on the ester bond of the peptidyl-tRNA in the ribosomal P-site, leading to transfer of the peptide chain onto the tRNA in the A-site. During this step, eIF5A can bind to the ribosomal E-site, improving positioning (of the CCA end of P-site tRNA) which further promotes peptide bond formation (especially in difficult cases) (Han *et al*., 2020; Saini *et al*., 2009; Schmidt *et al*., 2016a). Initially eIF5A was identified as an initiation factor (Benne and Hershey, 1978; Glick and Ganoza, 1975; Kemper *et al*., 1976) but was later observed to play a role during ribosome rescue (Gutierrez *et al*., 2013) and translation elongation (Gregio *et al*., 2009).

After peptide bond formation, a rotation of the ribosomal subunits relative to each other occurs. Here, ribosomes adopt a "rotated" or "hybrid" PRE-state which is in equilibrium with the non-rotated PRE-state (Frank and Agrawal, 2000). Due to the rotation, the tRNAs now occupy P- and E-sites on the large ribosomal subunit, while still in A- and P-site on the small subunit (A/P-, P/E-tRNAs) (Behrmann *et al*., 2015; Budkevich *et al*., 2011; Moazed and Noller, 1989). Elongation factor eEF2, another translational GTPase, preferentially binds to the rotated ribosome and induces a "head swivel" movement of the SSU, leading to intermediate chimeric ap/P- and pe/E-tRNA states (Flis *et al*., 2018), followed by back rotation of the SSU relative to the LSU. This translocates the tRNAs and mRNA, in a way that they now occupy P/P and E/E-site on SSU and LSU, respectively (POST-state). eEF2 is structurally close to the eEF1A•GTP•tRNA complex and also binds to the ribosomal A-site, disrupting the interaction of the rRNA and the mRNA-tRNA helix, which is thought to enable the observed head swivel movement. After translocation, the de-acetylated tRNA is released from the E-site. The A-site is now free for accommodation of the next charged tRNA.

Termination and Recycling

The elongation cycle repeats until a stop-codon (UAA, UAG or UGA) is encountered. At this point, the protein, which has been successfully produced, needs to be released and the ribosomal subunits dissociated, to be available for subsequent rounds of translation. To terminate the translation reaction, one of the three stop codons is recognized by release factor eRF1 instead of being decoded by a cognate tRNA. In contrast to the codons in the rest of the ORF, four bases are read during termination, with a +4 or +5 purine (+1 being the first base of the stop codon) increasing the efficiency (McCaughan *et al*., 1995; Pedersen and Curran, 1991). Depending on the identity of this nucleotide, there is also more or less read-through of the stop codon, by accommodation of near-cognate tRNAs (Beznoskova *et al*., 2016; Xue *et al*., 2017). For successful termination, the U-turn geometry, adopted by the stop codon, is read out by eRF1 (Brown *et al*., 2015b; Matheisl *et al*., 2015) via its conserved NIKS and GTS motifs (Conard *et al*., 2012; Kolosov *et al*., 2005). eRF1 structurally resembles the shape of tRNAs and binds the ribosome together with eRF3 and GTP (Matheisl *et al.*, 2015; Preis *et al*., 2014; Shao *et al.*, 2016).

A GGQ motif on the tip of eRF1, in a similar position to the amino-acid on a tRNA, leads to release of the nascent chain when accommodated in the PTC (Frolova *et al*., 1999; Seit-Nebi *et al*., 2001). The mechanism is similar to the one in elongation: the nucleophilic attack of a water molecule, coordinated by the GGQ, leads to hydrolysis and subsequent release of the peptide chain. Accommodation of eRF1 is closely coupled to release by eRF3. Similar to elongation factor eEF1A, which releases tRNAs upon GTP hydrolysis, eRF3 releases eRF1 after GTP hydrolysis (Alkalaeva *et al*., 2006).

After translation termination, the ribosome is recycled. Upon release of the nascent chain, the ribosome still contains eRF1, a deacetylated tRNA and mRNA. Disassembly of this state is crucial to free up the ribosomal subunits for subsequent rounds of translation. The dissociation of ribosomal subunits is facilitated by ABCE1 (Rli1 in yeast), an evolutionary conserved member of the ATP-binding cassette family of proteins and is dependent on its ATPase activity (Becker *et al*., 2012; Pisarev *et al*., 2010; Shoemaker and Green, 2011). Upon dissociation of eRF3 from the ribosome, ABCE1 binds to the post-termination 80S, where it contacts eRF1 (Becker *et al.*, 2012; Brown *et al.*, 2015b; Shao *et al.*, 2016). It has two iron-sulfur-clusters (4Fe-4S) and two nucleotide binding domains. Upon ATP binding, conformational changes are believed to force eRF1 into the inter-subunit space, leading to destabilization of the ribosomal inter-subunit bridges and ultimately dissociation. After dissociation of the ribosome, ABCE1 can stay bound to the 40S, preventing re-association of 40S and 60S subunits (Heuer *et al*., 2017; Nurenberg-Goloub *et al*., 2020) and likely play a role during initiation (Kratzat *et al*., 2021). During 40S recycling, mRNA and tRNA are thought to be removed from the 40S by MCT-1(Tma20)/DENR(Tma22) and eIF2D (Tma64) and the translation cycle can start again (Young *et al*., 2018; Young *et al*., 2021).

Errors in translation

Translation is a central process, which needs to be tightly regulated to keep a cell in a productive ‘equilibrium’ state (homeostasis). Disruption of homeostasis has detrimental effects such as proteotoxicity or neurodegeneration (Choe *et al*., 2016; Chu *et al*., 2009; Nedialkova and Leidel, 2015). Of course, components involved in translation undergo quality checks during their lifecycle. Processes such as transcription, mRNA transport, ribosome assembly, or translation, all have checkpoints and proofreading mechanisms to ensure components meet certain quality criteria. Still, mistakes can happen and need to be addressed.

Stalling and pausing

The state of translation can be supervised by monitoring the progress of the ribosome. This principle is not only true for translation but also for other cellular processes such as replication or transcription. One example for this is DNA repair, which can be triggered by disruption of movement of DNA/RNA polymerases (Edenberg *et al*., 2014).

Ribosomes can halt translation due to various reasons. Pauses/Stalls can be mRNA-mediated (e.g. stem loop structures, non-optimal codons, damage by UV radiation) or nascent peptide-mediated (poly-proline; arrest peptides), they can arise from insufficient levels of available tRNAs, or damage/mutations in the ribosome itself. Overall, there is a multitude of different reasons why translation cannot progress (Brandman and Hegde, 2016; Shoemaker and Green, 2012).

Of course, not all instances of slowed or paused translation are due to an underlying detrimental situation. Pausing can also be necessary to allow co-translational folding of proteins, to allow proteins to interact with partners, or to be targeted to the correct cellular compartment (Collart and Weiss, 2020). Across all species, some stalling sequences fulfill important regulatory functions such as the response to metabolites (e.g. SAM, spermidine, sucrose, arginine). One example for this is the fungal arginine attenuator peptide (AAP), a cis-regulatory element, which stalls the ribosome in the presence of high levels of arginine, leading to decreased translation of the downstream encoded carbamoyl-phosphate-synthetase, which is needed to synthetize more arginine (Wang *et al*., 1998). Another example is pausing of translation during targeting to the ER: when the signal sequence of a secretory protein is recognized by SRP, translation is slowed, the RNC is targeted to the ER membrane and the protein is co-translationally translocated into the ER (Mandon *et al*., 2013). In a slightly different mechanism, pausing and the subsequent targeting to the ER membrane is used by XPB1u to enable splicing of the mRNA by IRE1α into *XBP1s* mRNA, a critical step of the unfolded protein response (Plumb *et al*., 2015; Shanmuganathan *et al*., 2019).

Frameshifting

Ribosomal slowdown is used ubiquitously as regulatory mechanism, e.g. to enable folding or recruitment of necessary factors. In some cases, pauses can be resolved by factors like eIF5A, the homolog of bacterial EF-P (Schmidt *et al.*, 2016a; Schuller *et al*., 2017), which can promote peptide-bond formation for stretches of unfavorable amino-acids like proline (Gutierrez *et al.*, 2013). Alternatively, frameshifting can occur, where the ribosome 'slips' on the mRNA and thus enters an alternative three-letter reading frame of the codons. Although frameshifting can be employed as a regulatory mechanism, where a deliberate slowdown of the translational machinery leads to a shift (+1 or -1) in reading frame which changes the produced protein (Farabaugh, 1996), inadvertent frameshifting has often adverse effects. Recently, Mbf1 has been identified to prevent frameshifting at inhibitory codons in yeast (Wang *et al*., 2018). Originally, the small (16 kDa) protein Mbf1 was identified as a transcriptional co-activator, bridging nuclear receptor FTZ-F1 and the TATA-box binding protein (TBP) in *Drosophila* (Li *et al*., 1994; Takemaru *et al*., 1997). It is conserved in eukaryotes and archaea. In the latter, ribosome association to 30S subunits and 70S ribosomes has been shown (Blombach *et al*., 2014).

In yeast, Mbf1 connects the DNA-binding region of Gcn4 protein and TBP, acting as a coactivator of Gcn4 (Takemaru *et al*., 1998) but was also early on identified as a suppressor of frameshifting (Culbertson *et al*., 1982). Mbf1 contains a N-terminal Mbf1-domain and a C-terminal helix-turn-helix domain (HTH). The effect of frameshifting inhibition by Mbf1 is dependent on ribosomal protein uS3 (Wang *et al.*, 2018). Together with ribosomal protein uS5, uS3 forms part of the mRNA entry channel of the 40S and interacts with the mRNA via residues R116 and R117 (Simms *et al*., 2018). Interestingly, mutation of a different residue of uS3, K108, which resides in a region that forms two α-helices on top of the mRNA entry also increased frameshifting. This effect did not increase with an additional Mbf1 deletion which was previously found to increase frameshifting. Based on these findings, it was proposed that Mbf1 and uS3 maintain the reading frame in a related way (Wang *et al.*, 2018). However, in this case reading frame maintenance comes at the cost of stabilizing the ribosomes stalled at inhibitory codons, which in turn requires a rescue system to be resolved.

Ribosome rescue

For unproductive stalls, translation is abandoned. The produced nascent chain and the mRNA need to be degraded and if the ribosomes are intact, they should be rescued. Since pauses and frameshifting can be both problematic or regulatory, intensive effort needs to be invested to ensure that problems are reliably recognized but regulatory pauses can still occur. To achieve the necessary level of control, various, partially redundant pathways have evolved (reviewed e.g. by Shoemaker and Green, 2012). Some of these pathways were defined with a focus on the decisive mRNA defect and resulting decay. Nonsense-mediated decay (NMD) deals with mRNAs exhibiting an abortive stop codon in the ORF. Nonstop decay (NSD) is defined as targeting mRNAs without a stop codon, resulting in translation of the 3' UTR and eventually poly(A)-tail. No-go decay (NGD) recognizes mRNAs with translation elongation stalls and leads to endonucleolytic cleavage of the mRNA. Thus, both NGD and NSD take care of mRNAs that prevent the ribosome from finishing the translation elongation step and are closely related, involving mostly the same factors. NGD/NSD is coupled to ribosome associated quality control (RQC) which rescues the stuck ribosome and leads to degradation of the nascent chain.

As described above, in canonical termination, translation terminates at a stop codon, a process facilitated by release factors. However, stalled ribosomes may be located at arbitrary locations in the ORF and cannot be rescued in the same way. One of the first complexes identified as playing a role in the rescue of such ribosomes was Dom34•Hbs1 (Pelota•Hbs1 in mammals). The complex was found to recognize stalls in translation and lead to an upstream endonucleolytic cleavage event necessary to degrade stem-loop containing mRNA (Doma and Parker, 2006). Later studies, however, observed a preference for an empty A-Site or at least for shorter mRNA constructs, where increasing lengths of mRNA diminished the splitting activity of Dom34•Hbs1 (Hilal *et al*., 2016; Pisareva *et al*., 2011; Shoemaker and Green, 2011; Tsuboi *et al*., 2012).

Additionally, Dom34•Hbs1 was found to rescue non-translating ribosomes located on the poly(A) sequence in the 3' UTR (Guydosh and Green, 2014) or empty 'hibernating' ribosomes which accumulate as translation shuts down due to cellular stress (Pisareva *et al.*, 2011; Tzamarias *et al*., 1989; van den Elzen *et al*., 2014; Wells *et al*., 2020).

Structurally, Dom34/Pelota is a homolog of eRF1, but lacks both the NIKS motif for codon recognition and the GGQ motif necessary for peptide release. Where the release factor eRF1 recognizes its target by interaction with the stop codon, no such interaction is possible for Dom34. Instead, part of domain N of Dom34 is inserted into the mRNA decoding center on the 40S ribosomal subunit (Becker *et al*., 2011; Hilal *et al.*, 2016; Shao *et al.*, 2016), a conformation that would clash with present mRNA and explains the preference for an empty A-site. Dom34 is recruited to the ribosome by the GTPase Hbs1 (homologous to eRF3, eEF1A and Ski7) in a complex similar to eRF1•eRF3. As in canonical termination, the ribosomal subunits are then dissociated in a mechanism facilitated by ABCE1.

Ribosome associated quality control (RQC)

In contrast to canonical termination, after Dom34•Hbs1 (or RQT, described below) induced dissociation, the ribosomal 60S subunit remains associated with both tRNA and the nascent chain due to the missing peptide release (Brandman *et al*., 2012; Pisareva *et al.*, 2011; Shoemaker *et al*., 2010). Before the large ribosomal subunit can be used in subsequent rounds of translation, this tRNA, as well as the tethered nascent chain (NC), need to be removed. The translated protein is unfinished and thus unlikely to have passed important steps of co-translational protein maturation such as folding. Proteins from such aberrant translation processes are potentially problematic and often form aggregates, threatening cellular homeostasis. As a consequence, the translated nascent chain is targeted for degradation by the proteasome.

To achieve this, the 60S•tRNA•NC complex is recognized by the ribosome associated quality control (RQC) machinery (Figure 2). In an initial step, Rqc2 (also Tae2; human: NEMF) senses the exposed tRNA and binds to the 60S, preventing rejoining of the small ribosomal subunit. Subsequently, it recruits and stabilizes binding of E3 Ligase Ltn1 (human Listerin) (Defenouillere *et al*., 2013). Ltn1 wraps around the 60S, contacting the GTPase interaction site with its N-terminus and positioning the C-terminal RING domain next to the end of the peptide exit tunnel. This enables Ltn1 to add K48-linked ubiquitin to the nascent chain, a signal targeting the emerging protein for proteasomal degradation. If ubiquitination is slow, Rqc2 additionally catalyzes the addition of C-terminal alanine and threonine (CAT) tails to the nascent chain, revealing more amino acids yet remaining in the peptide exit tunnel. This mRNA template free elongation of the nascent chain happens by Rqc2 positioning a second tRNA in the A-site close to the peptidyl tRNA (Shen *et al*., 2015). CAT-tailing is thought to ensure the availability of a lysine residue for Ltn1 mediated ubiquitination, increasing the chance that the protein is targeted for degradation.

If no lysine is available, it may serve as an aggregation seed for the nascent chains possibly serving as a signal for cellular stress by Hsf1 activation (Brandman *et al.*, 2012; Joazeiro, 2019).

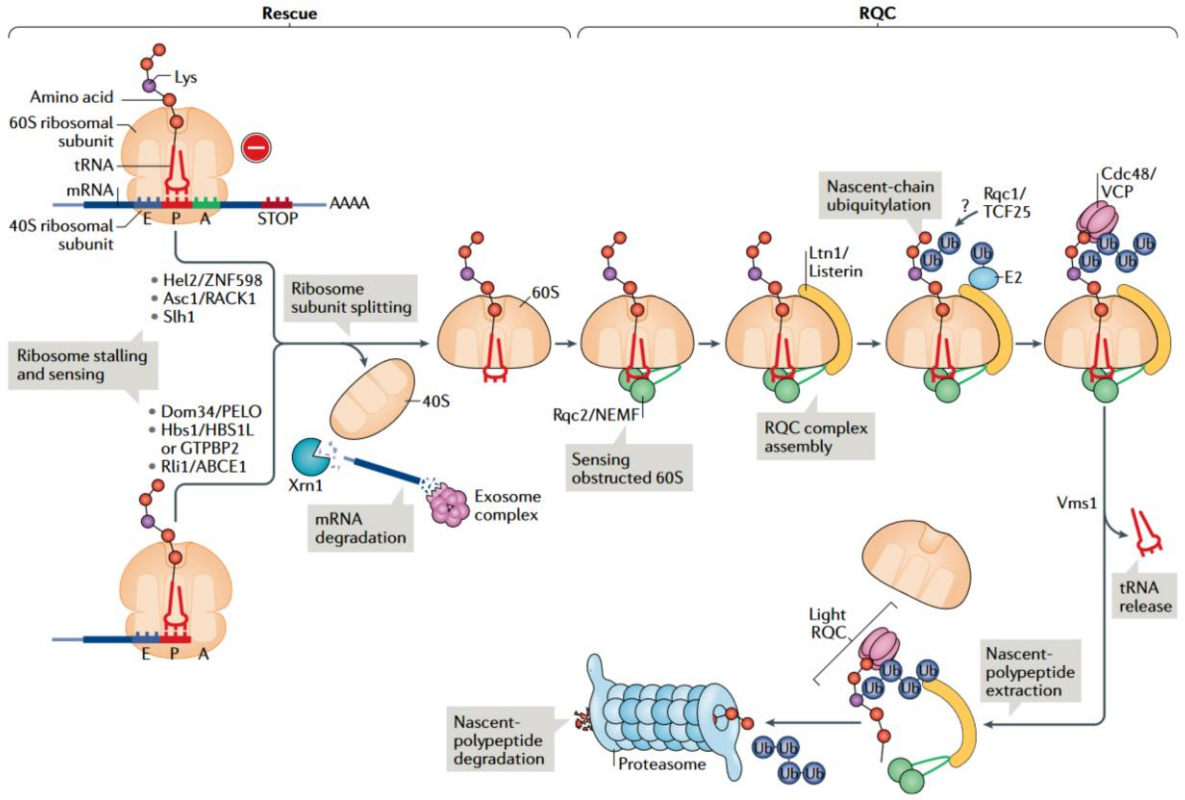

Figure 2: Overview of the RQC process triggered either by Dom34•Hbs1 or RQT.

After ribosome dissociation the 60S subunit remains associated with peptidyl-tRNA and nascent chain. This serves as a substrate for the RQC machinery. After recognition by Rqc2/NEMF, Ltn1 binds the 60S and ubiquitinates the nascent chain, thereby targeting it for degradation. Rqc1, together with the ubiquitin chain are necessary for Cdc48 recruitment and extraction of the NC. Vms1 cleaves the CCA acceptor end of the tRNA to enable NC release. The NC is degraded by the proteasome and the 60S subunit can be recycled for subsequent rounds of translation.(Figure adapted from Joazeiro, 2019)

Another factor, Rqc1, together with the ubiquitin signal added by Ltn1 recruits AAA-ATPase Cdc48, which extracts the nascent chain and facilitates delivery to the proteasome. However, for successful degradation, release of the nascent chain from the tRNA is necessary. This is achieved by a paralog of eRF1 called Vms1 (human ANZF1)(Su *et al.*, 2019; Verma *et al.*, 2018). In contrast to eRF1, Vms1 does not hydrolyze the bond between nascent chain and tRNA but rather catalyzes the cleavage of the peptidyl tRNA via its catalytic GSQ motif, which engages the universal 3'CCA end of the tRNA. Interestingly, addition of this CCA acceptor end by the enzyme TRNT1, is one of the last steps in tRNA maturation before they can be charged with an amino acid. During maturation, this serves as a quality control step, sorting out faulty tRNAs before they can lead to problematic translation. By cleaving the CCA end, Vms1 forces the tRNA to undergo this quality control step a second time. This effectively ensures that if the ribosome was stalled due to a faulty tRNA, this particular tRNA will be degraded and not used in further rounds of translation (Yip *et al.*, 2019).

mRNA degradation

Regular mRNA degradation requires deadenylation by Pan2•Pan3 or Ccr4•Not (Brown and Sachs, 1998; Tucker *et al*., 2001) and decapping by Dcp1p and Dcp2p (Steiger *et al*., 2003; van Dijk *et al*., 2002) before an mRNA can be actively degraded (mainly by Xrn1). However, in case ribosomal rescue is triggered by Dom34•Hbs1, the mRNA template is presumed faulty, leading to an endonucleolytic cleavage event which provides mRNA intermediates with free 5‘- and 3‘ends (Doma and Parker, 2006). A free 5‘end without a cap structure is targeted by exonuclease Xrn1. This exonuclease degrades mRNA in 5’-to-3’ direction (Hsu and Stevens, 1993; Kenna *et al*., 1993). 3’ends are accessed by the Ski-complex and the exosome and lead to 3’-to-5’ degradation of the mRNA (Anderson and Parker, 1998). Both Xrn1 and the Ski-complex have been shown to associate with ribosomes. As the major exonuclease for regular mRNA degradation, Xrn1 can degrade mRNA co-translationally while bound to the mRNA exit on the small ribosomal subunit, following the natural direction of the translational process (Tesina *et al.*, 2019). The Ski-complex operates in the reverse direction. It consists of the ATP dependent helicase Ski2, Ski3 and two copies of Ski8. It was proposed that in yeast, the ribosome bound Ski-complex serves as an adaptor to Ski7 and the exosome (Schmidt *et al*., 2016b). In the human system SKI is tethered to the ribosome in a more flexible manner, directly interacting with the exosome for mRNA degradation (Kogel *et al*., 2022). The main catalytic function of the Ski-complex originates from the Ski2 subunit and its 3’-to-5’ RNA helicase activity, which is thought to enable mRNA threading into the exosome. Recently, an additional role was proposed for the Ski-complex. In an *in vitro* assay, it was observed to extract mRNA from stalled 80S, independent of Ski7 and the exosome. This could clear the A-site and thus render the ribosomes susceptible to degradation via Hbs1•Dom34 (Zinoviev *et al*., 2020).

Collisions

For ribosomes with an empty A-site or that translated into the poly(A)-tail, it is rather easy to decide that this situation is not regulatory and needs to be dealt with. But what about stalling in the ORF? Initial studies, focused on different factors interacting with stalled ribosomes could not fully answer this question. However, a study focusing on the role of the ribosome itself during the stalling event provided a possible mechanism. In this study, 5’ mRNA fragments observed after endonucleolytic cleavage of a mRNA reporter with multiple inhibitory codons mapped quite far upstream of the stall site (Simms *et al*., 2017). Additionally, the endonucleolytic cleavage was only observed when the stall site was more than 105 nucleotides downstream from the start codon and decreased availability of ribosomes on a message lead to a decrease in the observed cleavage products.

All these observations hinted at the involvement of multiple ribosomes. In the same study, it was shown, that by cycloheximide treatment of a yeast strain, where half of the ribosome population was resistant against the translation interrupting antibiotic, endonucleolytic cleavage events could be deliberately induced (Simms *et al.*, 2017).

Thus, it was proposed that collision of ribosomes in the ORF, instead of stalling itself, serves as a signal for rescue pathways. Usually, initiation, rather than elongation, is the rate limiting step of translation. This ensures a distinct distribution of multiple ribosomes on a single mRNA. However, if a stalled ribosome pauses and does not resume translation, multiple ribosomes that were already translating the same mRNA will form a queue. The next upstream ribosome will continue translating until the point where the mRNA is blocked by the stalled ribosome forming a 'collision'. Interestingly, by using this mechanism, the level of control over this process is substrate specific since it depends on the initiation rate for a given mRNA. This leads to a specific tolerance duration for regulatory stalling, before collision should trigger degradation (Park and Subramaniam, 2019).

Inducing collisions

To study collided ribosomes in detail, various stall-inducing systems have been developed. Interrupting translation by addition of antibiotics like the above-mentioned cycloheximide has been established to prevent ribosome run-off during purifications for some time. Low-dose treatment of cells using emetine (another translation inhibitor) was found to stall only part of the translating ribosomes and thus generate collisions (Juszkiewicz *et al*., 2018; Simms *et al.*, 2017; Sinha *et al*., 2020; Wu *et al*., 2020). But also, different mRNA constructs harboring poly(A) stretches, problematic sequences or truncations have been employed to study both stalls and collisions (see Ribosome Rescue). In yeast, a variety of *in vivo* inhibitory codon-pairs have been identified: Initially, stretches of CGA codons, encoding arginine, were found to inhibit gene expression (Letzring *et al*., 2010; Letzring *et al*., 2013). Further studies showed that there are actually 17 di-codon-pairs that lead to reduced gene expression, all dependent of wobble-decoding (Gamble *et al*., 2016).

But how does translation of a poly(A)-tail or of a specific codon lead to stalling? Structural analysis of ribosomes stalled on di-codon combinations CGA-CGA (Arg-Arg) and CGA-CCG (Arg-Pro) revealed distinct mRNA arrangements in the ribosomal A-site (Tesina *et al*., 2020). For both codon combinations, the base in +4 position is flipped away from the A-site and interacts with 18S rRNA instead, impeding decoding by an arriving tRNA. In case of CGA-CCG, the mRNA forms a hairpin structure incompatible with accommodation of A-site tRNA. For poly(A) translation the effect is two-fold: the repeated addition of lysine residues in the PTC affects the efficiency of translation (but only modestly). Similar to the mechanism observed for di-codon stalling, the main contribution to the observed stalling efficiency originates from the mRNA, which forms a decoding incompetent π-stack in the A-site of the ribosome (Chandrasekaran *et al*., 2019; Tesina *et al.*, 2020).

Screening of endogenous genes for the CGA-CGA codon pair in yeast identified *SDD1* as an endogenous substrate for RQC (Matsuo *et al*., 2020). Structural analysis of the *SDD1* stalled ribosome revealed that also here, stalling is facilitated by a combination of the inhibitory CGA-CGA codon pair and the translated Sdd1 arrest peptide, similar to the mechanism observed for poly(A) mediated stalling.

Structure of collided ribosomes

The question remained, how collided ribosomes could serve as a proxy for problematic translation. Here, structural analysis of collided disomes (Figure 3) showed that they form a unique 40S-40S interface, with the collided ribosome positioned in close proximity to the mRNA exit of the stalled one (Ikeuchi *et al*., 2019; Juszkiewicz *et al.*, 2018). The stalled ('lead') ribosome is in a non-rotated POST-state with P/P- and E/E-tRNA, similar to stalled 80S ribosomes (Becker *et al.*, 2011; Becker *et al.*, 2012; Hilal *et al.*, 2016; Tesina *et al.*, 2020). The colliding ribosome was observed in a rotated PRE-state with hybrid tRNAs in A/P- and P/E-position, a state matching incomplete mRNA translocation due to the encountered roadblock.

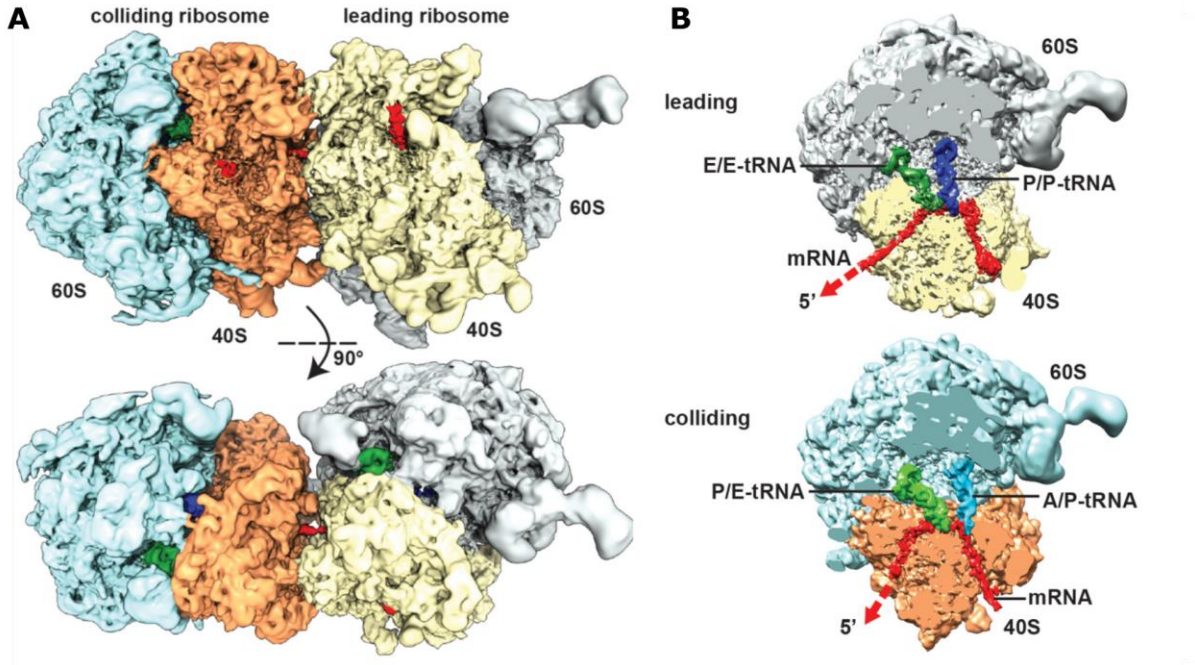

Figure 3: Structure of the collided ribosome.

(A) Overview of the collided disome. The lead ribosome and colliding ribosome form a tight 40S-40S interface (B) tRNA states in the collided ribosomes, the lead ribosome is in a POST state with P- and E-site tRNAs while the collided ribosome is in a rotated PRE state with hybrid A/P and P/E-tRNAs. (Figure adapted from Ikeuchi et al., 2019)

Between stalled and collided ribosome, the mRNA bridges the 40S-40S interface. Based on the surrounding interface, the mRNA between the ribosomes is quite inaccessible, matching experiments showing that collided ribosomes are resistant to treatment with nuclease which enabled detection in 'disome' foot-printing analysis (Guydosh and Green, 2014; Guydosh *et al*., 2017; Wolin and Walter, 1988).

Intriguingly, collision, stalling and frameshifting inhibition were found to involve ribosomal protein Asc1/RACK1 and ubiquitination of ribosomal proteins by E3 ligase Hel2 (discussed below). At the 40S-40S interface, the disomes form a tight RACK1-RACK1 interaction and the ubiquitination targets of Hel2 are in close proximity, arguing that this interface is indeed the target for recognition of problematic translation. Prolonged stalling does not only produce disomes, but also leads to formation of stable trisomes (e.g. from SDD1) which form two similar interfaces (Matsuo *et al.*, 2020).

Collision sensors

Although much information could be gained from studying *in vitro* collided ribosomes, the question remained how exactly collisions are recognized in the cells. Further, disome profiling in yeast showed that collision events are actually quite widespread (up to 20 % of all translating ribosomes, (Diament *et al*., 2018)), raising another question on how collisions are regulated in a way that not everything is degraded.

The first described sensor of collisions is E3 ubiquitin-ligase Hel2 (human ZNF598)(Ikeuchi *et al.*, 2019; Juszkiewicz *et al.*, 2018). It is required to abort translation and was shown to trigger RQC after ubiquitination of ribosomal target proteins (Garzia *et al*., 2017; Ikeuchi *et al.*, 2019; Juszkiewicz *et al.*, 2018; Juszkiewicz and Hegde, 2017; Matsuo *et al*., 2017; Matsuo *et al.*, 2020; Simms *et al.*, 2017). Together with an E1 ubiquitin-activating enzyme and E2 conjugating enzyme it adds ubiquitin to lysine residues of a target protein (Scheffner *et al*., 1995). Hel2 contains a RING domain, three zinc-finger (ZnF) domains and a proline-rich motive. The RING domain and ZnF are necessary for ubiquitination (Ikeuchi *et al*. 2019). The RING domain serves as the binding site for the E2 conjugating enzyme which is bound to ubiquitin, mediating the transfer from E2 to the protein of interest. Hel2 is thought to recognize the unique 40S-40S interface and ubiquitinate various ribosomal proteins (e.g., uS10, eS10, eS7) of the collided ribosomes. In contrast to proteasomal degradation where the ubiquitin on substrates are linked via lysine 48, the activity of Hel2 generates an ubiquitin chain, linked via lysine 63, which serves as a signal for ribosomal rescue (Juszkiewicz *et al.*, 2018). While studying Hel2, two seemingly contradicting observations were made: on the one hand, loss of Hel2 increases ribosome collision (D'Orazio *et al*., 2019; Matsuo *et al.*, 2020), but at the same time, loss of Hel2 was found to promote frameshifting at stall sites (Juszkiewicz and Hegde, 2017; Letzring *et al.*, 2013; Matsuo *et al.*, 2017; Sundaramoorthy *et al*., 2017) and decreases the amount of disomes (Meydan and Guydosh, 2020). Those observations seem to be counterintuitive but can be reconciled. If the stall is not so strict, ubiquitination by Hel2 might be necessary to signal for translation to pause, whereas for more severe stalling events, this is not necessary (Juszkiewicz *et al*., 2020b).

Interestingly, lack of Hel2 was found to lead to phosphorylation of initiation factor eIF2α (part of eIF2) by Gcn2 (Meydan and Guydosh, 2020), activating the integrated stress response (ISR), and thus decreasing global translation by blocking initiation.

If eIF2α is phosphorylated, GDP cannot be exchanged for GTP on eIF2, preventing the formation of a 43S pre-initiation complex. The Gcn2 kinase is part of the GCN complex (Gcn1•Gcn2•Gcn20), found to be co-immunoprecipitated with Hel2 (Simms *et al.*, 2017) which was previously reported to be activated by ribosomal stalling upon starvation (Garcia-Barrio *et al*., 2000; Harding *et al*., 2019; Inglis *et al*., 2019; Ishimura *et al*., 2016). Recently the structure of Gcn1 bound to collided ribosomes could be solved, establishing Gcn1 as a bona fide collision sensor by spanning over both lead and collided ribosome (Pochopien *et al*., 2021). In the observed structure Gcn1 was bound to the disomes together with Rbg2 and Gir2, two factors promoting cell growth under starvation conditions (Ishikawa *et al*., 2013). It was proposed that the Rbg2•Gir2 complex competes with Gcn2 for Gcn1 binding, giving an initial idea how Gcn2 may be activated and regulated upon collision to trigger ISR (Pochopien *et al.*, 2021).

Another collision sensing mechanism was described in the human system. Here, collision dependent stress response activation was found to be dependent on ZAKα (MAP3K). In the proposed mechanism, RQC and NGD deal with low levels of collisions. If this proves insufficient and the quality control pathways are overwhelmed, ZAKα is recruited to collided ribosomes. Depending on the severity, this triggers either the integrated stress response, blocking translation initiation via Gcn2 to reduce the levels of collision, or, in severe stress scenarios (ribotoxic stress response ,RSR), activates p38/JNK leading to apoptosis and cell death (Wu *et al.*, 2020).

Rescue after collision

Depending on which ribosomal protein is modified by Hel2, the mechanism of rescue differs. In both mammalian cells and yeast, ubiquitination of uS10 on collided ribosomes by Hel2/ZNF598 serves as a signal for ribosome dissociation by the RQC-trigger (RQT, ASCC or hRQT in human) complex (Juszkiewicz *et al.*, 2020b; Liaud *et al*., 2019; Matsuo *et al.*, 2017; Narita *et al*., 2022; Sitron *et al*., 2017). Similar to dissociation by Dom34•Hbs1, resolving the stall results in an 60S bound to tRNA and nascent chain which is processed by the RQC machinery.

The RQT complex was identified both in genetic screens analyzing ribosome read-through (Sitron *et al.*, 2017) and as co-purifying with Hel2-bound ribosomes (Matsuo *et al.*, 2017). While it is not necessary for ubiquitination of the ribosomes, it is necessary to trigger dissociation of the stalled ('lead') ribosome after ubiquitination (Matsuo *et al.*, 2020). Studies in the mammalian system observed that upon dissociation of the lead stalled ribosome, the collided one could resume translation (Juszkiewicz *et al.*, 2020b).

RQT is a trimeric complex, consisting of the ATP-dependent RNA helicase Slh1 (human ASCC3), and the two co-factors Cue3 (human ASCC2) and Rqt4 (ASC1/TRIP4) (Juszkiewicz *et al.*, 2020b; Matsuo *et al.*, 2017; Sitron *et al.*, 2017).

In yeast, Slh1 was first described in the context of translation as having a redundant function to Ski2 in preventing the translation of mRNAs lacking a poly(A)-tail, and repressing the copy number of double-stranded RNA viruses (Searfoss and Wickner, 2000). Later, is was identified as co-fractionating with translating ribosomes similar to DRG GTPases, with both being involved in promoting efficient translation (Daugeron *et al*., 2011). With its contribution to dissociating collided ribosomes, a more specific function was identified. As part of the ASCC, the human homolog of Slh1, ASCC3, is not only involved in inducing RQC, but also fulfills a role in the nucleus where it promotes AlkBH3 mediated DNA repair in a ubiquitination dependent manner (Brickner *et al*., 2017). ASCC3 was initially characterized as a DNA helicase, unwinding DNA to provide a single-stranded substrate for the repair process (Dango *et al*., 2011).

Slh1/ASCC3 belong to the Ski2-like subfamily of super-family 2 (SF2) helicases. The family contains both RNA- (Ski2, Slh1, Brr2, Mtr4) and DNA-helicases (Hel308, DDX60, Hfm1) with a 3'-to-5' unwinding ability. Ski2-like helicases are involved in various cellular processes, from RNA decay (Ski2 and Mtr4) and pre-mRNA splicing (Brr2) to DNA repair (Hel308).

Common to all SF2 helicases is a conserved core of two RecA-like domains (RecA1, RecA2) (Singleton *et al*., 2007) containing multiple motifs responsible for RNA binding, ATP binding and hydrolysis (Figure 4). Especially motif I (Walker A, ATP binding) and motif II (Walker B, ATP hydrolysis) were identified early on as a common denominator of ATPases (Walker *et al*., 1982). For Ski2-like helicases, the RecA1-RecA2 helicase core is complemented by a winged helix (WH) and a ratchet domain. Together they form a ring-like structure around the RecA-core, which contains a β-hairpin at the helicase entrance for strand separation (Buttner *et al*., 2007; Johnson and Jackson, 2013).

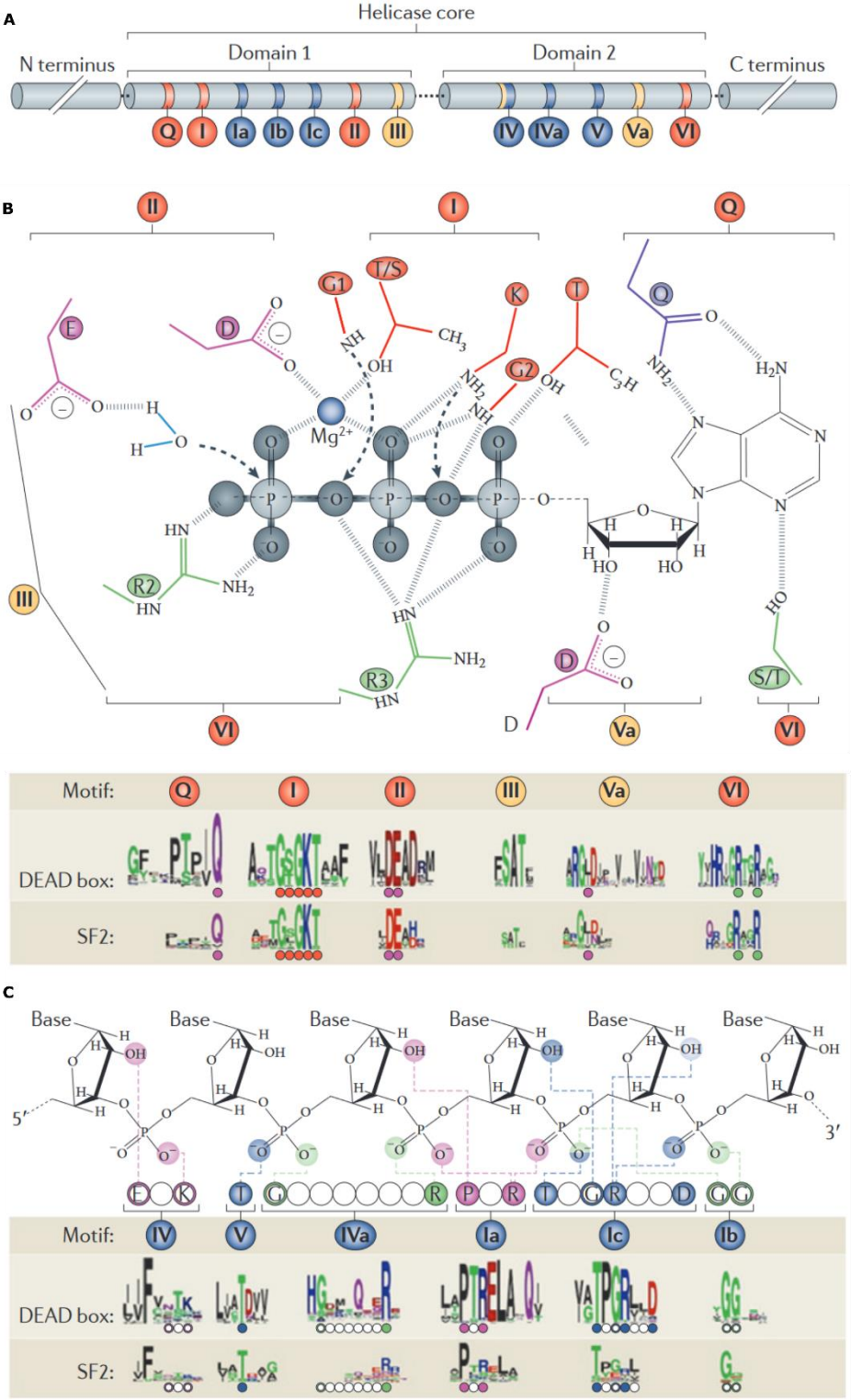

Figure 4: Architecture of the RecA1/RecA2 ATPase domain in DEAD box and SF2 family helicases.

(A) The helicase core consists of two domains, containing various motifs for ATP binding and hydrolysis (red), RNA binding (blue) and communication between the former two (yellow). (B) Representation of the conserved residues involved in ATP binding and hydrolysis. (C) Representation of residues involved in RNA binding. (Adapted from Linder and Jankowsky, 2011)

With a length of 1967 amino acids, Slh1, together with Brr2, is one of the largest members of the Ski2-SF2 helicase family. Both proteins exhibit a long N-terminal region (NTR, residues 1-220 in Slh1, 1-400 in Brr2) followed by a duplication of the basic Ski2-like helicase cassette. In addition to the RecA1, RecA2, WH and ratchet domain, the helicase cassettes contain a small helix-hairpin-helix (HhH) as well as a Fibronectin type III domain (FN3). These two domains, together with the ratchet domain are also known as the Sec63 (or Brl) domain, after the yeast protein Sec63 where they were first identified (Jermy *et al*., 2006; Ponting, 2000).

Brr2 is part of the spliceosome, and responsible for remodeling of the complex after spliceosome activation. A crystal structure of human Brr2 showed that the two helicase cassettes interact with each other (Santos *et al*., 2012), but only the N-terminal cassette was shown to be an active helicase. The C-terminal cassette retained the ability to bind, but not hydrolyze ATP, acting as a regulatory domain and enhancing the helicase activity of the N-terminal cassette (Kim and Rossi, 1999; Santos *et al.*, 2012). Further studies found regulatory contributions of the Brr2 N-terminus which contains a 'plug' and a PWI domain (Absmeier *et al*., 2015a; Absmeier *et al*., 2015b).

Although the Slh1 sequence shows high similarity to Brr2, no complete structure could be obtained so far. Overall, Slh1 matches the domain arrangement of Brr2 but has a slightly shorter N-terminus. In contrast to Brr2, the catalytic residues necessary for ATP hydrolysis and nucleic acid interaction are in principle present in both cassettes. Earlier studies examining DNA unwinding activity for the human homolog of Slh1, ASCC3, found the C-terminal cassette actively unwinding DNA (Dango *et al.*, 2011), whereas newer studies showed RNA unwinding ability mainly (but not exclusively) for the N-terminal cassette (Jia *et al*., 2020; Juszkiewicz *et al.*, 2020b; Stoneley *et al*., 2022), similar to the activity observed for Brr2. To further add to this similarity, the NTR of ASCC3 was found to auto-inhibit the helicase activity. The NTR of the ASCC3 protein was crystallized together with the N-terminal region (residues 1-434) of its co-factor ASCC2 (Cue3 in yeast), providing the very first structural insight on RQT components. The ASCC3 NTR displays a plug-like structure, which is probably responsible for helicase inhibition. It contacts the N-terminal region of ASCC2 which consists of two subdomains with each 8 α-helices (Jia *et al.*, 2020). This region is predicted to be connected to the eponymous CUE domain via a flexible linker.

Initially this domain was identified in Cue1, which is responsible for Coupling of Ubiquitin conjugation to ER degradation (Biederer *et al*., 1997; Kang *et al*., 2003). The domain itself has two surfaces that can bind ubiquitin. Due to the ubiquitin binding ability, Cue3/ASCC2 was proposed to function as an adapter for detection of Hel2/ZNF598 dependent uS10/eS10 ubiquitination by RQT. Intriguingly, while there are studies showing a dependency of RQT function on the availability of the CUE domain both for yeast and the human system (Hashimoto *et al*., 2020; Matsuo *et al.*, 2020), other studies found the CUE domain to be expendable for RQT activity (Juszkiewicz *et al.*, 2020b).

For the last co-factor, Rqt4, not much is known. It was initially identified in yeast as part of the RQT complex. It is a largely disordered zinc-finger containing protein. The human homolog TRIP4 is known to act as a transcription co-activator, facilitating nuclear receptor mediated transcription and is involved in transactivation of both the thyroid and estrogen receptor (Kim *et al*., 1999; Yoo *et al*., 2014). Deletion of Rqt4/TRIP4 only inhibits RQT activity if Cue3/ASCC2 is also not available (Matsuo *et al.*, 2017).

One alternative pathway, triggered if RQT cannot dissociate the collided ribosome to induce RQC (e.g. due to too many collisions), involves ubiquitination of eS7. In this case, ubiquitination happens via a two-step mechanism: eS7 is first mono-ubiquitinated by Not4 (Panasenko and Collart, 2012), and subsequently poly-ubiquitinated by Hel2 (Ikeuchi *et al.*, 2019). This leads to an endonucleolytic cleavage event upstream of the stalled ribosome, same as observed initially with Dom34•Hbs1. Two different positions have been proposed for this endonucleolytic cleavage. Cleavage upstream of the disome unit has been observed in the absence of Slh1, while presence of Slh1 lead to cleavage events on the mRNA usually protected by the colliding ribosome (Ikeuchi *et al.*, 2019). In contrast to this, another study found cleavage of the mRNA in the A-site of the colliding ribosome in the absence of Slh1 and identified Cue2 as the responsible endonuclease (D'Orazio *et al.*, 2019). Intriguingly, Cue2 contains at least two conserved CUE domains and up to two putative ubiquitin binding motives (UBA and CUE like), making it a likely candidate for recognition of eS7 ubiquitination (D'Orazio *et al.*, 2019). Generally, cleavage of the mRNA upstream of the stalled ribosome is thought to facilitate degradation of the collided ribosomes by Dom34•Hbs1, since the resulting substrate is a ribosome stalled on a truncated message. This could even explain the previously observed degradation of stalled ribosomes without an empty A-site by Dom34•Hbs1. So far, Cue2 was identified acting as an endonuclease, both in yeast and *C. elegans* (D'Orazio *et al*., 2019; Glover *et al*., 2020) but not in the Retic system (Juszkiewicz *et al.*, 2020b).

Another pathway, involving both RQT and ubiquitination, deals with ribosomes stalling due to mutations in the 18S rRNA. If the decoding center is mutated, initiating ribosomes are degraded via a non-functional rRNA decay (NRD) pathway. For the 60S subunit (25S NRD), this pathway has been studied previously and involved factors have been identified (Fujii *et al*., 2009; Fujii *et al*., 2012; Sakata *et al*., 2015). The knowledge on 18S NRD is more limited, only recently E3 ligase Mag2 was identified playing a role in 18S NRD, where it mono-ubiquitinates ribosomal protein uS3, which is then poly-ubiquitinated either by Hel2/Rsp5 (Sugiyama *et al*., 2019) or by Fap1 (Li *et al*., 2022). Splitting was proposed to be performed either by Dom34•Hbs1 or by the RQT complex and subsequently leads to decay of the 18S rRNA by exonuclease Xrn1 (Sugiyama *et al.*, 2019). How this pathway differs from the previously described dissociation pathways involving RQT or Dom34 is so far unclear. Nevertheless, comparing all the new pathways, licensing by ubiquitin modification of a translationally incompetent ribosome, combined with splitting as the commitment step emerges as one of the central aspects in quality control of translation.

Licensing is most likely balanced by the simultaneous action of both E3 ligases but also de-ubiquitinases (e.g., Otu2, Ikeuchi *et al*., 2021), enabling a truly specific reaction to aberrantly stalls but not translational pauses. Generally, deubiquitination is a necessary step in ribosome recycling, 'resetting' leftover signals from the previous round of translation to enable the ribosome to initiate the next round of translation.

Motivation/Aim

As described in the chapters above, a variety of new pathways targeting collided ribosomes have been discovered in the last few years. This thesis sets out to understand the process by which the RQT complex resolves stalled ribosomes and leads to subunit dissociation.

Although it has been shown that RQT is responsible for splitting after ubiquitination of collided ribosomes by E3 ligase Hel2, so far, the exact mechanism by which this splitting is achieved remains unclear. There are several open questions: How does the RQT complex exactly recognize the ubiquitinated ribosome? How does ATPase activity of the Slh1 helicase subunit lead to dissociation of the lead ribosome? Is the splitting process by RQT comparable to the one described for Dom34•Hbs1/ABCE1?

To shed light on those questions, the goal of this thesis is to solve the structure of the RQT-bound ribosomal complex by cryo-EM. To that end, a robust and reproducible *in vitro* system should be established to examine conditions and prerequisites for RQT-based splitting. The insights from these studies should then be employed to optimize a reconstitution approach for subsequent structural studies using cryo-EM. Cryo-EM represents a powerful method to investigate various states of reaction intermediates, enabling high-resolution based molecular modeling of the complex of interest. This should give insights into the mechanistic steps, involved in RQT-mediated splitting.

Methods and Materials

Amplification of template DNA

To generate stalling constructs for later *in vitro* translation reactions, plasmids containing stalling sequences were bought from eurofins (maps see Appendix). Employed sequences were either the endogenous staller *SDD1* (101-218) or the sequence of ribosomal protein Rpl4 (4-64) combined with a stretch of twelve *CGN* codons. Since both stallers have the same pEX plasmid backbone and a comparable length, the same primers and settings were used for amplification. In addition to the stalling sequence, the constructs were designed with a His-V5-TEV tag for purification and detection (see Figure 5A).

Used 5-10 ng of every construct for a PCR with phusion polymerase (Primer fw: ggccgcaagcTAATACGACTCAC, primer rev: CTTTATGCTTCCGGCTCGTATGTTG). 25 µl of a 2x phusion master mix were incubated with each 2.5 µl of forwards/reverse primer, template plasmid and nuclease free water was added to 50 µl. Amplification was performed with the following two-step program:

Table 1: 2-step PCR Program

temperature	*Duration*	*cycles*
98 °C	30 sec	
98 °C	10 sec	30 x
72 °C	45 sec	
72 °C	5 min	
12 °C	Hold	

The PCR product was purified with a Qiagen PCR purification kit. This generally yielded ~70-120 ng/µl for 2x 50 µl PCR reaction and elution in 40 µl nuclease free water (2.8 - 4.8 µg total).

In vitro transcription of mRNA

From the template PCR product, mRNA was transcribed using a mMESSAGE mMACHINE™ T7 Transcription Kit (Thermo). *In vitro* transcription reactions were set up as described in the manual, using 20 µl 2x NTP/Cap mixture, 4 µl 10x reaction buffer, ca. 300 ng of purified template PCR product, 4 µl T7 enzyme mixture and the reactions were adjusted to 40 µl with nuclease free water. After incubation at 37 °C for 2 h, mRNA was precipitated using 60 µl of the 7.5 M LiCl solution (with 50 mM EDTA) at – 80 °C for 2-3 h. The precipitated mRNA was pelleted by centrifugation (11,400 g) and washed with 70 % EtOH. After a second pelleting step and removal of EtOH, the mRNA pellet was dried at RT and resuspended in nuclease free H_2O. The concentration of the obtained mRNA was measured using a NanoDrop spectrophotometer. Yields varied, but were generally between 15-38 µg mRNA/reaction.

Preparation of cell free extract from yeast

To generate cell free extract from yeast strains (either *Δxrn1Δslh1Δcue2* or *Δski2/uS10-HA*), cells were freshly steaked on YP plates and incubated at 30 °C for 2 days. From the plate, an over-night culture was set up (ca. 50 ml, 30 °C). In the morning, the culture was diluted to an OD_{600} of 0.2, to ensure that the cells were optimally growing when setting up the cell culture in the afternoon. For the *Δxrn1Δslh1Δcue2* strain, doubling time was at approximately 2.2 h. The start OD_{600} was chosen such that the cells are at an OD_{600} of ~2 at the time of harvest. The cells were grown in 10-20 l YP medium with 2 % glucose, supplemented with both ampicillin and anti-foam. Cultures were harvested by centrifugation, resuspended in ice cold water, pooled, spun down to remove the water and pelleted. The yeast cells were either frozen as droplets in liquid nitrogen and cell walls were removed by cryogenic milling and subsequent centrifugation steps (Trainor *et al*., 2021), or cell free extract was prepared directly via preparation of spheroblasts (Waters and Blobel, 1986). For the latter method, from 20 l of cell culture, ca 65-75g cells could be harvested, resulting in 9-12 ml of translation extract with an A260 of 110-230/ml.

In vitro translation of stalling constructs

The *in vitro* translation reaction was assembled on ice and subsequently performed as described before (Ikeuchi *et al.*, 2019). To ensure ubiquitination, reactions were performed in the presence of Hel2 (68 nM) at 17 °C for 75-90 min.

Table 2: Scheme in vitro translation reaction

Component	*Volume*
Yeast translation extract	415 µl
25x CB-Mix	50 µl
12.5x E-mix	100 µl
1M Tris pH 6.8	50 µl
AA-mix (1.5 mM each)	50 µl
Anti-RNAse (20 U/µl)	25 µl
mRNA	30 µg
purified Hel2-FLAG (0.3 mg/ml)	20 µl
ad nuclease free H_2O	1250 µl

25x CB mix: 325 mM HEPES pH 7.5, 2.925 M KOAc, 45 mM $Mg(OAc)_2$, 32.5 mM DTT

12.5x E-mix: 12.5 mM ATP, 6.25 mM GTP, 1.25 mg/ml tRNA, 250 mM creatin phosphate, 1.25 mg/ml creatin kinase (in 5 mM HEPES pH 7.5)

RNC purification

Ribosome nascent chain complexes (RNCs) of ribosomes stalled on *SDD1* or *CGN12* stallers (see Results, Figure 5A) were purified from the *in vitro* translation reactions via the translated His-tag using magnetic Dynabeads (Invitrogen, #10104D). The translation reaction was applied to equilibrated beads (50 mM HEPES pH 7.5, 300 mM KOAc, 10 mM $Mg(OAc)_2$, 125 mM sucrose, 0.01 % NP-40, 5 mM β-mercaptoethanol) for 20-30 min at 4 °C, washed and eluted (10-15 min at 4 °C) in elution buffer (50 mM HEPES pH 7.5, 150 mM KOAc, 10 mM $Mg(OAc)_2$, 125 mM sucrose, 0.01 % NP-40, 5 mM β-mercaptoethanol) containing 400 mM imidazole.

Sucrose gradients

Purified RNCs were loaded on top of 10-50 % sucrose gradients (50 mM HEPES pH 7.5, 200 mM KOAc, 10 mM $(MgOAc)_2$, 1 mM DTT, 10/50 % sucrose(w/v)) followed by ultracentrifugation for 3 h at 284,000 x g. Fractions of the gradients were collected on a gradient station (Biocomp) equipped with a TRIAX flow cell (Biocomp) and a GILSON fractionator. Mono-, di- and trisome fractions were used for further experiments.

SDS-PAGE

To separate proteins according to their size, SDS-PAGE was performed using a standard protocol (Laemmli, 1970). Mainly 4-12 % Nu-PAGE gels were used in combination with 1x MOPS running buffer (50 mM MOPS, 50 mM Tris base pH 7.7, 0.1 % SDS, 1 mM EDTA). Samples containing 1x SDS-sample buffer (50 mM Tris/HCl pH 6.8, 2 % SDS, 10 % glycerol, 0.1 % bromphenol blue, 100 mM DTT) were denatured at 95 °C for 5 min (proteins) or 65 °C for 10 min (RNCs). Generally, electrophoresis was performed using a constant voltage of 160 V for ca. 90 min. To visualize proteins, gels were stained with Simply blue Coomassie staining solution (Novex).

Western Blotting

After sample separation on NuPAGE, semi dry western-blotting was performed with blotting buffer (48 mM Tris, 39 mM Glycin, 0.037% SDS, 20 % EtOH) at 75 mA/Nu-PAGE gel for 1h. The PVDF membrane was blocked with 5% skim milk in TBS for 1 h and incubated with anti-HA-HRP (Roche, 3F10, 1:5000) in 5% milk/TBS or anti-v5 (Genescript #A01724, 1:2000) in 5% milk/TBS-T. For the anti-v5-antibody, the blot was washed (1x TBS with 0.1 % (w/v) TWEEN-20, 2x TBS) and incubated 1h with goat-anti-mouse-HRP (1:5000). After washing (1x TBS with 0.1 % (w/v) TWEEN-20, 2x TBS) signal was detected with an AI-600 imager (GE Healthcare) using SuperSignal West Dura Extended Duration Substrate (Thermo).

Affinity purification of recombinant proteins

Hel2

A yeast strain overexpressing Hel2-FLAG was grown in synthetic dropout media. Cells were harvested by centrifugation and subsequently disrupted by cryogenic milling (SPEX SamplePrep 6970EFM Freezer/Mill). Cell-powder was resuspended in lysis buffer (50 mM Tris pH 7.5, 500 mM NaCl, 10 mM $Mg(OAc)_2$, 0.01 % NP-40, 1 mM PMSF/DTT, 1x cOmplete EDTA-free Protease Inhibitor Cocktail tablets (Roche, #04693132001)) and centrifuged at 30,596 x g for 30 min. The supernatant was purified using M2 FLAG affinity resin (Sigma Aldrich, #A2220). During the washing steps, the salt concentration was decreased from 500 mM NaCl to 100 mM NaCl in 100 mM steps. Hel2-FLAG was eluted by incubation of the resin with 3x FLAG peptide in elution buffer (50 mM HEPES, 100 mM KOAc, 5 mM $Mg(OAc)_2$, 1 mM DTT, 0.05% Nikkol).

eIF6

Yeast eIF6 was expressed from a p7XC3GH plasmid ((Wells *et al.*, 2020)) fused at the C-terminus to a 3C protease cleavage site, GFP, and 10× His-tag. The plasmid was transformed into E. coli Rosetta (DE3), which was grown at 37°C to mid-log phase. The temperature was reduced to 16°C, and protein overexpression was induced with 100 uM IPTG for overnight expression. Cells were harvested at an OD_{600} of 4 (4,000 × g, 4°C, 10 min), washed with phosphate-buffered saline (PBS), and resuspended in ca. 100 ml lysis buffer (20 mM Tris-HCl pH 8.0, 300 mM NaCl, 2 mM β-ME, 1x cOmplete EDTA-free Protease Inhibitor Cocktail tablets (Roche, #04693132001)) before being lysed with Microfluidics M-110L microfluidizer. Lysates were clarified by centrifugation at 30,596 × g at 4°C for 30 min. Clarified lysate from 2 l cell culture, (ca. 12 g cells) was loaded onto 2.5 ml (5 ml slurry) TALON metal affinity resin (Takara Bio) equilibrated in lysis buffer and incubated on a rotating wheel at 4°C for 1 hour. The supernatant was removed, and the resin was washed three times with lysis buffer containing 10 mM imidazole, before being incubated with ca. 6 ml elution buffer (20 mM Tris-HCl pH 8.0, 300 mM NaCl, 2 mM β-ME, 10 mM imidazole, 0.25 mg/mL 3C protease) for 30 min at 4°C. Eluted protein was concentrated to 1 mL before being loaded onto Superdex 200 (Sigma-Aldrich) for size exclusion chromatography in the final buffer (50 mM HEPES pH 7.5, 500 mM KCl, 2 mM $MgCl_2$, 2 mM β-ME).

Uba1

Uba1 was purified from yeast by Joanna Musial. A yeast strain overexpressing Uba1-FLAG (provided by Dr. Ken Ikeuchi) was grown in synthetic dropout media to an OD of 1.5. Cells were harvested and disrupted by cryogenic milling. 2.5g of cells were resuspended in lysis buffer (20 mM HEPES pH 7.6, 500 mM KCl, 5 mM $MgCl_2$, 1 mM DTT, 0.5 mM PMSF, 0.01 % NP-40, 1x cOmplete EDTA-free Protease Inhibitor Cocktail tablets (Roche, #04693132001)).

Cell debris was removed by centrifugation at 30,596 x g for 30 min. Hel2-FLAG was bound to M2 FLAG affinity resin (Sigma Aldrich, #A2220). During the washing steps, the salt concentration of the buffer was stepwise decreased to 150 mM KCl. Uba1-FLAG was eluted with 3xFLAG peptide in elution buffer (20 mM HEPES pH 7.6, 150 mM KCl, 5 mM $MgCl_2$, 1 mM DTT, 0.5 mM PMSF, 0.01 % NP-40).

Ubc4

Recombinant Ubc4 was purified by Dr. Ken Ikeuchi as a GST-Ubc4 fusion protein from *E. coli* Rosetta-gami 2 (DE3) cells harbouring the pGEX-Ubc4 plasmid essentially as described before (Ikeuchi *et al.*, 2019).

RQT complex

A yeast strain overexpressing RQT components (Slh1-FTP, Cue3, Rqt4) was grown in synthetic drop-out media. Cells were harvested by centrifugation and subsequently disrupted by cryogenic milling. Cell powder was resuspended in lysis buffer (50 mM K_2HPO_4 /KH_2PO_4 pH 7.5, 500 mM NaCl, 5 mM $Mg(OAc)_2$, 100 mM arginine, 1 mM DTT, 1 mM PMSF, 0.1 % NP-40, 1x cOmplete EDTA-free Protease Inhibitor Cocktail tablets (Roche, #04693132001)) and centrifuged at 30,596 x g for 30 min. Purification was performed on IgG-sepharose (GE Healthcare, #GE17096901) resin. The complex was eluted by TEV cleavage in RQT elution buffer (50 mM HEPES pH 7.5, 300 mM KOAc, 5 mM $Mg(OAc)_2$, 0.01% Nikkol, 1 mM DTT) for 1.5 h at 4 °C.

EDF1

Purification of EDF1 was performed by Timo Denk. To that end, HEK293 Flp-In T-Rex cells expressing EDF1 with an N-terminal 3xFLAG-3C Protease cleavage site tag (generated by Matthias Thoms) were lysed in lysis buffer (20 mM HEPES pH 7.5, 150 mM KOAc, 5 mM $MgCl_2$, 0.5% IGEPAL CA-630 (Sigma), 0.1 mM Na_3VO_4, 0.5 mM NaF, 1 mM DTT, 1x cOmplete EDTA-free Protease Inhibitor Cocktail tablets (Roche)). The crude lysate was consecutively sonicated four times for 10 s followed by 30 s on ice each. The lysate was clarified by two subsequent centrifugation steps at 2960 x g and 4°C for 15 min and 36,500 x g and 4°C for 25 min. The resulting supernatant was incubated with ANTI-FLAG M2 Affinity Gel (Sigma) at 4°C for 120 min. The affinity beads were washed twice with NP-40 washing buffer (20 mM HEPES pH 7.5, 150 mM KOAc, 5 mM $MgCl_2$, 0.01% IGEPAL CA-630 (Sigma), 0.1 mM Na_3VO_4, 0.5 mM NaF, 1 mM DTT) and once with Nikkol washing buffer (20 mM HEPES pH 7.5, 150 mM KOAc, 5 mM $MgCl_2$, 0.05% octaethylene glycol monododecyl ether, 1 mM DTT). After transferring the beads to a 1 mL Mobicol spin-column (MoBiTech) they were washed once with Nikkol washing buffer. For elution, the beads were incubated in elution buffer (20 mM HEPES pH 7.5, 150 mM KOAc, 5 mM MgCl2, 0.05% octaethylene glycol monododecyl ether, 1 mM DTT, 0.352 mg/mL 3C Protease (homemade)) at 4°C for 60 min. The eluate was collected by centrifugation and subjected to cryo-EM.

In vitro ubiquitination of RNCs

The *in vitro* ubiquitination reaction was performed essentially as described before with adjustments (Ikeuchi *et al.*, 2019). 10-15 pmol of purified RNCs, or isolated di-/trisomes were incubated with 57 µM ubiquitin, 116 nM UBE1 (R&D systems) or Uba1, 3.3 µM Ubc4 and 757 nM Hel2 in reaction buffer (20 mM HEPES-KOH pH 7.4, 100 mM KOAc, 5 mM $Mg(OAc)_2$, 1 mM DTT, 1 mM ATP, 10 mM creatine phosphate, 20 ug/ml creatine kinase (Roche)) at 25 °C for 30 min. Ubiquitinated ribosomes were either used directly in *in vitro* splitting assays or pelleted through a sucrose cushion (50 mM HEPES pH 7.5, 100 mM KOAc, 25 mM $Mg(OAc)_2$, 1 M sucrose, 0.1 % Nikkol) in a TLA110 rotor (Beckman Coulter) at 434,513 x g for 1.5 h at 4 °C, for the subsequent preparation of cryo-EM samples.

In vitro reconstitution of splitting reactions

6-12 pmol of RNCs (ubiquitinated or non-ubiquitinated) were incubated with 10x molar excess of RQT complex and 5x molar excess of eIF6 for 15 min at 25 °C. For control reactions without RQT, RQT elution buffer (50 mM HEPES pH 7.5, 300 mM KOAc, 5 mM $Mg(OAc)_2$, 0.01% Nikkol, 1 mM DTT) was added instead. The reactions were separated on a 10 – 50 % sucrose gradient using ultracentrifugation in a SW40 rotor for 3 h at 284,000 x g.

Crosslinking and Northern Blot of splitting reactions

For analysis of the RQT-mRNA interaction, 4-thio-uridine (4SU) containing mRNA was generated by addition of 7.5 mM 4SU to the *in vitro* transcription reaction. 8 pmol of ubiquitinated RNCs (stalled on CGN12 or CGN12-4SU mRNA) were incubated with a 10x molar excess of purified RQT complex at room temperature for 5 min. After crosslinking with UVA, samples were affinity-purified using M2 FLAG affinity resin (Sigma Aldrich, #A2220). Binding of Slh1-ribosome complexes to the beads was performed in binding buffer (50 mM HEPES pH 7.5, 200 mM KOAc, 100 mM arginine, 125 mM sucrose, 1 mM PMSF) at 4 °C for 1 h. After two washing steps with binding buffer, again two washing steps with either 4 mM ATP or 5 mM EDTA were performed. Samples were eluted by addition 3xFLAG peptide in elution buffer (50 mM HEPES, 100 mM KOAc, 62.5 mm sucrose, 1 mM DTT). To remove remaining protein, samples were treated with proteinase K in ProtK buffer (100 mm Tris-HCl pH 7.5, 50 mm NaCl, 10 mM EDTA pH 8) at 37 °C for 20 min at a concentration of 1 mg/ml. Subsequently, equal volume of ProtK buffer containing 7 M urea was added for further incubation at 37 °C for 20 minutes. After addition of TRI reagent (Zymo Research #R2051), RNA was extracted using a Direct-zol Mini Prep kit (Zymo Research #R2051).

Northern Blotting

6 µL of purified RNA was mixed with 19 µL of RNA loading buffer (30 mM Tricine, 30 mM Triethanolamine, 0.5 M formaldehyde, 5%v/v glycerol, 1 mM EDTA, 0.005%w/v Xylene cyanole, 0.005%w/v bromophenol blue in deionized formamide) and incubated at 65 °C for 5 min followed by resting on ice for 5 min. RNA was separated on a 1.2 % agarose gel with 1x TT buffer (30 mM Tricine, 30 mM Triethanolamine, pH 7.9 in 50X stock) by electrophoresis at 120 V for 100 min, followed by capillary transfer onto a Hybond-N+ membrane (cytiva #RPN303B) using 20X SSC (3 M NaCl, 300 mM Sodium citrate). Hybridization was performed at 52ºC using DIG-labeled R(CGN)12 probe (5'-DIG-GCGGCGCCGTCGTCGCCGGCGGCGCCGTCGTCGCCGTTCCCAGGATTCAG-3') and DIG easy hyb granules (Roche # 11796895001) and incubated in hybridization oven for 20 hours. The membrane was washed once for 15 minutes by 2X SSC 0.1% SDS, twice for 15 minutes each by 0.1X SSC 0.1%SDS in the oven, then incubated in blocking reagent (Roche #11096176001) for 30 minutes and with 1/10,000 anti-digoxigenin-AP (Roche #11093274910) for 1 hour at room temperature. After washing membrane three times by wash buffer (100 mM maleic acid, 150 mM NaCl, 0.3% Tween-20, pH 7.5) and once by pre-detection buffer (0.1 M Tris-HCl pH 9.5, 0.1 M NaCl), RNA was detected via chemiluminescence using CDP star reagent (Roche #11759051001) on a AI-600 mini (GE healthcare) for 24 min.

Cryo-EM of SDD1 stalled trisomes and EDF1-ribosome complexes

SDD1-stalled ribosomes were generated and purified as described previously (Matsuo *et al*., 2020). The purified RNCs were applied to a 10–50% sucrose gradient, and ribosomal fractions were separated via centrifugation for 3 h at 202,048 x g at 4°C in a SW40 rotor.

Freshly prepared samples of the EDF1-80S or SDD1 trisome fraction were applied to holey carbon support grids (R3/3 with 2 nm continuous carbon support, Quantifoil), which had been glow discharged at 2.1 × 10^{-1} mbar for 20 s. Grids were incubated for 45 s at 4°C and subsequently plunge frozen in liquid ethane using a Vitrobot Mark IV (FEI Company). Data were collected on a Titan Krios at 300 kV using a K2 Summit direct electron detector (Gatan) with a nominal pixel size of 1.059 Å and a defocus range from 0.5 to 2.5 µm at low-dose conditions. For each movie, 40 frames with approximately 1.12 e- $Å^{-2}$ exposure were gain corrected and aligned using MotionCor2 (Zheng *et al*., 2017). Contrast-transfer function (CTF) parameters of the summed micrographs were estimated with Gctf (Zhang, 2016), before micrographs were manually screened for quality.

The EDF1-80S data set was processed using Relion 3.1 (Zivanov *et al*., 2018). After two-dimensional (2D) classification, 95,832 particles from 4260 micrographs were subjected to a 3D classification. First, 80S states and low-resolution particles of the ribosome were separated in five 3D classes. Approximately 85% of the particles represented post-state ribosomes with high EDF1 occupancy which were refined to an overall resolution of 3.1 Å.

Post-processing, CTF corrections and a focused refinement with a soft mask around the 40S subunit yielded an overall resolution of 2.9 Å and improved the density of EDF1 for interpretation. This map was filtered according to local resolution with a negative B-factor of 20 and used for model building.

The SDD1 trisome data set was processed as an 80S dataset in Relion 3.0 and Relion 3.1 (Zivanov *et al*., 2018). In brief, individual 80S particles were picked using the Laplacian of Gaussian mode of Relion Autopicker and subjected to 2D classification. A total 398,371 particles from 4109 micrographs were selected after 2D classification. Initial refinement followed by masked 3D classification into five classes were performed, with the 3D classification focusing on differentiating between tRNA states. Of the observed ribosomes, 23% were occupied by P/P tRNA, 64% by A/P, P/E tRNA (in three classes) and 13% had A-site tRNA. The three classes representing rotated ribosomes with A/P and P/E tRNAs were merged for further processing. Sub-classification of these ribosomes into three classes with a mask around the 40S beak and rRNA helix 16 yielded one class (31%) with extra density where helix 16 was shifted compared to the other classes. After CTF-refinement and subsequent sub-classification into two classes, one well resolved class with 77% of the particles was observed. Focused 3D refinement with a soft mask around the 40S subunit yielded a map with an overall resolution of 3.0 Å which was filtered according to local resolution with a negative B-factor of 30 and used for model building.

To generate molecular models, previously refined models of stalled yeast and human 80S ribosomes (Thoms *et al*., 2020) (PDB 6ZMI) and the yeast disome (Ikeuchi *et al*., 2019) (PDB 6I7O) were used. First, individual subunits and tRNAs were fitted as rigid bodies into the densities. These models were then remodeled in COOT (Emsley *et al*., 2010) and refined in Phenix (Adams *et al*., 2010). Cryo-EM structures and models were displayed using UCSF ChimeraX (Goddard *et al*., 2018).

Cryo-EM of RQT-ribosome complexes

To generate suitable samples for cryo-EM, at least 6 pmol of ubiquitinated disomes were incubated for 5 min at 25 °C with 12 pmol of purified RQT complex in the presence of 1 mM ATP. After incubation, 3.5 µl of samples were vitrified in liquid ethane on glow discharged, R3/3 copper grids with a 2 nm carbon coating (Quantifoil) using a Vitrobot mark IV (FEI) with 45 s wait time and 2.5 s blotting time.

Altogether four samples were analyzed, two pre-splitting reactions and two post-splitting reactions. Pre-splitting reactions contained either ubiquitinated *CGN6*-stalled disomes (with short accessible 3'-mRNA, see Figure 10A) and wild type RQT (RQTwt) or (ubiquitinated) *CGN12*-stalled disomes (with long accessible 3'-mRNA) and the RQT mutant containing K316R-Slh1 (RQT*) as well as eIF6. Post-splitting reactions contained ubiquitinated *CGN12*-stalled disomes and wild type RQT, one reaction with and one without eIF6.

For the post-splitting sample (with *CGN12*-stalled disomes and RQTwt without eIF6 addition) sample, 21.171 movies were collected on a Titan Krios with a K2 Summit DED, at 300 keV with a pixel size of 1.045 Å/pixel. The applied electron dose was approximately 1.09 e-/Å/frame for 40 frames and data were collected in a defocus range between 0.5-3.5 µm. All frames were gain corrected, aligned and subsequently summed using MotionCor257,58. Downstream data processing was performed using CryoSPARC (v.3.3.1) (Punjani *et al.*, 2017). The CTF was estimated using gCTF and CTFFIND (Rohou and Grigorieff, 2015; Zhang, 2016), followed by particle picking via CryoSPARCs blob picker. After 2D classification, 2.415.630 particles were used for 3D refinement. Subsequent rounds of classification were carried out using 3D Variability Analysis with a soft mask around the ribosomal 40S subunit. Subsequent sorting steps with a soft mask around the RQT complex yielded two classes containing RQT in two distinct conformations (C1 and C2). The class of 80S ribosomes with RQT bound in C1 contained 194.186 particles (8 % of total particles) and was refined to an overall resolution of 2.4 Å. Subtracted particles of RQT were locally refined to a resolution of 3.5 Å. The second class of 80S with RQT bound in C2 contained 20.380 particles and was refined to an overall resolution 3.0 Å. Local refinement was carried out as for C1 and resulted in a resolution of 4.8 Å. The other three samples were vitrified and cryo-EM data were obtained as described above. For the CGN12/RQT* pre-splitting sample, 11.251 movies were collected with an applied electron dose of approximately 1.09 e-/Å/frame for 40 frames. For CGN6/RQTwt/eIF6 pre-splitting sample, 16.508 movies were collected with an applied electron dose of approximately 1.1 e-/Å/frame for 40 frames. For CGN12/RQTwt/eIF6 post-splitting sample, 14.092 movies were collected with an applied electron dose of approximately 1.16 e-/Å/frame for 40 frames. Downstream processing was performed using CryoSPARC (v3.3.1).

The RQT-ribosome C1 model was prepared by rigid body docking the model for SDD1-stalled 80S (PDB code 6SNT11) and the models predicted by Alphafold (Jumper *et al.*, 2021; Varadi *et al.*, 2022) for RQT components Slh1 (Uniprot-ID P53327), Cue3 (Uniprot-ID P53137) and Rqt4 (Uniprot-ID P36119). For Slh1, the N-terminal and C-terminal cassettes (NTC; residues 217-1122 and CTC residues 1123-1967) were docked individually. For Cue3 only the N-terminal part (residues 1-297) and for Rqt4, two parts (residues 171-219 and 323-381) were docked. To obtain the RQT-ribosome C2 model, 60S, 40S and RQT of the RQT-ribosome C1 model were individually rigid-body docked into the cryo-EM density. For the collided ribosomes, 40S and 60S of the SDD1 stalled 80S model (PDB code 6SNT) were docked individually. tRNAs were taken from the model of the yeast disome (PDB code 6I7O)17 and rigid body docked into the A/P, P/E site densities.

A 60S model was prepared by docking the model for NatA-bound 60S (PDB code 6HD7) into the cryo-EM density. tRNA was taken from 6SNT, eIF6 from PDB code 1G6264

Adjustment of all models was performed using Wincoot (v.0.9.6)(Emsley *et al.*, 2010) and subsequently real-space refined using Phenix (1.19.1)(Adams *et al.*, 2010). To obtain molecular models, cryo-EM densities were displayed in ChimeraX (v.1.3)(Goddard *et al.*, 2018).

Results

Characterization of the RQT dependent ribosomal rescue process

Although ribosomal rescue by the RQC system was extensively studied in the last few years, how this process is triggered remains poorly understood. Especially the mechanism, how RQT leads to ribosome dissociation, and how its helicase activity may contribute to the process is still elusive. The established model is that RQT recognizes ubiquitinated collided ribosomes by interaction of the Cue3 CUE domain with the poly-ubiquitin chain added to uS10 by Hel2. Although both Rqt4 and Cue3 are not essential for the dissociation reaction on their own, deletion of both disrupts the dissociation activity of RQT. To understand the splitting process, this thesis sets out to visualize the RQT-ribosome complex *in vitro*. Substrate ribosome nascent chain complexes were generated by *in vitro* translation on problematic messages such as the endogenous RQT substrate *SDD1* and a *CGN12* message, harboring consecutive problematic codons. Such substrates were then reconstituted with purified RQT to characterize the dissociation process.

Generation of substrates for RQT mediated dissociation

To generate a suitable substrate for ribosome dissociation by the RQT complex, collisions were induced by *in vitro* translation of specific mRNA constructs in a cell-free *S. cerevisiae* translation system. The mRNAs (Figure 5A) were designed with an N-terminal His6 tag followed by a V5 tag for detection and a tobacco etch virus (TEV) site for cleavage of the tag. This was either followed by the stall inducing sequence of endogenous RQT substrate Sdd1 (101-218) or by the sequence of ribosomal protein Rpl4A (4-64) followed by a stretch of hard-to-decode CGN (N = A, C or G) codons. To prevent degradation of stalled ribosomes during the *in vitro* translation process, yeast strains with knock outs in quality control factors were used (*Δxrn1Δslh1Δcue2*, (D'Orazio *et al.*, 2019). Purified E3 ligase Hel2 (Figure 5B) was added to the *in vitro* translation reactions to ubiquitinate the generated stalled ribosomes. If visualization of the ubiquitination was necessary, a strain with HA-tagged ribosomal protein uS10 was employed. Stalled ribosomes were purified via the N-terminal His6-tag on the nascent chain, separated by Nu-PAGE and analyzed on a Western Blot (Figure 5C). The size and composition of obtained RNCs was subsequently analyzed by sucrose density gradient centrifugation (Figure 5D).

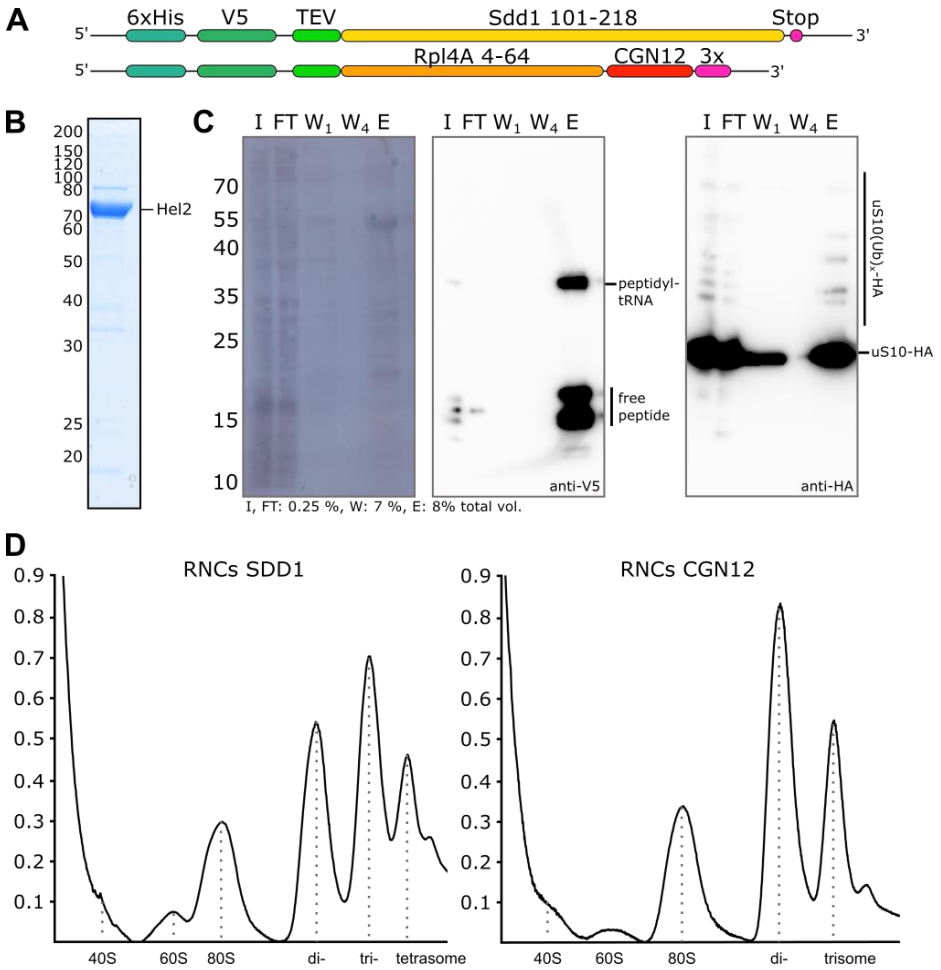

Figure 5: Preparation of ubiquitinated, collided RNCs.

(A) Scheme of the stalling constructs used for in vitro translation (B) Western Blot of the SDD1-RNC preparation. Left: PVDF membrane after Amidoblack staining, Middle: Blots against V5-tag, Right: Blot against HA-tag. I: Input, FT: Flow-through, W: Washes, E: Elution. Fraction of total volume applied to the Gel/Membrane: I, FT: 0.25 %, W1/4: 3 %, E: 8 %. V5-signals for peptidyl tRNA and free peptide are visible in the Input and Elution fractions. HA-signal for uS10 is visible in the input, flow through, first wash and elution fractions. Above the strong signal for uS10, a signal pattern for ubiquitinated uS10 is visible. (C) SDS-PAGE of purified E3 ligase Hel2. (D) Analysis of purified RNCs on a 10 – 50 % sucrose gradient. For both SDD1 and CGN12 message, stalled RNCs were generated. The polysome profile shows distinct peaks for single (80S) ribosomes as well as collided di- and trisomes.

During RNC preparation, stalled ribosomes were successfully enriched (Figure 5C, lane I and E). A subset of the obtained RNCs was also mono- or di-ubiquitinated (Figure 5C, lane E anti-HA), a prerequisite for efficient dissociation by the RQT complex. Analyzing the pattern of ribosomes in the gradient (Figure 5D), we found low amounts of 40S and 60S subunits, single 80S ('monosomes'), as well as collided ribosomes, visible as di- and trisome (and in some cases even tetrasome) peaks. Both stalling with *SDD1* and *CGN12* led to collisions, generally producing ~40-60 pmol of stalled ribosomes from reactions with 2 ml of cell free extract. Due to higher yields, mainly the obtained *CGN12* collided ribosomes were used in subsequent reconstitutions with the RQT complex. However, initial cryo-EM analysis of the *SDD1*-RNCs lead to the discovery of Mbf1 (discussed below).

Characterization of RQT mediated dissociation

The RQT complex was purified from a yeast strain over-expressing all three RQT components. Only the large helicase component Slh1 was tagged, ensuring that the co-purified proteins actually formed a stable complex. The affinity-purified complex was analyzed on a stained Nu-PAGE gel, verifying the presence of all three components. From 0.5 g of yeast cells, ca. 250 µg of the complex could be purified (Figure 6A). Purified CGN12 RNCs were incubated with a 5 – 20-fold molar excess of purified RQT in the presence of ATP to induce ribosome dissociation. The reaction was analyzed by sucrose gradient centrifugation, and Slh1 migration was visualized via Western Blot (Figure 6B).

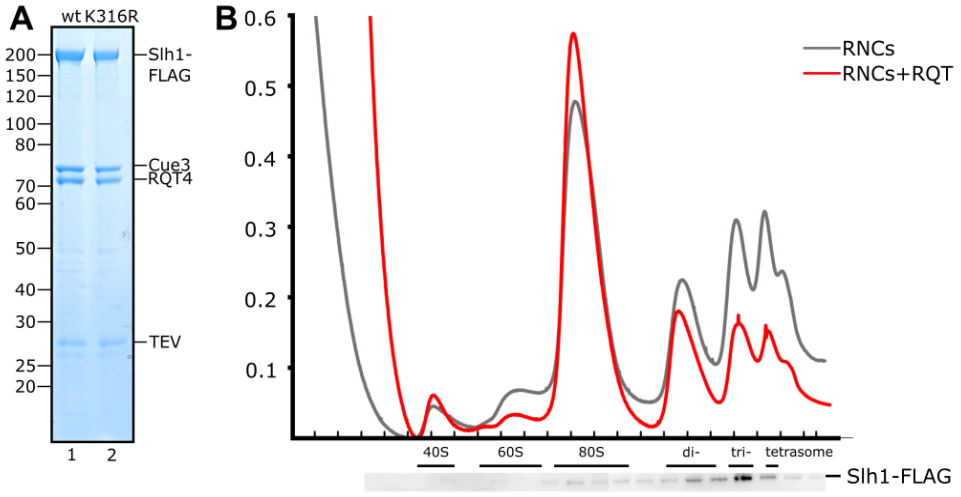

Figure 6: Dissociation of collided ribosomes by RQT.

(A) Nu-PAGE of purified RQT complex components Slh1, Cue3 and Rqt4. Tagged Slh1 (either wild type, lane 1 or with a N-terminal Walker A mutation, K316R, lane 2) was purified from yeast cells. Both Cue3 and Rqt4 co-purified with Slh1, confirming the assembly of a RQT complex. (B) Polysome profile of RQT incubated CGN12 RNCs on a 10 – 50 % sucrose gradient. Both profiles show distinct peaks of ribosomal subunits (40S and 60S) as well as single (80S) ribosomes and di- or trisomes. For RNCs incubated with RQT and ATP prior to centrifugation, polysome peaks are decreased and the 80S peak increased. Analysis of the fractions via Western Blot, showed that Slh1 co-migrates with the ribosomes and is enriched on trisomes.

Incubation with RQT complex prior to centrifugation, led to Slh1 co-migrating with the ribosomes, with an enrichment of Slh1 observed in the trisome fraction (Figure 6B). Comparing samples treated with and without RQT, a decrease of signal was visible for all collided ribosome fractions, while the amount of observed 80S monosomes was increased. Although dissociation occurred, using such reconstitutions to generate a sample for cryo-EM did not result in a visible RQT-ribosome structure.

Dissociation of *in vitro* ubiquitinated RQT substrates

The initial results shown above, suggested that while RQT seems to be actively dissociating collided ribosomes, the dissociation reaction only targets part of the obtained RNCs. To increase the amount of 'splitting-competent' RNCs, an *in vitro* ubiquitination step was introduced prior to reconstitution of the RNCs with RQT. The *in vitro* ubiquitination reaction was performed as described before (Ikeuchi *et al.*, 2019). Fractions of collided di- or trisomes were isolated after sucrose gradient separation, and subsequently incubated with ubiquitination factors (ubiquitin, E1 enzyme UBE1, E2 enzyme Ubc4 and E3 ligase Hel2). The efficiency of ubiquitination was tracked by Western Blot analysis. Splitting reactions with ubiquitinated ribosomes were performed in the presence of ATP with purified wild-type RQT or an ATPase deficient Slh1 mutant (K316R, RQT*).

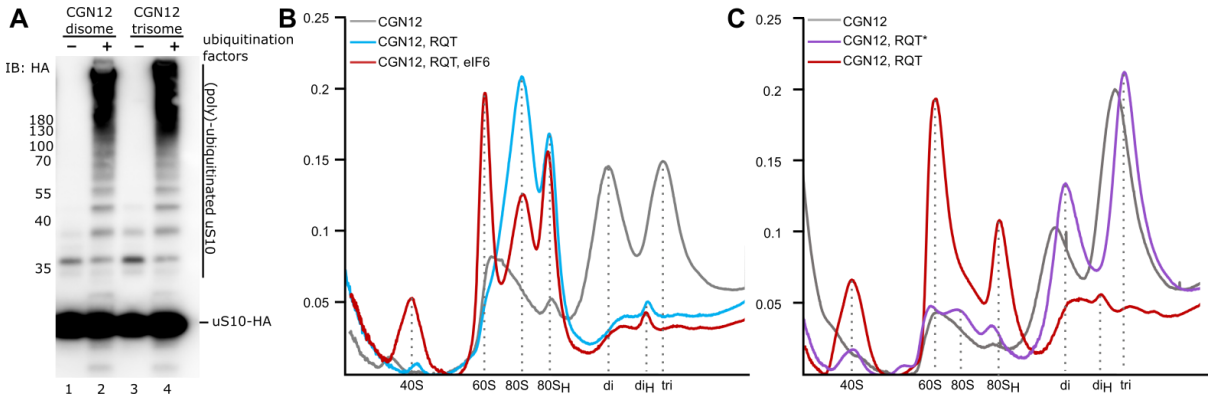

Figure 7: In vitro ubiquitination and splitting assays.

(A) The efficiency of in vitro ubiquitination of isolated di- and trisomes was analyzed on a Western Blot. Collided ribosomes were obtained from a yeast strain expressing HA-tagged ribosomal protein uS10. The base-line uS10 signal is comparable for all fractions. After isolation, modified disomes are mostly monoubiquitinated (lane 1) while trisomes showed mono- and di-ubiquitination (lane 3). After the ubiquitination treatment (lane 2 and 4), the amount of ubiquitination is severly increased, showing strong signals for polyubiquitinated uS10. (B) Polysome profiles of ubiquitinated di- and trisomes after incubation with RQT. Grey: control RNCs without RQT, light blue: RNCs incubated with RQT, red: RNCs incubated with RQT in the presence of anti-association factor eIF6. While the control showed two distinct peaks for ubiquitinated di- and trisomes, those peaks collapsed into a monosome peak with a shoulder upon RQT treatment. In case eIF6 was added, this monosome peak actually separated into 40S and 60S subunit peaks, proving that RQT is actually splitting ubiquitiated collided ribosomes. All subsequent splitting assays were performed in the presence of eIF6 (C) Polysome profiles of ubiquitinated di- and trisomes after incubation with ATPase deficient RQT. Grey: control RNCs without RQT, purple: RNCs incubated with ATPase deficient RQT (Slh1K316R), red: positive control of RNCs incubated with wild-type RQT. While wild-type RQT lead to efficient dissociation, incubation with ATPase deficient RQT did not have an effect on the ubiquitinated di- and trisomes.

In vitro ubiquitination of isolated di- and trisomes was extremely efficient. While the isolated ribosomes prior to ubiquitination were only mono-, or diubiquitinated (Figure 7A, lane 1 and 3), ribosomes that underwent the ubiquitination treatment showed efficient addition of long poly-ubiquitin chains to ribosomal protein uS10. Ubiquitinated ribosomes were then reconstituted with RQT complex and analyzed after separation on a sucrose density gradient (Figure 7B and 7C).

Incubation of ubiquitinated ribosomes with RQT resulted in a near complete collapse of di- and trisome peaks, accompanied by an increase in the 80S monosome peak. Interestingly, after successful dissociation, the monosome peak features a distinct 'shoulder peak', most likely formed by 80S-40S complexes ('halfmers'). Addition of anti-association factor eIF6 to the reaction resulted in a separation of the monosome peak (but not the shoulder peak) into 40S and 60S subunits, proving that RQT dissociates collided ribosomes by splitting them into subunits. Repeating the same experiment with the ATPase deficient Slh1K316R (RQT*) mutant did not result in any splitting activity, consistent with previously published studies (Juszkiewicz *et al.*, 2020b; Matsuo *et al.*, 2017; Matsuo *et al.*, 2020). To further characterize the splitting reaction, the assays were repeated with ubiquitinated monosomes, this time also monitoring the ubiquitination distribution.

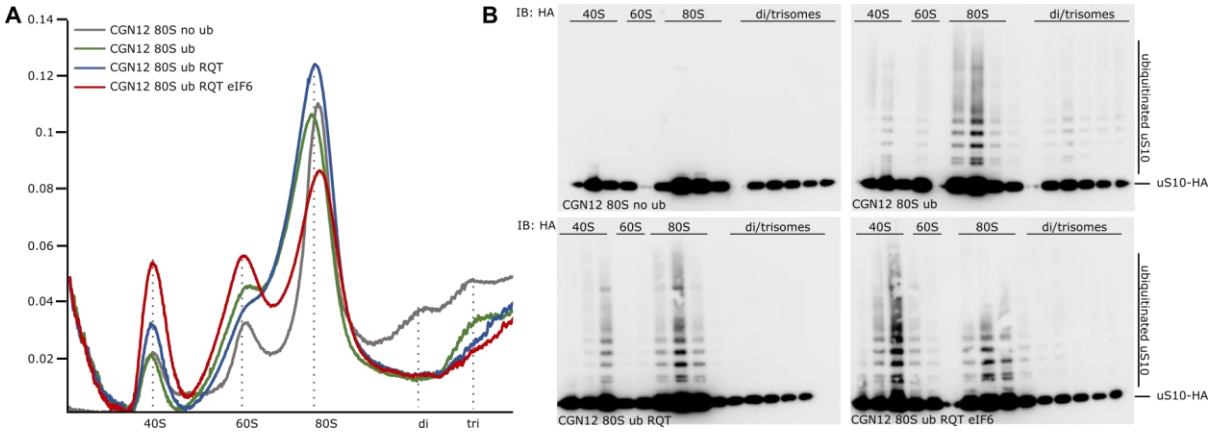

Figure 8: Splitting of ubiquitinated monosomes by RQT.

(A) Polysome profiles of CGN12 stalled 80S monosomes obtained from a yeast strain expressing HA-tagged ribosomal protein uS10. Grey: control RNCs without ubiquitination, green: ubiquitinated RNCs, blue: ubiquitinated RNCs incubated with RQT, red: ubiquitinated RNCs incubated with RQT and eIF6. Addition of RQT slightly decreases the monosome peak, with a simultaneous increase in 40S and 60S subunits. (B) Western Blots analyzing the ubiquitination pattern, corresponding to the gradients on the left. Top left: control RNCs without ubiquitination, top right: ubiquitinated RNCs, bottom left: ubiquitinated RNCs incubated with RQT, bottom right: ubiquitinated RNCs incubated with RQT and eIF6.

The polysome profile of control 80S showed one strong peak for 80S ribosomes, and slight peaks for ribosomal subunits, or di- and trisomes (Figure 8A). The monosome peak was decreased after incubation with RQT (and eIF6), again accompanied by an increase in the subunit peaks. However, the monosome-peak did not show a complete collapse similar to the previously examined di- and trisomes. On the basis of the ubiquitination pattern, not only collided ribosomes are efficiently ubiquitiated *in vitro*, but also 80S and single 40S subunits will be modified (Figure 8B, top, right). By addition of RQT, the ubiquitination pattern in the di- and trisome fraction disappears completely and shifts to the 40S fraction (Figure 8B, bottom, left). In accordance to the previous di- and trisome results, this effect is even more pronounced if eIF6 is added (Figure 8B, bottom, right).

Interestingly, ubiquitinated monosomes are still present after incubation with RQT even in the presence of eIF6, indicating that 80S ribosomes are not as efficiently split by RQT. However, in

the western blot the remaining ubiquitinated monosomes seem to miss the higher molecular weight signals, compared to the ones that did get split.

Biochemical analysis of mRNA dependency

Slh1, the largest component of the RQT complex, consists of two helicase cores. Homologs of Slh1 such as Brr2 or Ski2 were shown to possess 3'-to-5' helicase activity, in the case of Ski2 extracting mRNA from the ribosome, suggesting that Slh1 may proceed in a similar manner. To figure out if the RQT complex interacts directly with the mRNA, RNA-protein crosslinks were performed and analyzed via Northern Blotting (performed by Dr. Ken Ikeuchi). To that end, ribosomes were stalled on the previously used CGN_{12} mRNA and a freshly prepared 4-thio-uridine (4SU) containing CGN_{12} mRNA. Isolated trisomes were ubiquitinated, followed by reconstitution with RQT in the presence of ATP, similar to the previous splitting reactions. Instead of analysis by sucrose gradient centrifugation, the reactions were subsequently cross-linked using UVA light, forming specific links between 4SU in the mRNA and interacting protein. From the samples, Slh1 was affinity-purified and the associated mRNA analyzed on a Northern Blot (Figure 9). Affinity purification of samples without crosslink or RQT already contained traces of mRNA (Figure 9, lane 1), however, the amounts were increased in the RQT-containing sample (Figure 9, lane 2). This effect was even stronger for the cross-linked samples (Figure 9, lane 3 and 4), indicating that there is indeed a direct RQT-mRNA interaction.

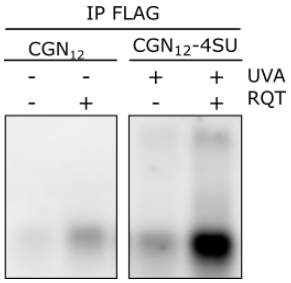

Figure 9: RQT mRNA interaction.
The RQT splitting reaction was performed with in vitro ubiquitinated ribosomes stalled either on CGN12 mRNA or CGN12 mRNA containing 4-thio-uridine. The 4SU samples were cross-linked via UVA and subsequently affinity purified via the SLh1-FLAG tag. The presence of mRNA was detected via Northern blotting. For both samples, mRNA was enriched in the presence of RQT, with a stronger effect for the cross-linked sample.

To further characterize the splitting activity, especially regarding the mRNA interaction, different mRNA constructs were prepared. While the previously used mRNA construct contained twelve stalling CGN codons, followed by a 3' region, the new constructs were truncated after four or six CGN codons, respectively (Figure 10A).

Stalling on CGN codons was previously shown to occur on the second or third CGN codon (Matsuo *et al.*, 2017), thus, the shorter constructs do not have an accessible 3' mRNA region emerging from the ribosome. The new constructs were successfully used in *in vitro* translation reactions and trisomes were isolated, ubiquitinated and used in RQT splitting assays, as described for the full-length mRNA construct (Figure 10B).

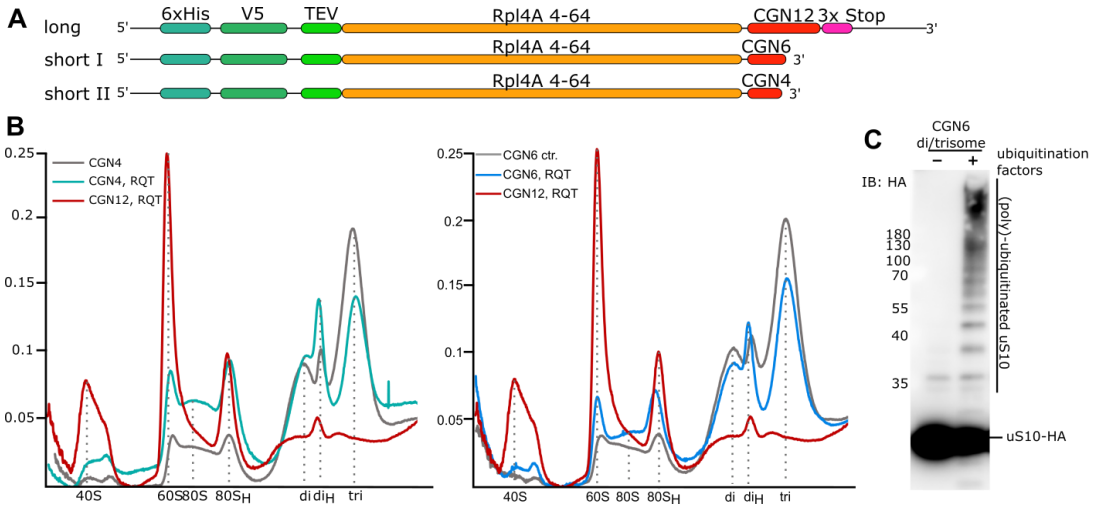

Figure 10: mRNA dependency of the splitting reaction.

(A) Schemes of employed mRNA constructs (B)Polysome profiles of splitting reactions analyzed on a 10 – 50 % sucrose gradient. Left: splitting reactions with an mRNA construct truncated after four CGN codons. Grey: negative control of ubiquitinated CGN4 stalled ribosomes without RQT, red: positive control of full-length mRNA incubated with RQT, teal: ubiquitinated CGN4 RNCs incubated with RQT. Right: splitting reactions with an mRNA construct truncated after six CGN codons. Grey: negative control of ubiquitinated CGN6 stalled ribosomes without RQT, red: positive control of full-length mRNA incubated with RQT, teal: ubiquitinated CGN6 RNCs incubated with RQT. (B) Western Blot of isolated CGN6 stalled di- and trisomes before and after the ubiquitination reaction. In vitro translation was performed in a yeast strain containing HA-tagged uS10. The ubiquitination reaction efficiently adds poly-ubiquitin chains to the obtained ribosomes.

Control reactions of ubiquitinated CGN_{12} stalled ribosomes, with an accessible 3' end, were again effectively dissociated by RQT. However, for the new constructs this splitting activity was abolished, even though they were still ubiquitinated efficiently (Figure 10C), showing that the observed splitting activity by RQT is indeed dependent on accessible mRNA.

Structure of RQT-ribosome complexes

The newly established splitting assays with *in vitro* ubiquitinated ribosomes showed a drastically increased efficiency compared to the ones performed without *in vitro* ubiquitination step. To understand the mechanism of the splitting process, we set out to visualize reconstituted RQT-ribosome complexes using *in vitro* ubiquitinated ribosomes. To decrease the amount of structural complexity, disomes (the minimal collision unit) were used. Similar to the reconstitution for splitting assays, RQT was added to ubiquitinated disomes in the presence of ATP. After short incubation, samples were directly flash-frozen on EM grids in the hope to obtain reaction intermediates. Both wild-type and ATPase deficient RQT were used, as well as CGN_{12} and CGN_6 stalled ribosomes. Data were collected on a Titan Krios with a K2 Summit DED. In total four datasets were analyzed (Table 3).

Table 3: Collected Datasets

Dataset	*Number of Micrographs*
RQT_{wt} CGN_{12}	21,171
RQT_{wt} CGN_{12} eIF6	14,092
RQT_{K316R} CGN_{12} eIF6	11,251
RQT_{wt} CGN_6 eIF6	16,501

Data processing

After gain correction and alignment, micrographs were summed using MotionCor2. Downstream processing and sorting was performed with cryoSPARC (V 3.3.1, Figure 11). For CGN_{12} stalled disomes with RQTwt, 2,415,630 particles were obtained after initial 2D classification. 3D classification into five classes showed ribosomes in both rotated PRE and non-rotated POST state, some with density for neighboring ribosomes, as previously observed for di- and trisome structures. Interestingly, a sub-population of ribosomes exhibited extra density near the mRNA entry region. Further classification and sub-sorting revealed two distinct ribosome states with such extra density, which could be assigned to the RQT complex. In total, 194,186 particles (~8 % of total particles) contributed to the first state (termed C1), in which the ribosome adopts a POST state with a P/P-site tRNA. In the second state (C2), the head of the small ribosomal subunit is swiveled relative to the 40S body and the tRNA is in a chimeric pe/E-position, corresponding to a translocation intermediate state (POST-TI-2, (Flis *et al.*, 2018)). State C2 contains 20,380 particles, ca. 0.8 % of the total particles after 2D classification.

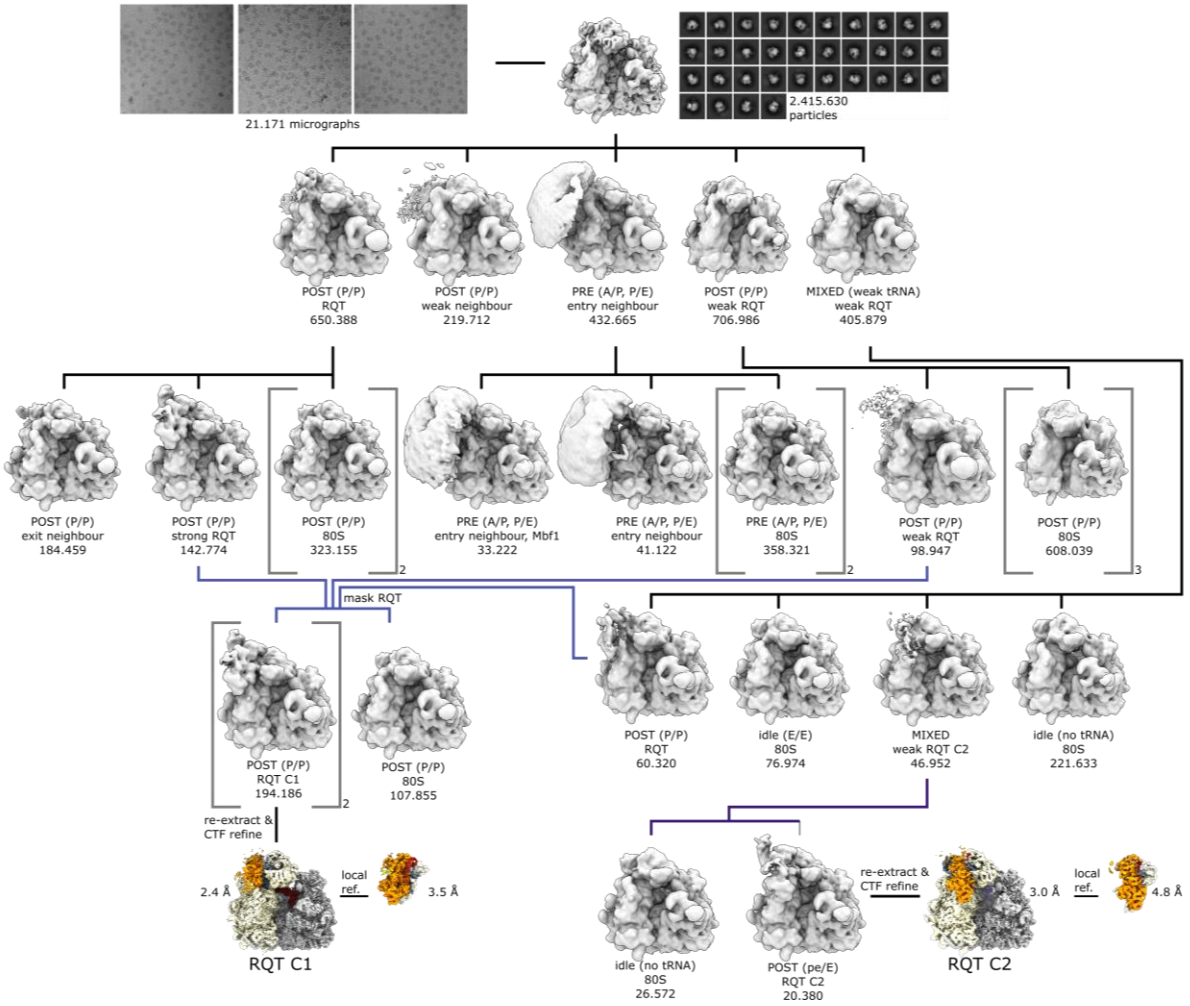

Figure 11. Classification of the RQT-ribosome dataset.

From a total of 21,171 micrographs, 2.41 million ribosomal particles were selected after 2D classification and a consensus refinement was performed. This was followed by exhaustive heterogeneity assessment using the CryoSPARC-2 3D variability analysis tool. Five main ribosomal classes were distinguished. They represented ribosomes in the non-rotated post-translocational (POST) state with a P/P site tRNA, rotated pre-translocational state (PRE) with hybrid A/P-P/E tRNAs, and mixed classes with low-tRNA occupancy and low-resolution. Individual classes also differed in presence or absence of a neighboring ribosome, either on the mRNA entry site (mostly for hybrid state 80S) or the mRNA exit site (mostly for POST state 80S) and extra density for RQT on the 40S head. Four of the five primary classes were sub-classified further. Resulting POST state ribosomes containing RQT were merged and sub-sorted using soft masks around the 40S head region, yielding two classes with highly enriched RQT density. These classes were merged and refined followed by local refinement for RQT after signal subtraction, yielding in a final resolution of 2.5 Å for the 80S (representing the C1 state) and 3.5 Å for the RQT complex. The RQT-containing 80S in the C2 state was obtained from the weak tRNA class, that contained idle ribosomes with only traces of tRNA which could be separated into RQT-containing particles in both C1 and C2 states. The C2 state particles were refined followed by local refinement of the RQT complex yielding in a final resolution of 3.0 Å for the 80S (representing the C2 state) and 5.0 Å for the RQT complex. Notably, despite some classes showing density for a neighboring ribosome, no stable disomes with RQT could be reconstructed from this dataset.

For the final sorted maps of RQT-ribosome complexes in state C1 (Figure 12A), local resolution of the ribosome ranged from ca. 2.4 Å at the core region, to 5.5 Å for more flexible areas, while the RQT complex was resolved at ca. 3.5-7.5 Å. In state C2 (Figure 12B), the ribosomal core region was resolved to ca. 3 Å, ranging up to 6.5 Å for the more flexible areas, with RQT in a resolution range from ca 5 -12 Å.

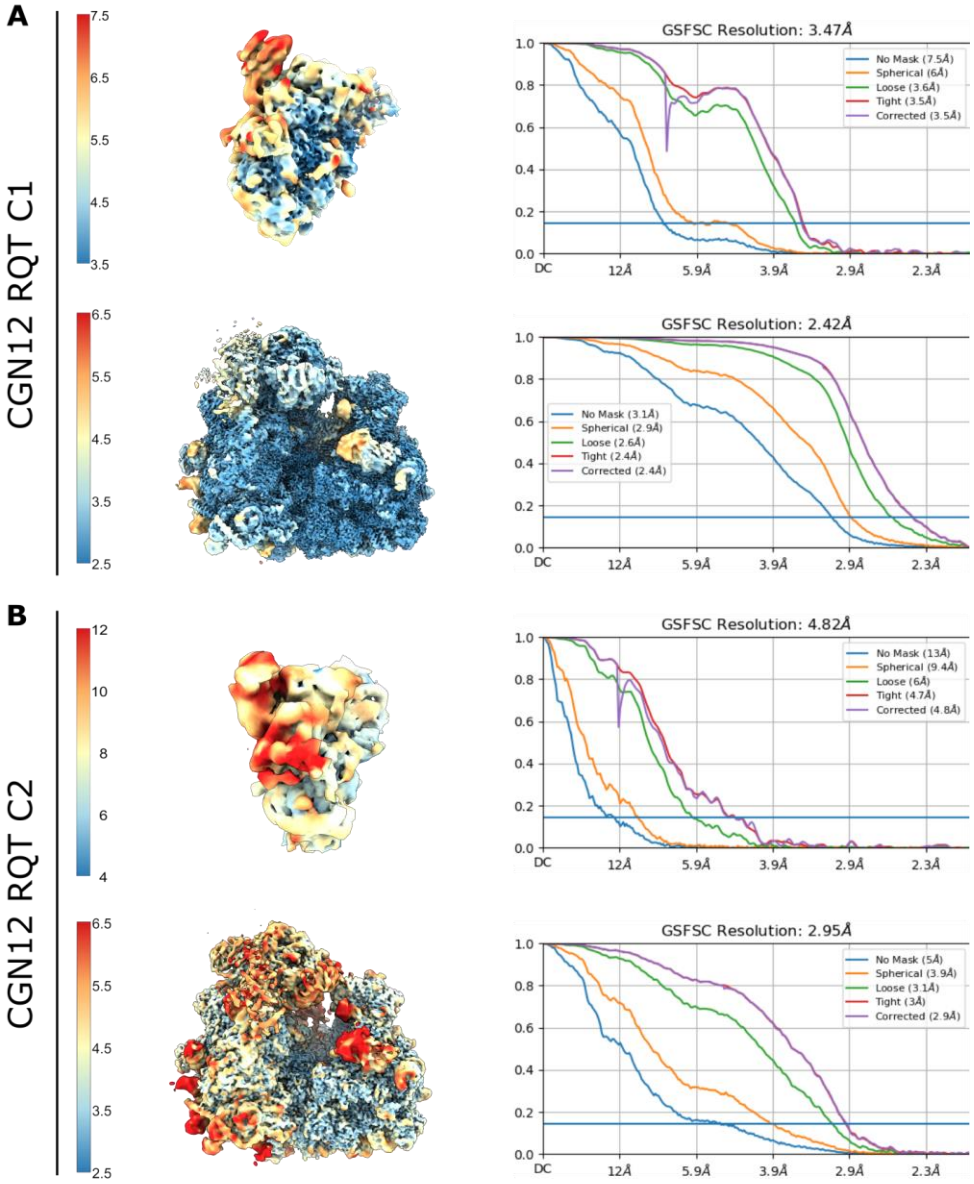

Figure 12: Local resolution of RQT-ribosome complexes.

(A) State C1, (B) state C2. Locally refined maps of the RQT complex or ribosome are colored according to the estimated local resolution. The corresponding FSC curves are shown on the right. The resolutions are estimated from the gold-standard FSC at 0.143.

The other datasets were processed in a similar way (for details see sorting schemes in the Appendix), all resulting in the identification of RQT-ribosome complexes (Figure 13).

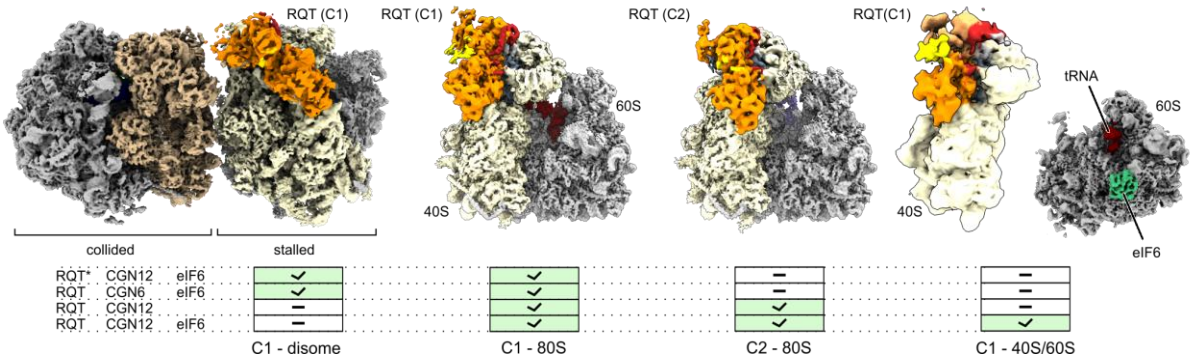

Figure 13: Overview of the observed RQT-ribosome complexes.

Composite maps of RQT-ribosome complexes are shown for the different samples. Grey: 60S subunit, light yellow/brown: 40S subunit, orange/yellow/red: RQT complex. For splitting competent reactions, RQT was observed in two states, C1 and C2, on the ribosome. In case eIF6 was included, subunits corresponding to splitting products (40S with bound RQT and 60S with eIF6 and peptidyl-tRNA) were observed. Reactions that did previously not show any splitting capacity (CGN6 mRNA or ATPase deficient RQT) resulted in stable RQT-disome complexes as well as 80S with RQT bound in C1, but not in C2 or splitting products.

When comparing the four collected datasets, various RQT-ribosome complexes could be identified. Similar to what was observed in the polysome profiles before, samples of splitting reactions with wild-type RQT and CGN_{12} disomes performed in the presence of anti-association factor eIF6, contained ribosomal subunits in addition to the observed RQT-ribosome complexes in state C1 and C2. Here, ca. 8 % of the identified 40S subunits also displayed extra density for the RQT complex. Almost all of the identified 60S subunits were bound to eIF6, with 8 % additionally containing peptidyl-tRNA, verifying that splitting did occur. Although during sorting some ribosomes still showed density for a neighboring ribosome, no stable RQT-disome complexes were obtained. Those were uniquely observed in the samples that did previously not show any splitting capacity. Although eIF6 was included during the reconstitution, both lack of an accessible 3' mRNA (of the CGN_6 stalled disomes) and the utilization of ATPase deficient RQT, did not result in visible subunits, or RQT-ribosome complexes in state C2. Instead, RQT was observed on the stalled (or lead) ribosome in state C1, with the colliding ribosome in a rotated PRE state. Similar to the splitting-competent samples, those datasets also contained RQT-80S complexes in state C1. The presence of 80S ribosomes in such disome samples is very likely a result of unspecific nuclease activity during substrate preparation.

Structure of the complex

Due to the high resolution, the wild-type RQT CGN_{12} dataset was used for model building. Local refinement of the isolated RQT densities allowed rigid-body fitting of (partial) alphafold models of Slh1, Cue and Rqt4 into the obtained maps (Figure 14).

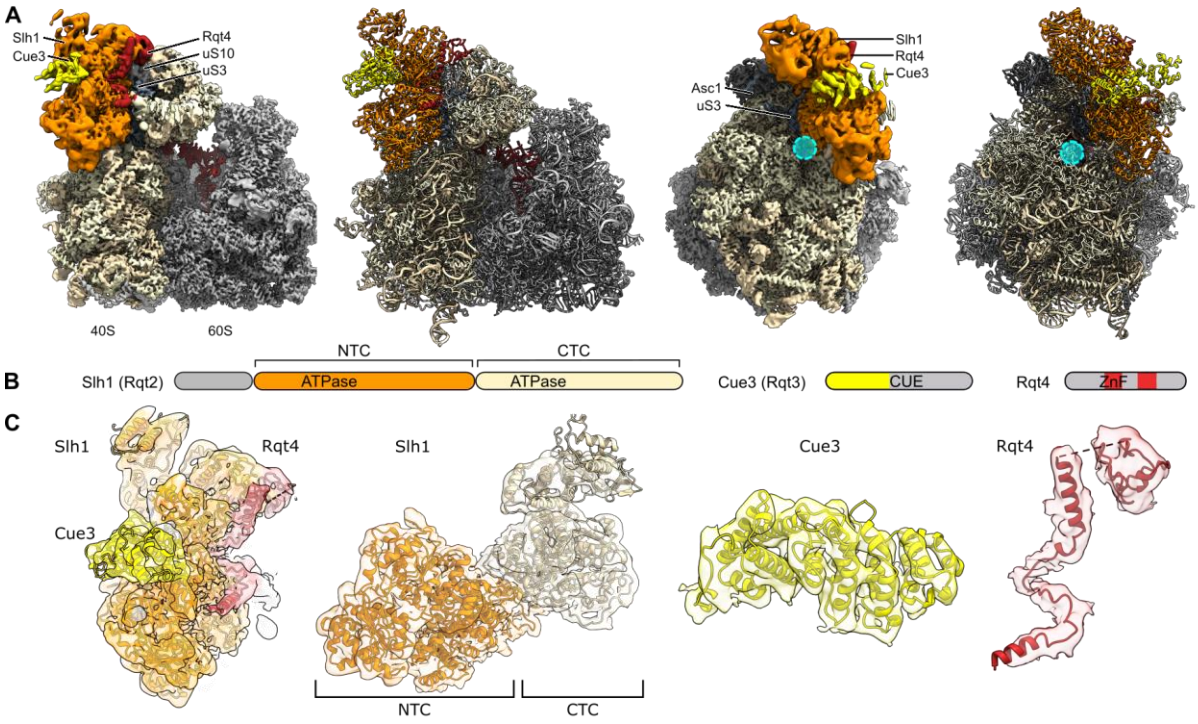

Figure 14: Cryo-EM structure of the RQT-ribosome complex.

(A) Top and side-view of the RQT complex on the ribosome. The local resolution filtered, composite EM-map and corresponding molecular model are shown. Dark orange: Slh1, gold: Cue3, red: Rqt4, light yellow: 40S subunit, grey: 60S subunit. RQT binds on the 40S subunit in between head and body in close proximity the mRNA entry (cyan circle), uS10, Asc1 and uS3. (B) Overview of RQT domains visible in the EM-map. (C) Alphafold2 models fit into the local filtered density for Slh1, Cue3 and Rqt4.

Overall, the RQT complex is located on the small ribosomal subunit in close proximity to the mRNA entry tunnel as well as ribosomal proteins Asc1, uS3 and uS10, where it bridges head and body of the 40S. For the large helicase component Slh1, only the N-terminus (1-217) is invisible in the EM-maps, enabling independent docking of both the N-terminal (NTC) and C-terminal helicase cassette (CTC). The density in between the two cassettes of Slh1, could be assigned to the N-terminal helical domain of Cue3 (1-297). In previous crystal structures of the human homolog of Cue3, ASCC2, this region was shown to interact with the N-terminus of the human Slh1 homolog, ASCC3 (invisible part of Slh1). The remaining part of Cue3, including the CUE domain which was proposed to be responsible for ubiquitin recognition and binding remains invisible. On the other side of Slh1, the C2HC5-type zinc-finger domain of Rqt4 (172 – 218) could be identified in between the Slh1-CTC and ribosomal protein uS10. Additionally, a helical part of Rqt4 (318 – 383) bridges CTC and NTC of Slh1. In all obtained structures, the mRNA itself was not visible outside of the ribosomal mRNA tunnel.

Interactions with the ribosome

In all the observed RQT-ribosome complexes, only Slh1 directly interacts with the ribosome. The domain arrangement of Slh1 closely resembles the one of the related Brr2 and Ski2 helicases. The NTC and CTC both consist of a RecA1-RecA2 ATPase site, connected to a Sec63 domain via a winged helix (WH) domain. The Sec 63 domain can be sub-divided into a Ratchet-, Helix-hairpin-Helix- (HhH) and Fibronectin-like- (FN3) domain (Figure 15A). Slh1 is anchored to the ribosome mainly via interactions of its NTC with ribosomal protein uS3 and rRNA helix 16, with one additional interaction formed between Asc1 and the CTC (Figure 15B).

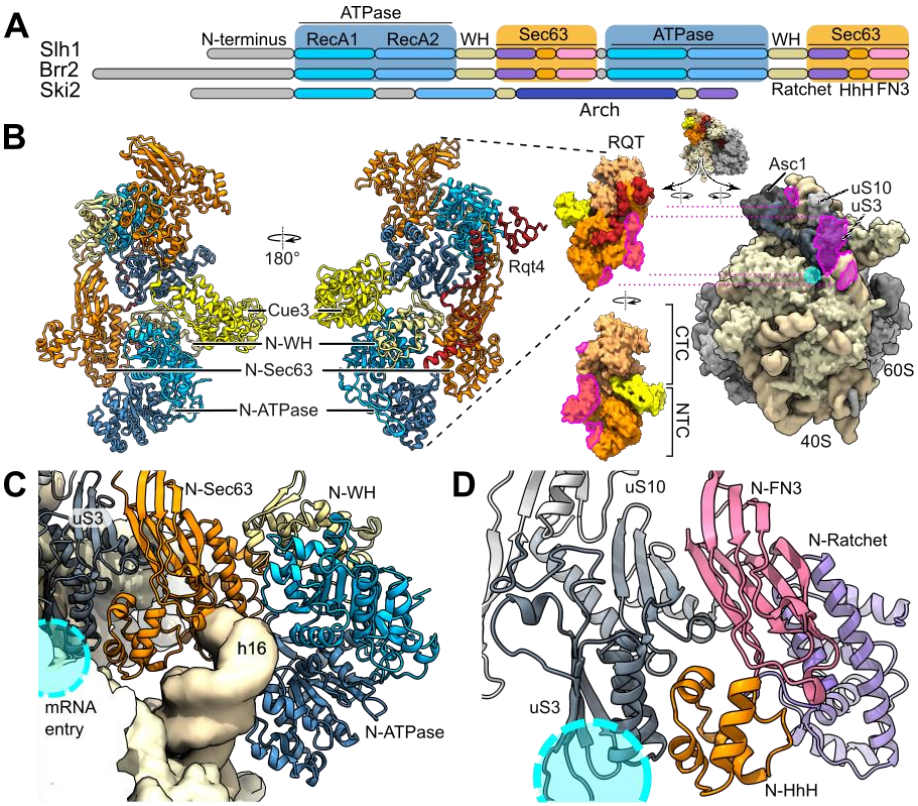

Figure 15: Molecular model of the RQT complex.

(A)Domain overview of Slh1, compared to homologous proteins Brr2 and Ski2. (B) Left: Molecular model of the RQT complex, right: Low-pass filtered map of RQT and ribosome, interaction interfaces are colored in pink. (C) Position of the N-terminal cassette on the 40S. (D) Interaction of the N-terminal FN3 and HhH-domains with ribosomal protein uS3.

On the ribosome, the NTC is wrapped around helix 16, with the Sec63 domain bound in close proximity to the mRNA entry on one side of the helix and the RecA1-RecA2 ATPase domains located on the opposite side (Figure 15C). The main interaction of the Sec63 domain with ribosomal protein uS3 has two contributions: one is formed by the FN3 sub-domain, where the terminal β-sheet of FN3 packs against the β-sheet of the uS3 KH domain (Figure 15D);

the other hails from the HhH sub-domain, which interacts with two alpha helices of the uS3 middle domain. In our structures, the CTC is located on top of the NTC and contacts ribosomal protein Asc1.

Interactions between RQT components

As described above, the N-terminal domain of Cue3 is bound in between the two Slh1 cassettes. In detail, it contacts the WH domain of the NTC (N-WH) and the RecA2 domain of the CTC (C-RecA2, Figure 16A). On the opposite side of Slh1, the zinc-finger (ZnF) domain of Rqt4 is bound on top of the C-RecA1 domain, close to ribosomal protein uS10. The remaining visible part of Rqt4 spans the two cassettes of Slh1, mainly by interactions with C-RecA2, and an interface between N-Ratchet, N-RecA2 and N-WH (Figure 16B).

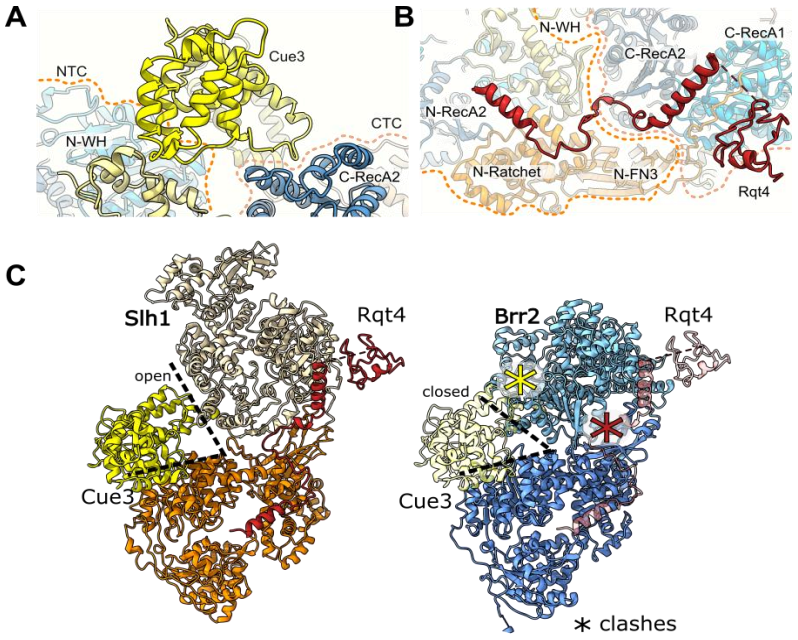

Figure 16: Detailed view of interactions between RQT components.

(A) Location of Cue3 in between the CTC and NTC of Slh1. Cue3 contacts C-RecA2 and N-WH (B) Location of Rqt4 on Slh1. The Znf domain of Rqt4 is bound on top of C-RecA1, the remaining visible part spans the two cassettes of Slh1 and interacts with C-RecA2, N-FN3, N-Ratchet and N-RecA2. (C) Comparison of the structures of Slh1 and Brr2. Slh1 adopts an elongated, 'open' conformation with Cue3 bound in between the two cassettes. Both Cue3 and Rqt4 clash with parts of Brr2 since it adopts a more compact 'closed' conformation.

Overall, these interactions stabilize an elongated Slh1 conformation, appearing more open compared to the crystal structure of the homologous protein Brr2 (Figure 16C, left). This limits the observed inter-cassette interactions of Slh1 to only one interaction of the C-RecA2 with the N-FN3 and N-WH. Although the overall domain arrangement and shape of Slh1 and Brr2 are almost identical, an overlay of the two co-factors Cue3 and Rqt4 with the Brr2 crystal structure reveals clashes due to the more compact cassette arrangement of Brr2 (Figure 16C, right).

Conformational Changes Induced by the RQT complex

For datasets collected of splitting-competent RQT samples (containing active RQT and an accessible 3' mRNA overhang), the identified RQT-ribosome complexes were observed in two distinct states. While the first state C1 represents a classic POST state ribosome with a P/P tRNA, in the second observed state C2, the head of the 40S is swiveled by ca. 20 degrees, with the beak of the 40S moving closer to the inter-subunit space. In contrast, the 40S body remains in a position comparable to the one observed in the C1 POST state (Figure 17).

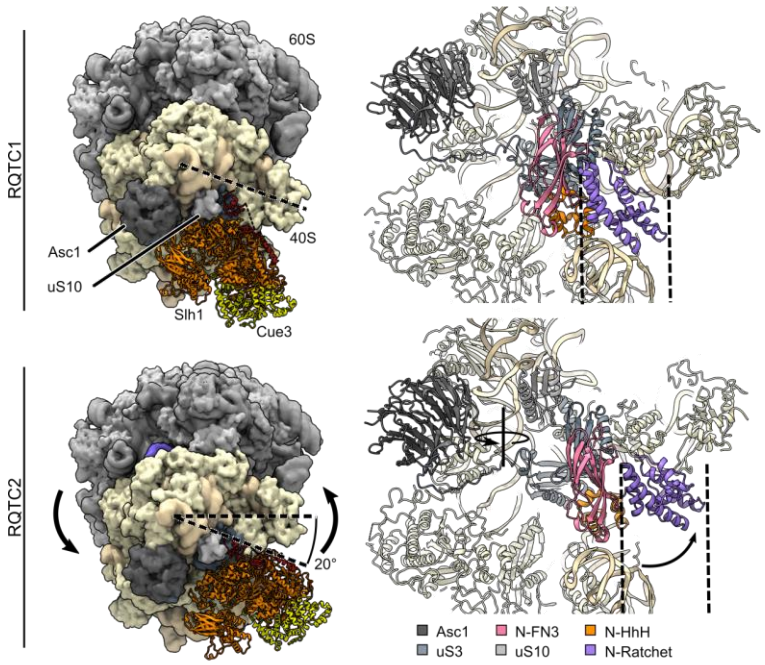

Figure 17: Comparison of the two observed RQT-bound ribosome states C1 and C2.

Top left: Local resolution filtered map of the RQT-bound ribosome in C1, with RQT displayed as a model. Top right: Model of the head region, the sub-domains of the Slh1-Sec63 domain which are acting as the main anchor of the RQT complex on the ribosome are colored in pink (N-FN3), orange (N-HhH) and purple (N-Ratchet), while ribosomal proteins Asc1, uS3 and uS10 are colored in shades of gray. Bottom left: Local resolution filtered map of the RQT-bound ribosome in C2. Bottom right: Model of the head region in C2, the head of the ribosome and the Sec63 domain of the RQT complex perform the same movement, leaving the interactions between uS3 and N-FN3 unaffected.

This movement of the ribosome matches the observed rearrangement of the RQT complex, which translocates on rRNA helix 16 (located on the 40S body), while the interactions of the Sec-63 sub-domains with ribosomal protein uS3 (located on the 40S head) remain unaffected, thus mirroring the movement of the 40S head. Additionally, the interaction between the N-HhH domain of Slh1, which contacts ribosomal protein eS30 (also located on the 40S body) in state C1 (Figure 18A), changes, such that the N-HhH domain now directly contacts rRNA helix 18, while the C-terminal tail of eS30 is displaced (Figure 18B).

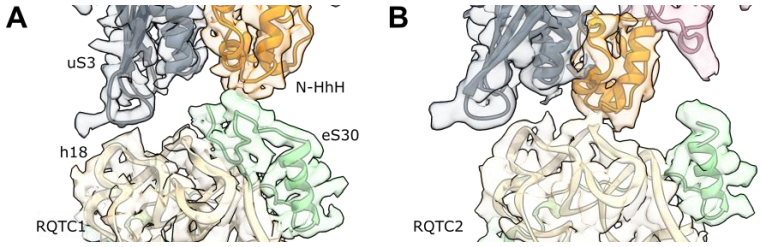

Figure 18: Interactions of the N-HhH domain with the ribosome in state C1 and C2.
(A) In state C1, the N-HhH domain of Slh1 interacts with uS3 and the C-terminus of ribosomal protein eS30 which in turn interacts with ribosomal rRNA helix 18 (h18). (B) In state C2, the N-HhH domain still interacts with uS3, but now directly contacts h18, while the C-terminus of eS30 is displaced.

In the observed state C2, the present tRNA adopts a chimeric pe/E state (Figure 19). This state is characterized by interactions of the tRNA with U1191 (human U1248) and G904 (human G961) of the 18S ribosomal rRNA. In the mammalian system, a similar state has been described as a late translocation intermediate (TI-POST-2), only observed with bound eEF2 and a non-hydrolysable GMP-PNP, which prevents the ribosome from transitioning to the POST state (Figure 19, (Flis *et al.*, 2018)). However, in the described TI-POST-2 state, two tRNAs were observed in ap/P and pe/E positions, respectively. Interestingly, while eEF2 contacts both 40S and 60S subunit of the ribosome, in our observed structure, Slh1 only interacts with the small ribosomal subunit.

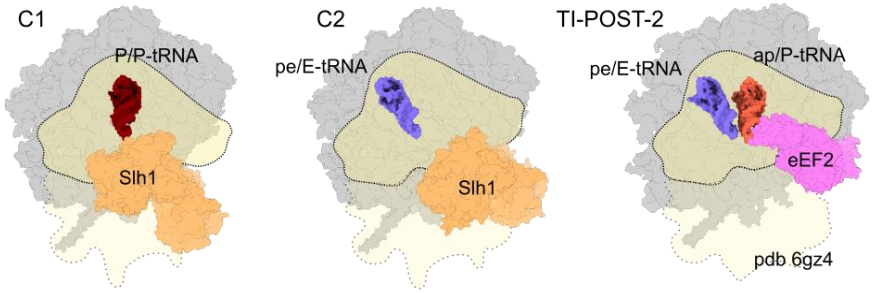

Figure 19: Comparions of RQT-bound ribosome states C1 and C2 to the mammalian TI-POST-2 state.
In state C1, the ribosome is in a non-rotated POST state with a tRNA in a P/P-state, while in state C2, the head of the 40S is swiveled and the tRNA adopts a chimeric pe/E-state. The C2 state is similar to a late translocation intermediate usually observed in the presence of eEF2 and non hydrolyzable GMP-PNP, however here usually two tRNAs are accomodated.

State C2 was only observed in splitting competent samples, suggesting its requirement for the splitting reaction. However, RQT-80S complexes in state C2 were still present in the samples containing eIF6, indicating that the rearrangement on its own is not sufficient to efficiently dissociate ribosomes. This supports the earlier observations, which found a diminished splitting efficiency for ubiquitinated 80S compared to ubiquitinated di- and trisomes. To analyze what the conformational change implies for a disome, models of the RQT-bound ribosomes were compared. Structures of RQT bound to disomes could only be obtained from samples without accessible 3’ mRNA or lacking RQT ATPase activity. In these structures, RQT is bound to the lead ribosome, comparable to the RQT-80S C1 state.

On the colliding ribosome, the observed binding interface is not accessible, providing a structural explanation of observations made in previous studies, that found the lead ribosome as the target for RQT mediated dissociation (Juszkiewicz *et al.*, 2020b; Matsuo *et al.*, 2020).

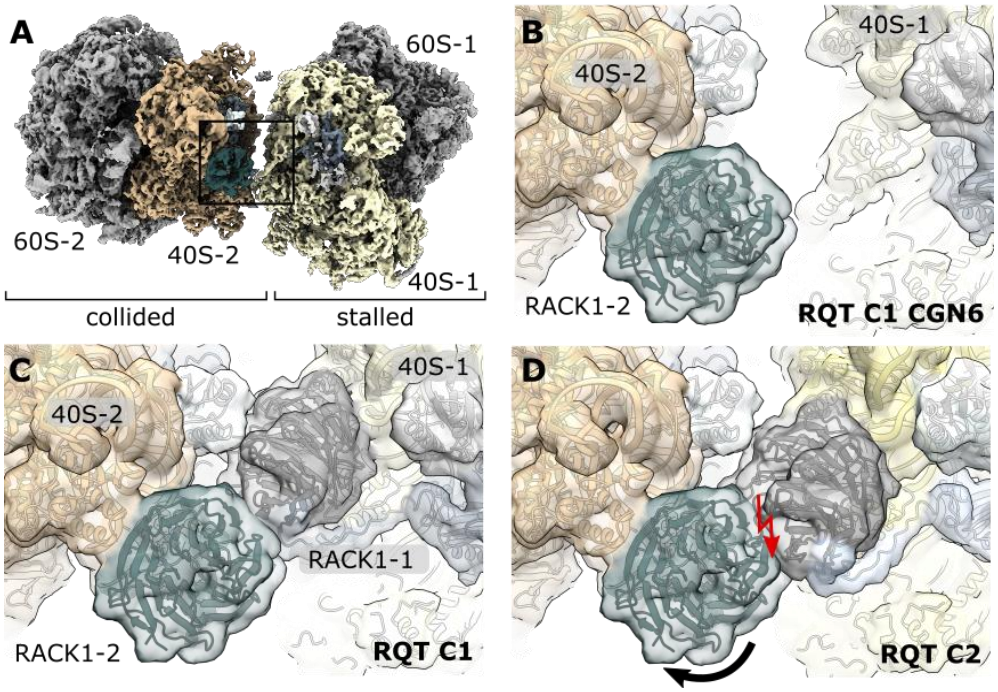

Figure 20: Implications of the observed C1 and C2 states for disomes.
(A) Composite map of CGN6 stalled disomes bound to RQT, the black box indicates the region of the zoom in (B). (B) Zoom view of the CGN6 stalled disome model. In the lead ribosome RACK1 is underrepresented. (C) Superposition of the collided CGN6 ribosome (40S-2) with the lead ribosome in state C1 (40S-1). (D) Superposition of the collided CGN6 ribosome with the lead ribosome in state C2. Here, the head swivel observed in state C2 leads to a clash between the RACK1 proteins.

An overlay of the RQT-ribosome complex in state C2 on the lead ribosome of the disome (Figure 20A, C, D) shows a clash in the tight RACK1-RACK1 interface: RACK1 in the swiveled C2 position overlaps with the RACK1 positioned on the colliding ribosome. Intriguingly, in the observed RQT-disome structure RACK1 is underrepresented: the tight RACK1-RACK1 interface commonly found in collided ribosomes seems to be already destabilized upon prolonged RQT binding (Figure 20B), although the samples did not show any splitting activity.

Contributions of the helicase cassettes

So far, conformational change and splitting was shown to be dependent on ATPase activity of the N-terminal helicase cassette of Slh1, an accessible mRNA overhang and the presence of a second, colliding ribosome. Due to the helicase activity of Slh1, it would be plausible that this is indeed the part of RQT that engages the mRNA. Compared to Brr2, where only the NTC was shown to be active, in Slh1, both cassettes exhibit the right residues for helicase activity (Figure 21).

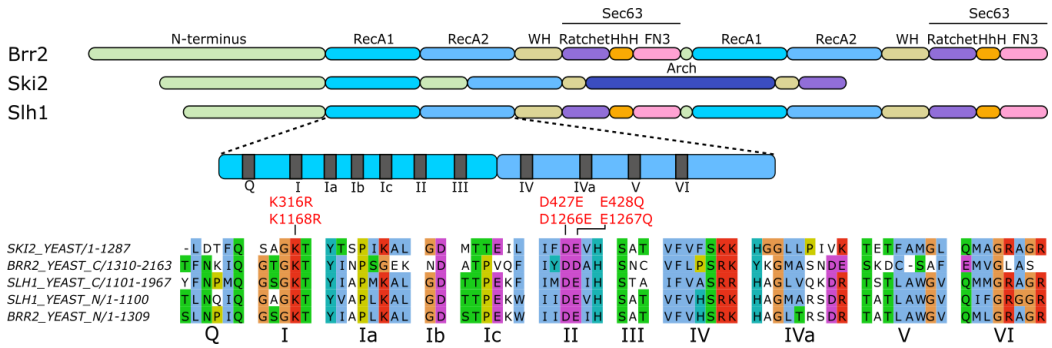

Figure 21: Domain architecture and alignment of Ski2 family helicases Brr2, Ski2 and Slh1.

Domain overview (top) and sequence alignments (bottom) of Slh1 with Brr2 and Ski2 from S. cerevisiae. The region of the (N-terminal) RecA domains is enlarged and conserved hallmark sequences for this protein family are indicated, for which also the sequence alignment is shown. Alignments are comparing the C- and N-terminal cassettes of both Slh1 and Brr2 with Ski2. The CTC of Brr2 in is inactive as indicated by low conservation; for the CTC of Slh1, however, all regions crucial for ATPase activity are conserved. Indicated in red are Walker A (motive I) and Walker B (motive II) mutations in the Slh1 N- and C-terminal cassettes, respectively.

In contrast to the obtained RQT-ribosome structures, where no mRNA is visible outside of the ribosomal mRNA tunnel, previous studies on Ski2 could follow the path of the mRNA into the helicase core ((Schmidt *et al.*, 2016b), Figure 22, left panel). Assuming the same 3' to 5' directionality attributed to all Ski2 family helicases, for Slh1, the mRNA exit of the NTC is blocked by h16 and the NTC is directionality wise bound in an unfavorable position to act on the mRNA emerging from the ribosomal entry site (Figure 22, RQT C1). In contrast, the CTC is positioned more similar to Ski2 and could in principle engage mRNA. Especially in state C2, the CTC moves closer towards the mRNA entry and would be positioned ideally to pull on the free 3' mRNA.

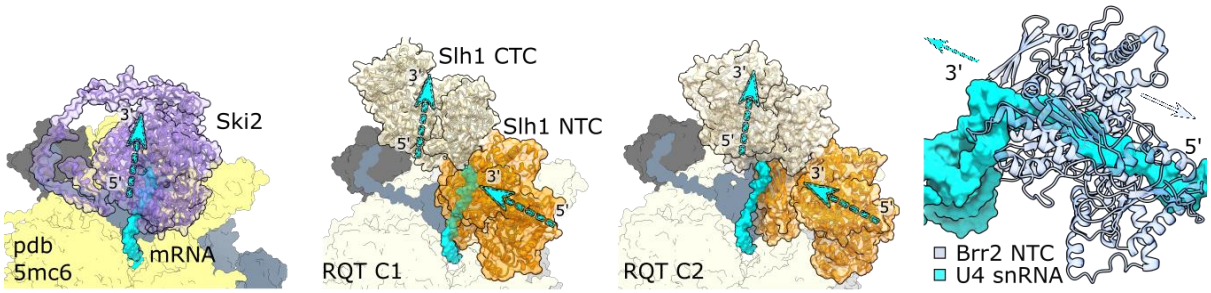

Figure 22: Directionality of Ski2 family helicases Brr2, Ski2 and Slh1.

Comparison of the directionality of Ski2 family helicases Ski2 (pdb 5mc6), Brr2 (pdb 5gan) and Slh1. All known Ski2 family helicases exhibit 3' to 5' helicase activity. Compared to Ski2, The CTC of Slh1 is in a more favorable position for helicase activity on the mRNA. For the NTC, the mRNA exit is blocked by helix 16 and the mRNA entry is on the opposite site of the mRNA entry channel of the ribosome.

To elucidate the role of the CTC in the splitting process, Slh1 mutants of the Walker A motif (K1168R), corresponding to the previously used K316R mutation of the NTC, as well as Slh1 mutants of the Walker B motif (D1266E or E428Q/E1267Q) were generated by Dr. Ken Ikeuchi (Figure 21). These mutants were co-purified with Cue3 and Rqt4 from yeast over-expression strains as described above for the wild-type. Successfully purified complexes were used in splitting assays with *in vitro* ubiquitinated CGN_{12} stalled ribosomes and analyzed by sucrose density gradients (Figure 23).

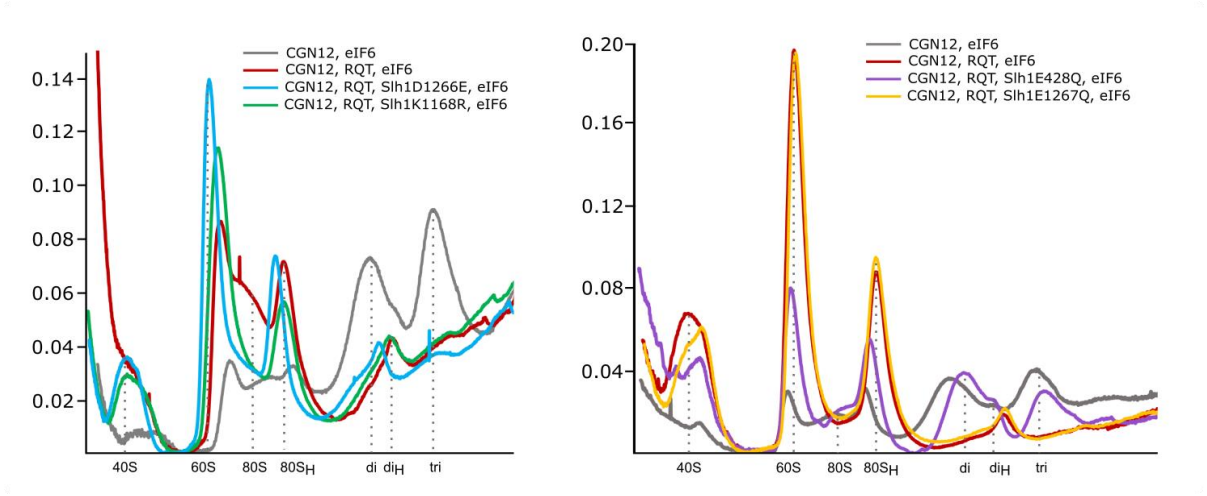

Figure 23: Dependency of the splitting reaction on ATPase activity of CTC and NTC.
For the assays, in vitro uniquitinated trisomes were incubated with RQT with several Slh1 mutations. (grey) control reaction without RQT, (red) control reaction with wt RQT. Mutations of the CTC of Slh1 (blue, green and orange) did not have any discernable influece on the splitting activity, while the Walker B mutation of the NTC (purple) showed a decrease in splitting efficiency.

As before, *in vitro* ubiquitinated di- and trisomes were successfully dissociated by incubation with wild-type RQT, resulting in a complete collapse of the corresponding peaks coupled to an increase in signal for the ribosomal subunits. Surprisingly, of the newly prepared mutants, only the Walker B NTC mutant (Slh1 E428Q) did not lead to efficient splitting, similar to what was previously observed for the NTC Walker A mutant (Slh1 K316R Figure 7C). Both Walker A (K1168R) and Walker B mutants (D1266E, E1267Q) of the CTC ATPase site were still splitting competent.

Recapitulating the findings so far, the *in vitro* splitting reaction of collided ribosomes by RQT could be optimized in order to obtain structural insights into the splitting process. RQT was observed to process ribosomes consecutively, in a mechanism dependent on ubiquitination of the collided ribosomes, presence of a neighboring ribosome and accessible 3' mRNA. Although RQT was directly interacting with the mRNA in cross-linking experiments, no density for mRNA was visible in the obtained RQT-ribosome structures, where RQT is stably bound to the small ribosomal subunit close to the mRNA entry.

Inhibition of frameshifting by Mbf1/EDF1

Mbf1 in yeast is a highly abundant protein (85,000 molecules/cell, (Kulak *et al*., 2014), 43,000-65,000 molecules/cell, (Ho *et al*., 2018)) that was recently proposed to inhibit frameshifting in the context of ribosomes stalled on inhibitory codon combinations (Wang *et al.*, 2018). By serendipity, the cryo-EM analysis of *SDD1* stalled RNCs, that were initially investigated in context of RQT mediated splitting (described above) revealed the structure of Mbf1 bound to the ribosome. In parallel to this finding, the human homolog, EDF1, was identified to be recruited to emetine-stalled ribosomes (Juszkiewicz *et al*., 2020a; Sinha *et al.*, 2020). To compare Mbf1 and EDF1, a structure of EDF1-ribosome complexes was solved after affinity-purification from cells expressing tagged EDF1.

SDD1 stalled ribosomes contain Mbf1

To obtain *SDD1*-stalled ribosomes, a mRNA construct encoding a His6-tag followed by a V5 tag and a TEV cleavage site as well as the stalling region of *SDD1* (101-218) was used in an *in vitro* translation system with cell free yeast extract (*Δski2, Δslh1, Δcue3*). Stalled ribosomes were affinity purified and collided ribosomes (trisomes) were isolated using sucrose density gradient centrifugation. Reconstitution of such ribosomes with RQT complex (described above) were analyzed by collecting data on a Krios Titan Microscope with a K2 Summit DED. From 4109 micrographs, 398,317 particles resembling ribosomes were selected after 2D classification (Figure 24). Although trisomes were collected from the gradient, the samples were processed as single 80S. 3D classification revealed most ribosomes (63 %) in a rotated PRE-state containing A/P and P/E tRNAs, 24 % in a non-rotated POST state containing P/P tRNA and 13 % in a non-rotated PRE-state with A-site tRNA, similar to the states previously observed for collided ribosomes (Ikeuchi *et al.*, 2019). Further classification of the PRE-state ribosomes revealed a class containing extra density between the 40S beak and rRNA helix 16 of the 40S body which could be identified as the HTH domain of Mbf1, since the HTH motive of archaeal Mbf1 had previously been described as binding to the small ribosomal subunit and its structure was solved by solution NMR (Blombach *et al.*, 2014). Intriguingly, Mbf1 was found only on rotated PRE-state ribosomes, since sub-sorting of the other classes with a focus on Mbf1 did not reveal any extra density.

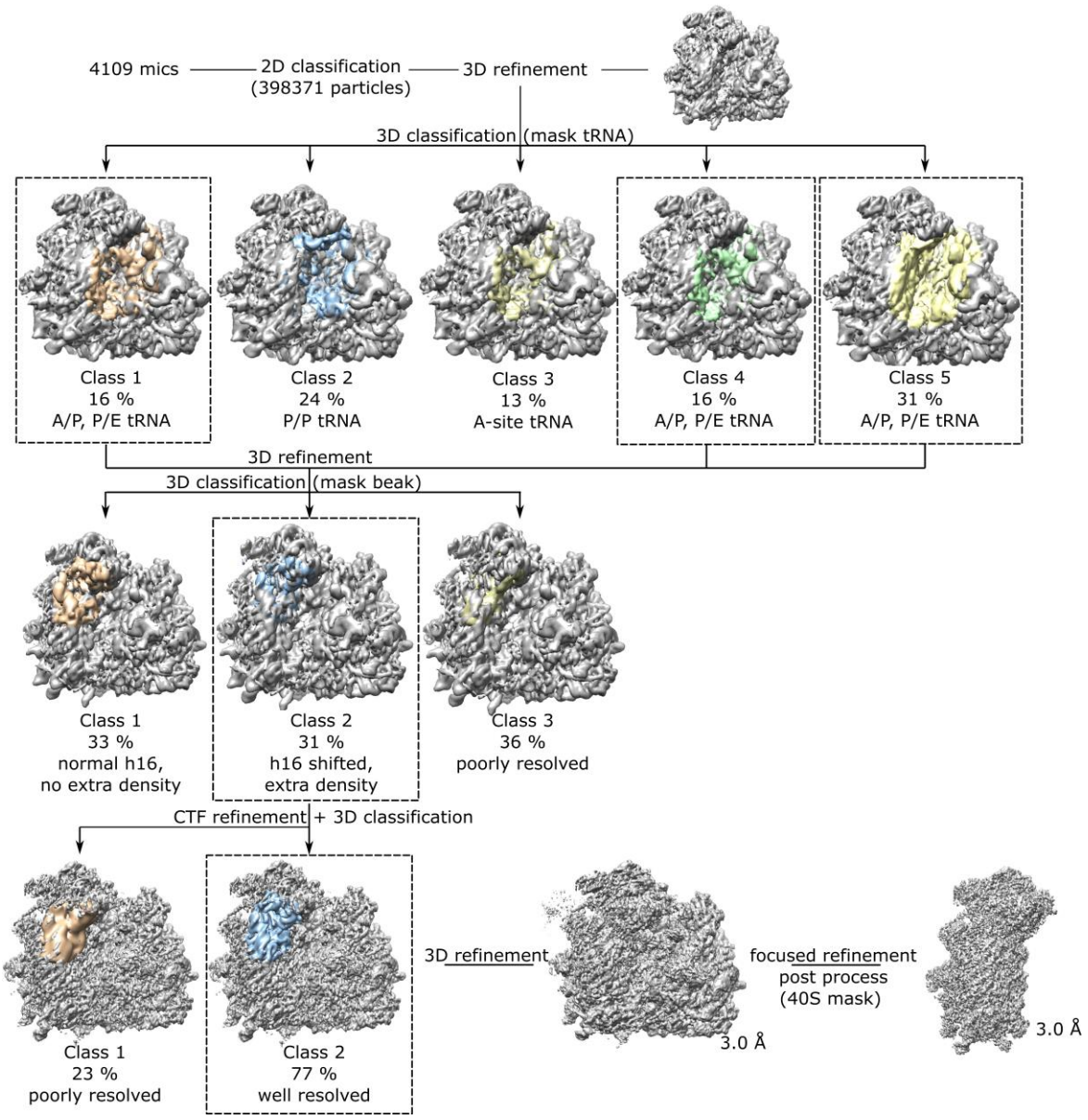

Figure 24: Sorting scheme for the cryoEM analysis of SDD1 stalled ribosomes.

From a total of 4109 micrographs, 398317 particles were selected after 2D classification. The obtained particles were processed using Relion 3.1. Refinement and 3D classification were performed, resulting in 5 classes with three distinct tRNA states.13 % of the ribosomes (non—rotated PRE) contained A/A-site tRNA, 24 % were observed in an non rotated POST-state (P/P tRNA). The remaining 63 % adopted a rotated PRE-state with tRNAs in a hybrid A/P, P/E state. Further sorting of the third state revealed a sub-class of ribosomes in which helix 16 was shifted towards the 40S subunit and that contained extra density in between beak and body of the 40S subunit. After focused refinement and post processing the overall resolution was determined at 3.0 Å, according to the GSFSC.

Purification of EDF1-ribosome complexes from human HEK cells

EDF1 was identified as a factor involved in quality control co-migrating with collided ribosomes (Juszkiewicz *et al.*, 2020a; Sinha *et al.*, 2020). This raised the question if EDF1 binds those ribosomes similar to what was observed for the yeast protein Mbf1. To answer this, HEK293 Flp-In T-Rex cells expressing EDF1 with an N-terminal 3xFLAG-tag and 3C Protease cleavage site were generated by Matthias Thoms. From those cells, EDF1-ribosome complexes were affinity purified by Timo Denk. The eluted complex was analyzed using SDS-PAGE (Figure 25).

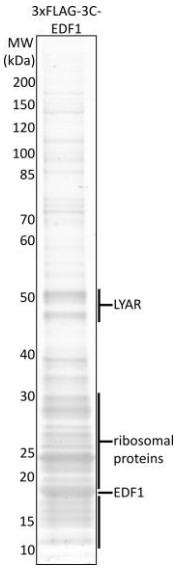

Figure 25: SDS-PAGE of the 3xFLAG-3C-EDF1 affinity purification.

In addition to the expected EDF1 band (ca. 17 kDa), the typical pattern of ribosomal proteins was observed, confirming the co-purification of EDF1 and ribosomes. Interestingly, a larger protein (ca. 50 kDa) was also enriched in the EDF1 elution fraction. Using mass spectrometry, this was identified as the cell growth-regulating nucleolar protein LYAR.

Structure of the EDF1-ribosome complex

To understand how EDF1 associates with ribosomes, the obtained complex was analyzed using cryo-EM. Samples of the elution fraction after affinity purification were flash-frozen on EM grids and data were collected on a Krios Titan Microscope with a K2 Summit DED. From 4,260 micrographs, 95,832 particles were selected after 2D classification (Figure 26). After 3D classification, 85 % of the ribosomes were found in a non-rotated state containing density for EDF1 and LYAR, while the rest resembled either poorly resolved 80S or 80S bound to elongation factor eEF2.

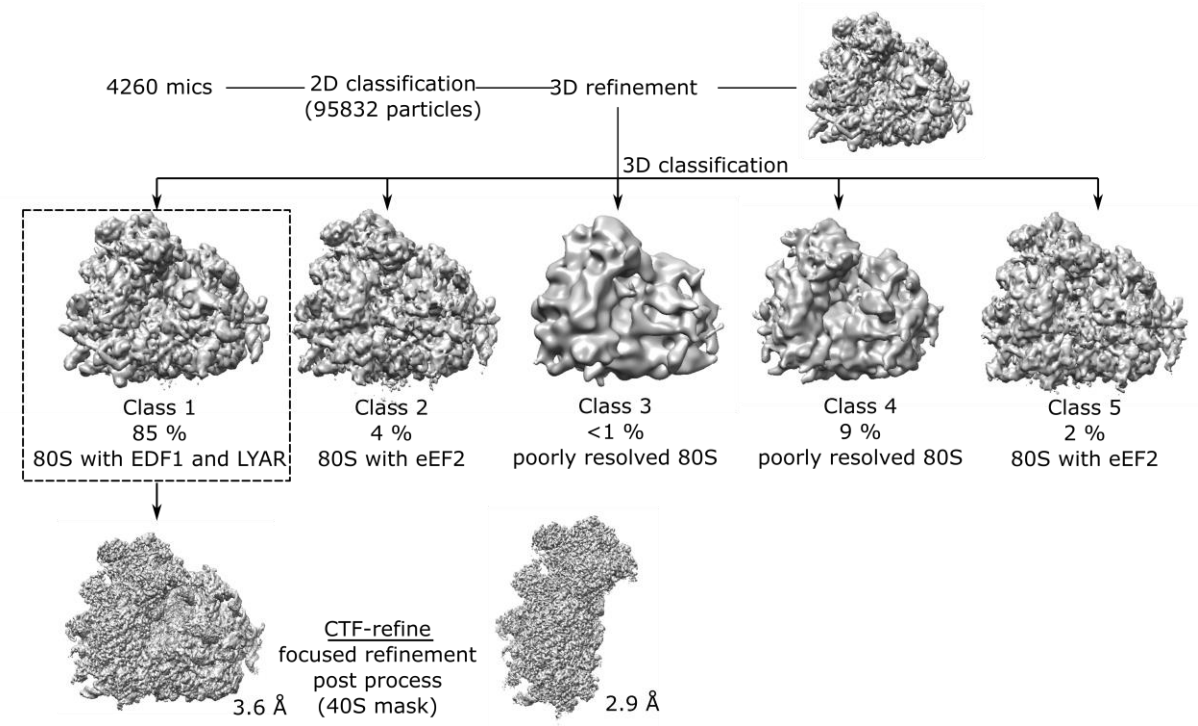

Figure 26: Sorting scheme for the cryoEM analysis of EDF1-bound ribosomes.

From a total of 4260 micrographs, 95832 particles were selected for 3D refinement and 3D classification. 3D classification resulted in 5 distinct classes with 85 % of the ribosomes showing extra density for EDF1 and LYAR. After post-processing, the overall resolution of the 40S from the EDF1-80S complex was determined at 2.9 Å, according to the GSFSC.

Comparison of ribosome bound EDF1 and Mbf1

After CTF-refinement, focused refinement and post processing, the Mbf1 and EDF1 bound ribosomes could be resolved at an average resolution of 3.0 Å and 2.9 Å, respectively (according to the gold standard criterion, Figure 27). For the Mbf1-ribosome, the observed local resolution ranged from 2.9 Å in the core region to 6.0 Å for the more flexible parts of the ribosome. The EDF1 bound ribosome was slightly better resolved with 2.5 Å for the ribosomal core and ca. 6.0 Å for the auxiliary regions.

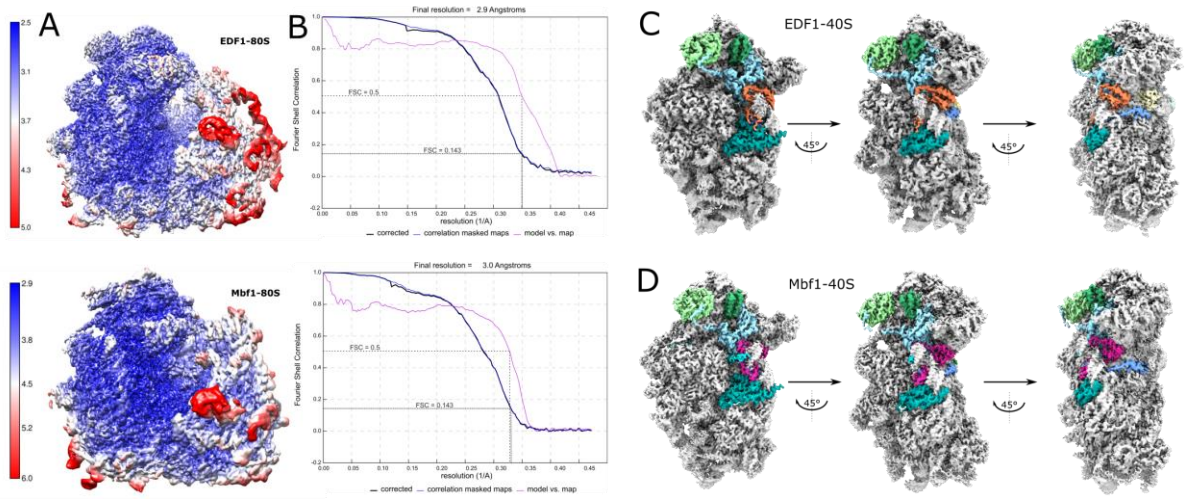

Figure 27: Validation of the final EM maps.

(A) Final filtered EM maps, (top) EDF1-bound 80S, (bottom) Mbf1 bound 80S colored according to local resolution. (B) Fourier shell correlation (FSC) curves corresponding to the final maps shown in (A). FSC curves of the final cryo-EM density maps (black), indicating average resolutions (FSC = 0.143, dashed black line), and FSC curves calculated between the cryo-EM density map and the final model (purple) as calculated by Relion. (C,D) Cryo EM map of the EDF1/Mbf1 bound ribosome, important ribosomal proteins are colored in shades of green/blue (light green: RACK1/Asc1, dark green: uS10, light blue: uS3, blue: eS30 and teal: uS4) EDF1 and Mbf1 are colored in orange or pink, respectively.

The Mbf1-bound ribosome displayed a rotated PRE-state with hybrid A/P and P/E-tRNAs and traceable mRNA. In contrast to that, the EDF1-bound ribosomes adopted a non-rotated conformation, without tRNAs in the intersubunit space. Here, the mRNA is invisible. Instead LYAR is bound to the 40S A-site. This is similar to a previously observed structure of ribosome bound viral protein Nps1, in which LYAR was identified in the same position (Thoms *et al.*, 2020). In both the Mbf1 and EDF1 structure, the extra density for EDF1/Mbf1 is located between the beak of the 40S head and rRNA helix 16 (h16) of the 40S body (Figure 27C, 27D, 28). For both proteins, the obtained maps could be used to build a near complete molecular model (EDF1:24-133, Mbf1: 27-137), covering both the N-terminal Mbf1-domain (containing α1 and α2 helix), and the C-terminal helix-turn helix domain (α3- α6).

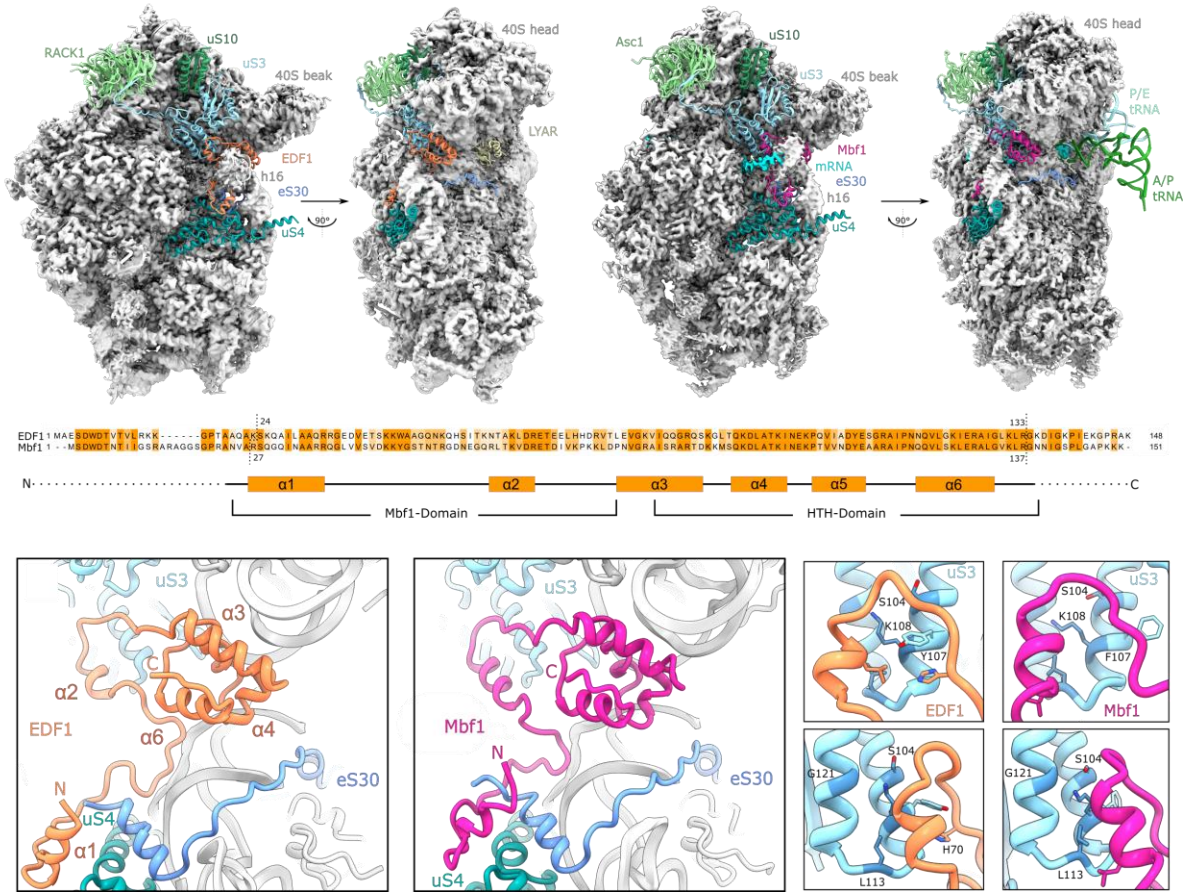

Figure 28: Structure of EDF1/Mbf1 bound to the ribosome.

(Top, left), EDF1 (orange) binds to the ribosome between beak and helix 16 of the 40S ribosomal subunit. Important ribosomal proteins are colored in shades of green/blue (light green: RACK1/Asc1, dark green: uS10, light blue: uS3, blue: eS30 and teal: uS4). (Top, right) Mbf1 binds to the ribosome in a mode identical to the EDF1 structure. In addition to important ribosomal proteins, the mRNA is colored in cyan and hybrid A/P,P/E tRNAs are displayed. (Middle) Alignment of the conserved EDF1 and Mbf1 proteins. For EDF1 residues 24-133 could be modeled, wheras for Mbf1 residues 27-137 were modeled. The modeled region covers 6 α-helices (termed α1- α6) and contains the N-terminal Mbf1-Domain and the C-terminal Helix-turn-Helix (HTH) domain. (Bottom, left) Detailed view of the EDF1 model. The EDF1 HTH-Domain is sandwiched between helix 33 and helix 16 of the ribosomal 18S rRNA. The loop connecting α2 and α3 as well as α2 itself interact with the middle domain of uS3. Helix α1 interacts with helix 16, opposite from the HTH-Domain and ribosomal protein uS4. (Bottom, middle) Mbf1 shows the same mode of binding and interactions as EDF1. (Bottom, right) Detailed view of the interaction of EDF1/Mbf1 and ribosomal protein uS3. Indicated in dark blue are conserved residues involved in frameshifting inhibition.

EDF1 and Mbf1 are highly conserved and bind the ribosome in close proximity to the mRNA entry in an identical fashion. The C-terminal HTH-Domain is sandwiched between h33 (40S beak) and h16 (40S body) of the 18S ribosomal RNA. From the HTH-Domain, the path of EDF1/Mbf1 could be traced to the mRNA entry channel, where the α2 helix of the Mbf1-domain interacts with two α-helices of the uS3 middle domain. Mutations of conserved uS3 residues in this region were previously shown to increase frameshifting on inhibitory CGA codons (Wang *et al.*, 2018).

From the mRNA entry, EDF1/Mbf1 continues down to the base of h16, where the N-terminal α1 helix of the Mbf1-domain interacts with ribosomal proteins uS4 and eS30 (Figure 29A, 29B).

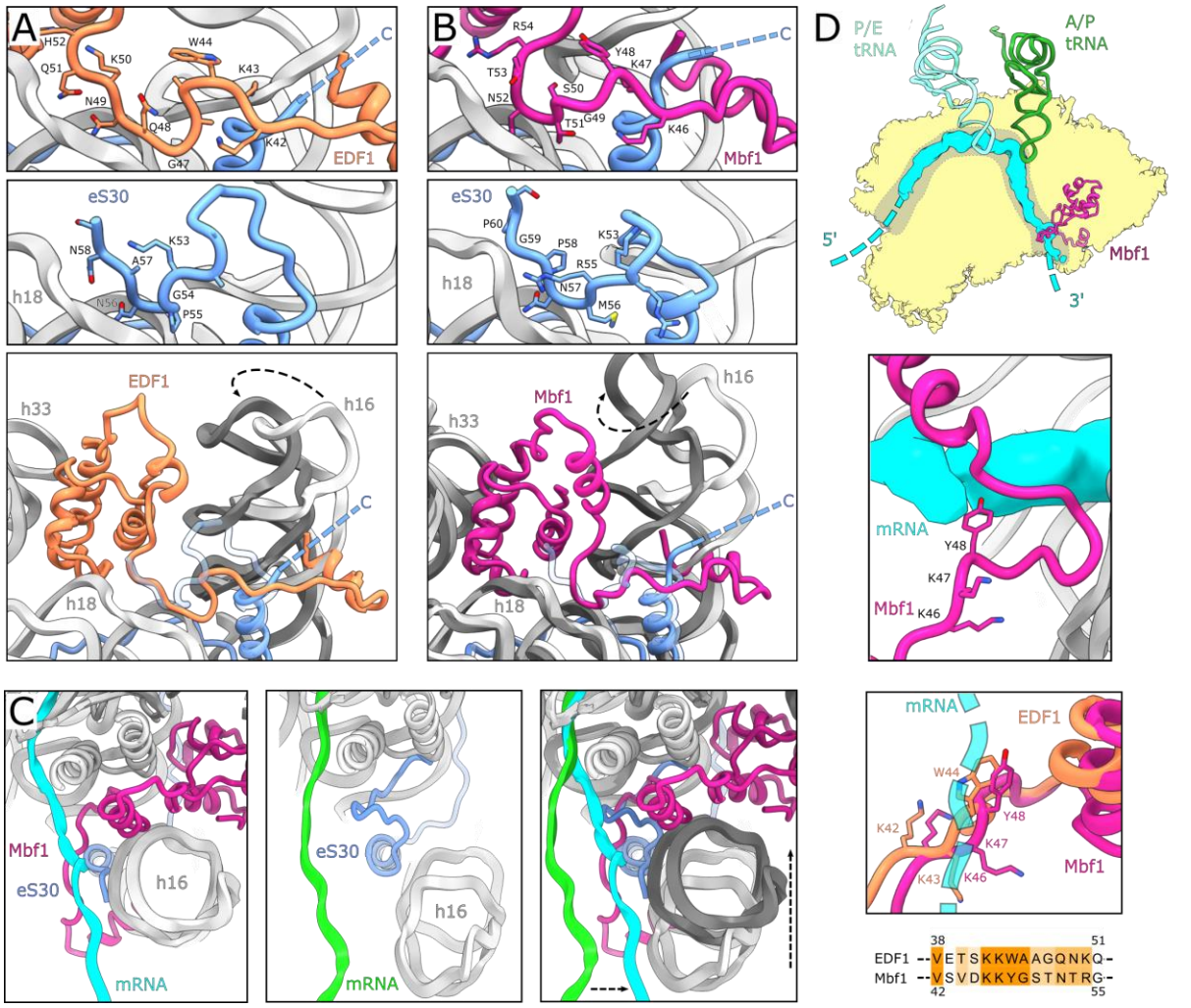

Figure 29: Conformational changes in the EDF1/Mbf1 bound ribosomes.

(A,B) MBF1/EDF1 displace the eS30 C-terminus from rRNA helix 18. (Top) Structure of EDF1/Mbf1 interacting with rRNA helix 18, K47 (Mbf1) and K43 (EDF1) respectively reach toward the backbone of helix 16 and thereby displace the C-terminus of eS30. The interaction with h18 is similar to the one observed for the eS30 C-terminus (middlie panel). (Bottom) In the EDF1/Mbf1 bound structures helix 16 is displaced towards the 40S, a position that would additionally clash with the usual position of the eS30 loop. (C) Comparison of the Mbf1 bound ribosome to a cannonical colided ribosome (pdb 6i7o, middle pannel). The most distinct changes are the displacement of h16 as well as a shift in the mRNA position towards h16 and Mbf1. (D) In the Mbf1-ribosome structure, the mRNA can be traced through the ribosome, from the E-site to the mRNA entry channel. Near the mRNA entry, Mbf1 forms a headlock-like arrangement comprised of its α2 helix and the following upstream KKY motif (KKW in human). While the mRNA was invisible for the EDF1-bound ribosome, this motiv is positioned in a similar way.

Between α1 and α2, residues of both Mbf1 and EDF1 interact with h18, thereby displacing the C-terminus of ribosomal protein eS30 which is usually observed in this location. Additionally, in the observed structure, lysine 43 (K43) of EDF1 (K47 in Mbf1) points towards h16, and is thus located on top of a helix of eS30 (30-42), preventing accommodation of the following loop and C-terminus.

Compared to the previously described structure of a collided ribosome, the interaction of EDF1/Mbf1 with the ribosome leads to a conformational change of h16, which is shifted closer to the ribosome (Figure 29C). In the Mbf1 structure, the path of the mRNA could be traced though the ribosome, from the E-site to the mRNA entry channel (Figure 29D). Here, the path of the mRNA is also shifted closer to helix 16 and Mbf1. Mbf1 itself forms a head-lock like clamp around the emerging mRNA 3' end, consisting of a conserved KKY (46-48, EDF1: KKW 42-44) motif positioned to interact with the mRNA, followed by the α2 helix of the Mbf1-domain.

Overall, Mbf1 is stably bound to SDD1 stalled colliding ribosomes and positioned ideally to stabilize the mRNA. While the EDF1 bound structure did not contain visible mRNA or tRNAs and thus most likely resembles a translationally inactive state, comparison with the translationally active Mbf1 ribosome showed a conserved mode of binding, suggesting that EDF1 could stabilize mRNA in a similar fashion.

Discussion

Ribosomal collisions are a conserved hub for quality control

Monitoring the translation process is crucial to ensure protein and mRNA homeostasis. In case something goes wrong, cells need to deal with the situation to mitigate detrimental effects such as proteotoxicity. In recent years, formation of collided ribosomes has emerged as a proxy for faults during translation and turned out to be a key trigger for quality control pathways. By formation of a unique collision interface, such ribosomes can be easily distinguished from ribosomes undergoing regulatory pauses and targeted accordingly.

At this point a variety of pathways recognizing collided ribosomes have been discovered. Depending on the conditions leading to collision, different factors are recruited, leading to various outcomes. One example is the induction of the Gcn2 dependent integrated stress response upon amino-acid starvation. Gcn1 and Gcn20 were found to bind the collided ribosome, most likely enabling binding of Gcn2, leading in turn to phosphorylation of eIF2α and thus prevention of further translation initiation (Pochopien *et al.*, 2021). A different mechanism targets ribosomes stalled on faulty mRNAs: Here, collisions lead to ubiquitination of the involved ribosomes and are subsequently resolved by RQT/RQC (Hashimoto *et al.*, 2020; Ikeuchi *et al.*, 2019; Juszkiewicz *et al.*, 2018; Juszkiewicz *et al.*, 2020b; Matsuo *et al.*, 2017; Matsuo *et al.*, 2020; Simms *et al.*, 2017; Sitron *et al.*, 2017; Sundaramoorthy *et al.*, 2017). In genetic screens, ribosome binding proteins Rbg1 and Rbg2 were necessary for efficient growth of cells lacking RQT component Slh1 (Daugeron *et al.*, 2011). Rbg1 and Rbg2 were recently found to be recruited to ribosomes translating lysine- or arginine-rich regions, promoting efficient translation and thereby preventing collisions (Zeng *et al.*, 2021). Rbg2 was also identified on collided ribosomes together with Gcn1, and eIF5A, probably enhancing peptide bond formation to enable resumption of translation (Pochopien *et al.*, 2021). If collisions persist, endonuclease Cue2 (NONU-1 in *C. elegans*) can cut the mRNA in the A-site of the colliding ribosome, generating substrates for Dom34-Hbs1/ABCE1 (D'Orazio *et al.*, 2019; Glover *et al.*, 2020).

The so-far mentioned pathways all deal with collisions in eukaryotes. However, detection of collision events as a signal for problematic translation seems to be a generally conserved mechanism. While it has been known for some time that rescue systems for stuck ribosomes exists in bacteria (Muller *et al.*, 2021), very recent studies revealed that this also involves ribosome collision. Similar to Cue2 in yeast, nuclease SmrB is recruited to collided bacterial ribosomes, cleaves the mRNA in between the collided ribosomes and thus generates ribosomes stalled on truncated mRNA (Saito *et al.*, 2022).

Those mRNAs are a targets for the various bacterial rescue systems employing tmRNA (Moore and Sauer, 2007) or alternatively ArfA and ArfB (Huter *et al*., 2017). Another proposed sensor of collision events in bacteria is MutS2, a protein implicated in splitting of collided ribosomes, promoting the bacterial RQC pathway (Cerullo *et al*., 2022).

This study focused on two different aspects of the quality control mechanisms targeting stalled and collided ribosomes: Rescue and dissociation of collided ribosomes by the RQT complex and inhibition of frameshifting by Mbf1.

Ribosome associated quality control trigger (RQT) complex

Although translational control pathways and ribosomal rescue in particular have been studied extensively over the last years there is still a large knowledge gap on how exactly these pathways function or interplay. Generally, these processes seem to be tightly regulated by the employment of several overlapping, and in some aspects partially redundant mechanisms. One recently emerged and rather well studied pathway dealing with the rescue of stalled ribosomes in eukaryotes is ribosome associated quality control (RQC). Here, recognition and dissociation of stalled ribosomes leads to degradation of the involved mRNA and already translated nascent peptide. Since its discovery RQC was studied in detail, and a large part of the ribosomal rescue process has been described. Still, only in more recent studies, ribosome collisions were identified as the key trigger, leading to ubiquitination of the collided ribosomes by E3 ligase Hel2 and subsequent recognition and dissociation by the RQC trigger (RQT) complex (Hashimoto *et al.*, 2020; Ikeuchi *et al.*, 2019; Juszkiewicz *et al.*, 2018; Juszkiewicz *et al.*, 2020b; Matsuo *et al.*, 2017; Matsuo *et al.*, 2020; Simms *et al.*, 2017; Sitron *et al.*, 2017; Sundaramoorthy *et al.*, 2017). A major goal of this thesis was to elucidate how the RQT complex recognizes the ubiquitinated ribosomes and subsequently leads to splitting. To that end, collided ribosomes representing a bona fide RQT substrate were generated by *in vitro* translation reactions of messages containing non-optimal codons. By introducing an *in vitro* ubiquitination step these substrates could be further optimized, ultimately using them in a reconstitution reaction both for splitting assays and for visualization by cryo-EM.

Prerequisites for RQT binding and RQT mediated splitting

Recruitment of RQT to ribosomes and in particular the commitment to the splitting reaction needs to be very specific for collided ribosomes that cannot continue translation and should not target regulatory pausing mechanisms (such as the translational pause induced by SRP targets). This specificity is thought to be achieved by the selective ubiquitination of collided ribosomes on ribosomal protein uS10 by E3 ligase Hel2 (human ZNF598) (Hashimoto *et al.*, 2020; Juszkiewicz *et al.*, 2018; Matsuo *et al.*, 2017; Narita *et al.*, 2022). Due to their unique collision interface, collided ribosomes can be deliberately recognized and targeted for dissociation by RQT.

In the performed *in vitro* splitting assays, a dependency of the RQT mediated splitting process on ATPase activity of the RQT N-terminal cassette (NTC), availability of a 3' mRNA overhang and indeed sufficient ubiquitination by Hel2 was observed. Another prerequisite for efficient splitting in this system, was the presence of a neighboring ribosome. While *in vitro* ubiquitinated di- and trisomes were dissociated very efficiently (Figure 7), dissociation of ubiquitinated monosomes was incomplete (Figure 8). However, whether the presence of a neighbor is indeed a strict necessity for efficient splitting or rather enables more efficient ubiquitination and subsequent splitting needs to be investigated further.

Along the same lines, the presence of E3 ligase Hel2 on the ribosome might also be necessary for accommodating RQT, especially since the RQT components were initially identified by co-purification with Hel2 and ribosomes (Matsuo *et al.*, 2017). In contrast to the splitting assays, the visualization of stably bound RQT-ribosome complexes in cryo-EM mainly required highly ubiquitinated samples, whereas both the ATPase activity and mRNA overhang were not strictly necessary for obtaining RQT-ribosome complexes. Earlier studies showed hRQT ribosome association even without helicase activity of the N-terminal cassette, however, the levels were quite weak compared to wtRQT (Hashimoto *et al.*, 2020). On top of that, studies by both Juskiewicz and Matsuo, respectively found RQT co-migrating with polysomes even without increased ubiquitination levels (Juszkiewicz *et al.*, 2020b; Matsuo *et al.*, 2017), similar to what was observed before introducing the *in vitro* ubiquitination step (Figure 6). However, in such samples RQT was not visible in cryo-EM and the corresponding splitting assays showed less splitting efficiency compared to the ones performed with *in vitro* ubiquitinated ribosomes. Without sufficient ubiquitination, RQT most likely still associates with polysomes but is not stably accommodated and thus does not lead to splitting.

In the obtained RQT-ribosome structures, the complex was found on the lead ribosome of a collided disome unit (in samples without emerging mRNA or with ATPase deficient RQT) or single 80S ribosomes which represent a non-optimal splitting substrate (Figure 8, gradients of monosomes). Although the incubation times of the reconstitution were very short (5-10 minutes), for actively splitting samples, no stable RQT-disome structure could be observed, however, the splitting products (40S•RQT complex and 60S•peptidyl-tRNA•eIF6) were clearly identifiable. Overall, this points to a rapid splitting process in which RQT recognizes the lead ribosome after Hel2-dependent K63-linked uS10 ubiquitination and immediately leads to subunit dissociation.

Recognition of substrate ribosomes by the RQT complex

Recognition of the ubiquitin-chain is most likely facilitated by the CUE domain of Cue3 or the human homolog ASCC2 (Hashimoto *et al.*, 2020; Matsuo *et al.*, 2017). However, a study in the human system came to the conclusion that this is more likely due to the stabilizing effect of ASCC2 on the RQT complex than the recognition of ubiquitin by the CUE domain, since mutating the CUE domain did not reduce the observed splitting efficiency (Juszkiewicz *et al.*, 2020b). A more recent study provides yet another explanation for these observations: In addition to the interaction of the Cue3 CUE domain with ubiquitin, the N-terminal domain of Rqt4 was found to bind ubiquitin chains (Matsuo *et al.*, 2022). In the presented structures, neither the CUE domain, the N-terminal domain of Rqt4 nor the ubiquitin chain were visible, most likely due to the inherent flexibility of those components. In Alphafold structure predictions of Cue3 (P53137, (Jumper *et al.*, 2021; Varadi *et al.*, 2022)), the CUE domain is connected to the observed N-terminal domain via an unstructured linker and also the Alphafold model of the Rqt4 (P36119) predicts a flexible linker between N-terminus and the observed parts of Rqt4. Those most likely increase the range in which ubiquitin can be detected, an advantage when recognizing the flexible (poly-)ubiquitin chain but detrimental for visualization by cryo-EM. In the above-mentioned study, deletion of both the CUE domain of Cue3 and the N-terminal domain of Rqt4 abolished the binding to a K63-linked ubiquitin chain and inhibited the recruitment of the RQT complex to ubiquitinated collided ribosomes. However, this effect could also be attributed to destabilization of the RQT complex, even though Slh1 seems to be stable when purified on its own (Matsuo *et al.*, 2022).

It is tempting to speculate that the interaction of the two co-factors with the (poly-)ubiquitin chain leads to structural re-arrangement and activation of the RQT complex, upon which RQT can be stably accommodated on the ribosome, similar to what was observed for the inhibitory plug domain in the N-terminal region (NTR) of Slh1 homolog Brr2. Crystal structures of Brr2 in complex with the Jab1 domain of its Prp8 co-factor (pdb 5m52) find the plug-domain (114-154) bound to the mRNA entry of the NTC (Absmeier *et al.*, 2016). Intriguingly, in the Brr2 structure a downstream stretch of the NTR (259-275) is bound in a position closely resembling the position of Rqt4 (344-364) observed in this thesis, suggesting the possibility that binding of the co-factor indeed displaces part of the NTR for activation.

For the human homologs of Slh1 (ASCC3) and Cue3 (ASCC2), the structure of a $ASCC2^{1-434}$•$ASCC3^{1-207}$ complex was determined (Jia *et al.*, 2020), and direct interaction between the two N-terminal regions was observed. The NTR of ASCC3 contains a plug-like domain similar to Brr2 which contacts the N-terminus of ASCC2 via two arms framing the plug-like domain.

Unfortunately, the cryo-EM structures presented in this thesis did not give major hints about this mechanistically still very enigmatic recognition process on collided ribosomes. While the core RQT complex is well resolved, flexible parts that are proposed to mainly contribute to both (poly-)ubiquitin-binding and regulation via the NTR remained invisible. While there is unassigned density in the maps on top of the Cue3 N-terminal domain, the bad resolution and multiple candidates for this position (Cue3, Rqt4 or Slh1 NTR) made identification impossible.

RQT splits the lead ribosome

The obtained structures of RQT-bound ribosomes provide the first mechanistic insight into the RQT-mediated splitting process. They revealed the architecture of RQT-bound ribosomes in various states, bound to stalled disomes, 80S monosomes and even 40S subunits which enabled to propose a model for RQT-mediated splitting. In the disome structure, RQT is bound to the lead ribosome, with only an indirect connection to the collided ribosome via the RACK1-RACK1 interaction. The RQT complex is bound to the ribosome in close proximity to the mRNA entry channel, bridging head and body of the small ribosomal subunit.

Binding of the RQT complex to ribosomes is established by the large helicase component Slh1, which interacts with ribosomal protein uS3 via the HhH and FN3 subdomains in the Sec63 domain of the Slh1 NTC. When binding the ribosome like that, the C-terminal helicase cassette (CTC) is located on top of the NTC, interacting with ribosomal protein RACK1. However, in none of the observed states, mRNA was visible inside the ATP-binding cassettes and further, it was not possible to unambiguously discriminate between ATP and ADP in the Slh1 NTC at the given resolution. Interestingly, the mode of binding differs considerably between RQT and the eponymous Ski2 helicase, which binds the ribosome in a rather similar position. However, Ski2 lacks the Sec63 domain and thus has no equivalent of the HhH and FN3 sub-domains. Instead, Ski2 contacts the ribosome via the RecA2 domain that binds to the tip of helix 16 and then also contacts uS3 and uS10 on the 40S head (Schmidt *et al.*, 2016b).

The overall position of the complex on the first ribosome of a collided disome unit is in agreement with previous data, which found that the lead ribosome is dissociated. In yeast, only the longest nascent chain originating from the lead ribosome was detectable in the 60S fraction of sucrose gradients performed after reconstitution of stalled ribosomes with RQT (Matsuo *et al.*, 2020). In the human system, it was shown that the colliding ribosomes can resume translation after splitting of the lead ribosome: When ribosome collision was induced by mutations in termination release factor eRF1 ($eRF1^{AAQ}$), only full length nascent chains were detected after dissociation of the stalled ribosomes by the human RQT homolog ASCC. In contrast ribosomes stalled by treatment with the antibiotic anisomycin could not continue translation and produced full length and truncated nascent chains (Juszkiewicz *et al.*, 2020b). Similar to the latter, in the employed *in vitro* system, the collided ribosomes cannot continue translating, and were sequentially dissociated as discernible from the lack of a disome peak after trisome dissociation.

In accordance with these previous findings, in the cryo-EM structures of the RQT-ribosome complex, the RQT binding interface on the colliding ribosome is blocked by the lead ribosome and would not be accessible to RQT.

Helicase activity of RQT leads to a conformational change of the ribosome

How does RQT lead to splitting of the lead ribosome? While Ski2, which shows decreased binding to ribosomes when no 3' mRNA is accessible, has been proposed to extract mRNA from stalled ribosomes to enable splitting by Dom34•Hbs1 (Zinoviev *et al.*, 2020), RQT is not extracting mRNA (Juszkiewicz *et al.*, 2020b; Matsuo *et al.*, 2020). In the presented structures, RQT is still binding to the ribosome even in the absence of available mRNA emerging from the entry channel: All captured RQT datasets contained a RQT-ribosome class in which the ribosome adopts a POST state with P/P-tRNA, similar to what has been described for stalled ribosomes or the lead ribosome in di- or trisomes. Since this state was observed in all datasets, also including samples incapable of splitting the ribosomes in splitting assays, it is natural to assume that this is the initial accommodation state of RQT.

Samples with a 3' mRNA overhang on the lead ribosome and NTC ATPase activity of Slh1, contained an additional state in which the 40S is stabilized in an unusual position. While the position of the 40S body relative to the 60S still resembles a POST-state ribosome, the head has undergone a counterclockwise swivel motion. This is similar to a translocation intermediate so far only captured in the presence of eEF2 stabilized by non-hydrolysable GMPPNP (Flis *et al.*, 2018). The head-swivel of the 40S repositions the P/P site tRNA into an pe/E position. RQT mirrors this movement of the ribosome, thereby concomitantly translocating its NTC on helix 16, while the CTC moves closer to the mRNA entry.

This head swivel could be induced by applying force on the mRNA (in opposite direction to normal translation), explaining the necessity of mRNA and ATPase activity for splitting. In favor of this point, human ribosomes stalled on bulky mRNA formed by UV damage are resistant to splitting by RQT, pointing to a requirement for applying a force on the mRNA (Stoneley *et al.*, 2022). Although the mRNA was invisible in all obtained structures, when analyzing the movement and the positions of Slh1s helicase cassettes it seemed plausible that the CTC could act as a helicase to accomplish such a force. The 3' to 5' direction inherent to Ski2-family helicases would favor threading the mRNA through the CTC rather than the NTC, which is, on top of the unfavorable position, (partially) blocked by helix 16. In contrast to Brr2, where the CTC only acts as a regulatory domain and lacks distinct residues necessary for ATPase activity, Slh1 retains those residues in both cassettes. In the human homolog of Slh1 ASCC3, the question with cassette is indeed active remains unclear with either NTC (Jia *et al.*, 2020) or CTC (Dango *et al.*, 2011) or both NTC and CTC (Jia *et al.*, 2022) proposed to be able to unwind DNA. For RNA helicase activity, especially in the context of RQC, mutations of the NTC are not able to rescue read through phenotypes induced by the lack of wt hRQT, while mutations in the CTC lead to a partial rescue (Juszkiewicz *et al.*, 2020b).

In the performed splitting assays, mutations in the NTC targeting a lysine residue involved in ATP binding (K316R, (Matsuo *et al.*, 2017)) or the glutamic acid in the DExD/H motive involved in the release of phosphate after ATP hydrolysis (E428Q, (Xiol *et al.*, 2014)) negatively affected the splitting activity of RQT, although the latter still showed slight splitting activity (Figure 23). Mutations of similar residues in the CTC did not lead to a decrease in splitting efficiency. However, especially when keeping in mind the reaction speed of the frozen cryo-EM samples, the analysis of the splitting reactions on gradients enables us to just observe the final situation after the reaction. Thus, (small) changes in reaction speed will not be resolved in real-time, possibly masking the influence of the CTC mutations. Nevertheless, it is safe to assume that at least *in vitro*, the ATPase activity of the NTC is the main driving force behind the splitting reaction, even though at this point the complete mechanism remains unclear. Further experiments need to be performed addressing this question (see Outlook).

Model of RQT mediated dissociation

Helicase mediated ribosome dissociation is distinct from the previously described mechanism known to generate RQC targets by action of Dom34•Hbs1/ABCE1. Here, steric clashes caused by the involved components lead to dissociation of large and small subunit. While Dom34•Hbs1 preferentially targets ribosomes stalled near the 3' end of a mRNA with a free A-site, RQT is able to resolve internal stalls. Since the Dom34 substrates are easier to recognize as aberrant, the system does not require collisions (and thus ubiquitination) as the decisive trigger the way that the RQT mechanism does. Ubiquitination of the collided ribosome then acts as a signal for RQT to dissociate those ribosomes. Due to the presence of deubiquitinases in the system, this is most likely not an irreversible step. However, if the ubiquitination persists, the ribosome is committed to rescue/degradation by the splitting activity of RQT. Based on the previous results, recognition of the ubiquitin chain by the RQT complex (likely via Rqt4 and Cue3) leads to RQT binding to the 40S of the lead stalled ribosome. Upon ATP hydrolysis, RQT switches conformation, probably also caused by applying force on the mRNA, leading to an unfavorable conformation of the ribosome where the tRNA adopts a chimeric pe/E state. This destabilized state is additionally affecting the trailing collided ribosome, which needs to accommodate the head movement of the leading ribosome to avoid clashes in the RACK1-RACK1 interface. Since leading and colliding ribosome are connected via the mRNA, the possibilities for evasion are restricted. This most likely results in a net movement of the trailing ribosome in the direction of the 60S of the leading ribosome, possibly even dislocating the 60S from its position and committing the lead ribosome to dissociation. Interestingly, a recent study found individual 80S that are dissociated by the RQT complex in the context of nonfunctional rRNA turnover. Here, the splitting is dependent on mono-ubiquitination of ribosomal protein uS3 by Mag2 and ubiquitin chain extension by Fap1 (Li *et al.*, 2022).

How exactly this pathway/mechanism compares to the requirement for collision is yet unclear, especially since this pathway is not dependent on collisions, but overall, this points to ubiquitination as the crucial licensing step for RQT action. In the performed splitting assays, dissociation of single 80S was inefficient, however, in the presence of different factors, there are probably slight adjustments to the RQT splitting mechanism. Even without RQT, internally stalled ribosomes will eventually be dissociated by Dom34 and Hbs1 (Shao *et al*., 2015; Shao *et al*., 2013; Shoemaker *et al.*, 2010). If RQT is overwhelmed/unavailable, collided ribosomes are cleaved upstream of the stalled ribosome by Cue2 (D'Orazio *et al.*, 2019). This cleavage event happens in the A-site of the colliding ribosome, transforming the trailing ribosome into a preferred Dom34•Hbs1 substrate, which can be split by ABCE1.

Multiprotein bridging factor 1 (Mbf1)

If collided ribosomes are not rescued in a timely manner, they tend to frameshift (Simms *et al*., 2019). The colliding ribosome is still translationally competent and only sterically inhibited by the presence of the stalled lead ribosome. Therefore, the collided ribosome continuously applies force on the mRNA. Depending on the nature of the stall, this can lead to the first ribosome 'slipping' on the mRNA and thus resume translation of an out of frame protein. One factor found to mitigate the effect of frameshifting on inhibitory codon sequences together with ribosomal protein uS3, is multiprotein bridging factor 1 (Mbf1)(Wang *et al.*, 2018). This conserved (eukaryotes and archaea) factor was initially identified as a transcriptional co-activator (Li *et al.*, 1994; Takemaru *et al.*, 1997) and has previously been observed to be upregulated upon cellular stress (Tkach *et al*., 2012). The newly proposed function in frameshifting inhibition implies that Mbf1 is not only located in the nucleus but can also be located in the cytoplasm. In the human system, proteomic analysis of polysome fractions after the induction of collisions by low-dose emetine treatment revealed the human homolog of Mbf1, EDF1, to be recruited to collided ribosomes (Sinha *et al.*, 2020). Surprisingly, in yeast, when analyzing collided *SDD1* stalled trisomes for the presence of RQT, instead of RQT, classification revealed classes of ribosomes containing extra density which could be identified as Mbf1.

Based on those results, we set out to understand how Mbf1/EDF1 associates with ribosomes and by that gain mechanistic insight on how this leads to frameshifting inhibition. To compare Mbf1 and the human homolog EDF1, the EDF1-ribosome structure was obtained by a native-pull from cells overexpressing tagged EDF1.

Structures of Mbf1 and EDF1 reveal similar mode of binding

Although EDF1 was enriched in polysome fractions after low-dose emetine treatment (Sinha *et al.*, 2020), no stable structures of EDF1-ribosome complexes could be obtained from such fractions. Instead, cryo-EM analysis of the native pull revealed EDF1 bound to translationally inactive, non-rotated 80S ribosomes containing cell growth-regulating nucleolar protein Ly 1 antibody reactive (LYAR). Intriguingly, this state of the ribosome resembles a state previously described for the native Nsp1-bound 80S ribosome complex with the C-terminus of LYAR occupying the same position in the ribosomal A-site (Thoms *et al.*, 2020). LYAR has so far been described in the context of pre-rRNA processing and negative regulation of the antiviral immune response (Miyazawa *et al.*, 2014; Yang *et al.*, 2019), however, why it is recruited to ribosomes bound to EDF1 or Nsp1 remains unclear.

In contrast to EDF1, Mbf1 could be identified on *SDD1*-stalled ribosomes, with the ribosomes adopting a rotated state with hybrid A/P- and P/E-tRNAs, representing the collided, rather than the stalled ribosomes (POST-state with A-site and P-site tRNAs, Figure 30).

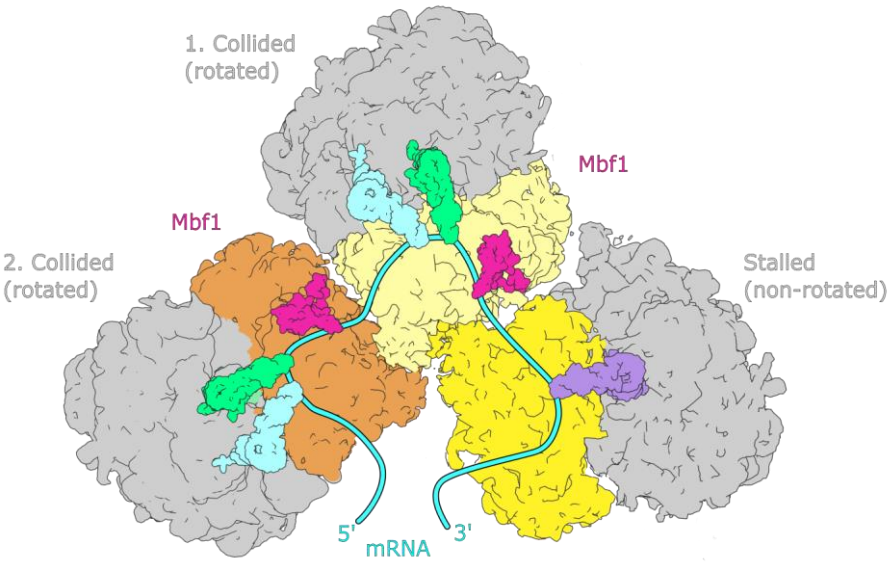

Figure 30: Position of Mbf1 in collided ribosomes.

Mbf1 was only identified on collided ribosomes in a rotated state with A/P and P/E site tRNAs.

In accordance with this, Mbf1 was also observed in structures of Gcn1-bound disomes strictly on the collided ribosomes (Pochopien *et al.*, 2021). In biochemical assays, the same specificity was also observed for EDF1, where low dose treatment with emetine increased the polysome-bound population of EDF1 but not the monosome-bound one (Juszkiewicz *et al.*, 2020a; Sinha *et al.*, 2020). The presence of Mbf1 in the *SDD1* stalled trisomes was unexpected, but may be explained by its high abundancy (85,000 molecules/cell, (Kulak *et al.*, 2014), 43,000-65,000 molecules/cell, (Ho *et al.*, 2018)). In the employed cell-free yeast system, the endogenous Mbf1 levels are high enough to target the produced colliding ribosomes and the interaction is stable enough to survive the following purification procedure.

At first glance, the states that the EDF1/Mbf1-bound ribosomes adopt are very different (rotated with hybrid tRNAs vs. non-rotated with LYAR). However, the 40S conformation itself is comparable, with the only difference being the respective 60S position relative to the 40S. Both Mbf1 and EDF1 bind the ribosome on the small 40S subunit in close proximity to the mRNA entry channel. The C-terminal HTH domain serves as an anchor and is sandwiched between rRNA helix 16 (h16, 40S body) and h33 (40S beak). This domain is well conserved in eukaryotes and archaea, and most likely able to fulfill a ribosome binding function in most organisms. At least for the archaeal homolog it was shown that the HTH domain is crucial for association to both 30S and 70S ribosomes (Blombach *et al.*, 2014). Interestingly, full length archaeal Mbf1 could not complement a Mbf1 deletion in yeast, while a chimeric fusion of the archaeal C-terminus (containing the HTH domain) to the yeast N-terminus restored wild type Mbf1 activity (Marrero Coto *et al.*, 2011), suggesting that the N-terminus function mechanistically differs between yeast and archaea. Following the conserved C-terminal region, the archaeal Mbf1 indeed contains a Zn ribbon motif, whereas in yeast this is followed by the eukaryote specific Mbf1 domain.

In the Mbf1/EDF1-ribosome structure this Mbf1 domain comprises (from C- to N-terminus) the interaction site with ribosomal protein uS3, a stretch displacing ribosomal protein eS30 on h18, an interaction site for the mRNA and an anchor helix (α1) on h16.

Frameshifting inhibition of Mbf1 and EDF1

But how does this observed position explains Mbf1 function in frameshifting inhibition? Earlier studies showed that the frameshifting inhibition activity of Mbf1 is dependent on conserved residues on two α helices of the uS3 middle domain (Wang *et al.*, 2018). In the Mbf1-ribosome structure, these residues are interacting with the α2 helix of Mbf1. This, together with the following interaction site of Mbf1 on rRNA helix 18, positions a conserved KKY (KKW in EDF1) motif in the path of the mRNA. In combination with the α2 helix this motif forms a “headlock’ like arrangement around the mRNA and probably relives the force on the mRNA applied by the colliding ribosome. In addition, the position of the HTH domain in between beak and body of the 40S could in theory prevent the 40S head from swiveling, inhibiting translocation of the tRNAs and thus stabilizing the collision. On the other hand, a head swivel could also disrupt the EDF1/Mbf1 HTH association with h33 and thus lead to dissociation of the proteins from actively translating ribosomes.

Yet the question remains how the described specificity of EDF1/Mbf1 for collided ribosomes is established on a mechanistic level, especially, since in the structures, EDF1 binds non-translating 80S in a similar mode as Mbf1. Either this state resembles an artifact, arising from overexpression of EDF1 in the cells, or EDF1 is also recruited to hibernating ribosomes, similar to CCDC124 or SERBP1 (Wells *et al.*, 2020) in a so-far unknown mechanism.

In contrast to factors like RQT and Cue2, recruitment of EDF1 to collided ribosomes is independent of ZNF598 and loss of EDF1 decreases ubiquitination of eS10 and uS10 as well as ZAKα mediated phosphorylation of protein kinase p38 (Sinha *et al.*, 2020). This fits to Mbf1/EDF1s role as a frameshift inhibitor, since an inhibition of frameshifts in this context amounts to a stabilization of collided ribosomes, which can then be recognized by Hel2/ZNF598. To specifically bind to its substrate, Mbf1/EDF1 needs to distinguish a collided ribosome in a rotated state with hybrid tRNAs from a translation intermediate. One factor here could be the duration in which the ribosome is found in this particular state. During translation this intermediate state is rather short lived, whereas in a collided ribosome the ribosome is locked in this position, increasing the available time for Mbf1/EDF1 recruitment and accommodation. Another possibility to distinguish translating from collided ribosomes is detecting the neighboring ribosome. The conserved N-terminus of both Mbf1 and EDF1 is so far invisible in the structures and could be used as a probe to check for the presence of a leading ribosome. The importance of frameshifting inhibition seems to be different for yeast and human or at least for different underlying stalls. In yeast, Mbf1 knockouts had drastic effects on read through and resulted in +1 frameshifts at inhibitory di-codon sequences (Wang *et al.*, 2018), while in the human system EDF1 knockouts in the context of Xbp1 mediated stalls only lead to moderate -1 frameshifting (Juszkiewicz *et al.*, 2020a). However, frameshifting inhibition is not the only proposed function of EDF1. EDF1 was also found to regulate JUN transcriptional activity (Jindra *et al*., 2004; Miotto and Struhl, 2006; Sinha *et al.*, 2020), thereby regulating transcription of certain proteins after ribosomal collisions.

On top of that, GIGYF2 and EIF4E2 (also known as 4EHP) are also recruited to collided ribosomes by EDF1 (Juszkiewicz *et al.*, 2020a; Sinha *et al.*, 2020). Previous studies showed, that GIGYF2 recruits 4EHP and thus leads to repression of translation via competition with eIF4E for the 5’ mRNA cap (Chapat *et al*., 2017; Cho *et al*., 2005). In earlier studies in human, ZNF598 was found interacting with both 4EHP and GIGYF2 (Morita *et al*., 2012; Tollenaere *et al*., 2019), together repressing translation initiation (Hickey *et al*., 2020). The ZNF598•GIGYF2 interaction was proposed to be independent of EDF1 (Juszkiewicz *et al.*, 2020a). Here, in the suggested model, EDF1 stabilizes a previously formed ZNF598•GIGYF2•4EHP complex on the collided ribosomes. However, GIGYF2•4EHP can also be recruited independent of ZNF598 (Sinha *et al.*, 2020). These results seem contradicting but show how large the knowledge gap for those systems still is. A variety of those pathways are overlapping or act under specific conditions, complicating the process of unraveling the underlying mechanisms. A very recent study in yeast connected frameshifting inhibition on collided ribosomes to even more factors, proposing that elongation factor eEF3 can promote frameshifting, while Gcn1 and Gcn20, which were shown to bind collided ribosomes together with Mbf1 upon starvation conditions (Pochopien *et al.*, 2021), suppress frameshifting (Houston *et al*., 2022). Overall, all these emerging pathways and the interplay between all the involved factors underlines the importance of collided ribosomes as a quality control trigger, but at the same time reveals how much there is still to uncover.

Outlook

While the presented novel RQT structures provide an initial structural and conceptual framework for a helicase driven ribosomal splitting mechanism, several key questions remain unanswered. One of the main issues is that, although there is a dependency on 3' mRNA availability in the splitting assays, the mRNA could not be observed in the RQT-bound ribosome structures. Therefore, it is still unclear how the mRNA is engaged by RQT. On the one hand, it is still necessary to figure out the exact mRNA length required for splitting. On the other hand, the function of the two helicase cassettes needs to be elucidated. The generated E428Q and E1267Q mutants, which impair the release of phosphate after ATP hydrolysis can be used to trap mRNA in the cassettes and to generate cryo-EM samples. In the best case, this will enable direct visualization of the mRNA and by this, structural analysis of the helicase activity. Alternatively, an RNA helicase assay similar to what has already been performed for the human RQT helicase component (Jia *et al.*, 2020; Jia *et al.*, 2022) could yield more information on the cassettes. For all of these approaches, various mutants (in the CTC and NTC but also deletions of the Slh1 NTR) or combination of mutants should be used to ascertain the contribution of both ATPase cassettes. Analysis of the splitting reaction using gradients did not reveal differences in splitting efficiency for the Slh1 CTC mutants compared to the wild type samples. However, by using a method such as mass photometry, one can follow the reaction in real time, enabling a more precise estimation.

Another open point is the recognition of the ubiquitin chain and necessity of Hel2. So far, E3 ligase Hel2 has mainly been implied in ubiquitination leading to subsequent RQT activation. One remaining question is if Hel2 still needs to be present on the ribosome for RQT binding. After the *in vitro* ubiquitination step, Hel2 is still present in the samples and probably can co-pellet with the ribosomes used for cryo-EM samples. To figure out if Hel2 is indeed involved in RQT binding, splitting assays can be performed after removing ribosome associated factors, e.g. by pelleting the *in vitro* ubiquitinated ribosomes through a high salt sucrose cushion. After ubiquitination, both Rqt4 and Cue3 have been proposed to bind (poly)-ubiquitin, however, how long this ubiquitin chain needs to be for efficient recognition and how this recognition leads to accommodation of RQT on the ribosome needs further clarification. Solving the structure of the RQT without the ribosome substrate (possibly in both presence and absence of mRNA) and comparing such a structure to the ribosome-bound state could reveal structural rearrangements and further clarify both how this complex is regulated and the role of the specific components.

So-far, studies suggest a similar mechanism for ribosome dissociation in the yeast and human system. While this thesis provides an initial structure of the yeast RQT-ribosome complex, it will be interesting to repeat the optimized ubiquitination approach for collided human ribosomes and use the obtained insights from the yeast system to reconstitute human RQT (hRQT) and ribosomes.

By this, it should be possible to elucidate the structural basis of the hRQT-ribosome interaction and mode of function.

The second part of the thesis revealed the structures of Mbf1- and EDF1-bound ribosomes, gaining a first idea about the mechanism behind frameshifting inhibition by Mbf1. Since EDF1 could only be visualized on translationally inactive ribosomes, it could be beneficial to aim for purification of endogenous EDF1-ribosome complexes. However, such complexes could not be purified from sucrose gradient fractions containing collided polysomes. One approach could be to reconstitute purified EDF1 with colliding ribosomes, either during *in vitro* translation (similar to Mbf1) or after purification of collided di- and trisomes.

Additionally, the question on how collided ribosomes are recognized by Mbf1/EDF1 is still open. The easiest way to analyze this would be the collection of larger datasets, which could reveal if the N-terminus of the two proteins indeed contacts the neighboring ribosome. Alternatively, mutations in the N-terminus combined with tracing Mbf1/EDF1 association with collided ribosomes could also shed further light on the differentiation between stalled and collided ribosome.

Finally, it would be interesting to look at the proposed associating factors, for both Mbf1 and EDF1 to understand the observed difference in efficiency of frameshift inhibition. Regarding associated factors, also the presence of LYAR in the translationally inactive ribosome raises the question of its functional relevance and could be a target for further studies.

References

Absmeier, E., Rosenberger, L., Apelt, L., Becke, C., Santos, K.F., Stelzl, U., and Wahl, M.C. (2015a). A noncanonical PWI domain in the N-terminal helicase-associated region of the spliceosomal Brr2 protein. Acta Crystallogr D Biol Crystallogr *71*, 762-771. 10.1107/S1399004715001005.

Absmeier, E., Santos, K.F., and Wahl, M.C. (2016). Functions and regulation of the Brr2 RNA helicase during splicing. Cell Cycle *15*, 3362-3377. 10.1080/15384101.2016.1249549.

Absmeier, E., Wollenhaupt, J., Mozaffari-Jovin, S., Becke, C., Lee, C.T., Preussner, M., Heyd, F., Urlaub, H., Luhrmann, R., Santos, K.F., and Wahl, M.C. (2015b). The large N-terminal region of the Brr2 RNA helicase guides productive spliceosome activation. Genes Dev *29*, 2576-2587. 10.1101/gad.271528.115.

Adams, P.D., Afonine, P.V., Bunkoczi, G., Chen, V.B., Davis, I.W., Echols, N., Headd, J.J., Hung, L.W., Kapral, G.J., Grosse-Kunstleve, R.W., *et al*. (2010). PHENIX: a comprehensive Python-based system for macromolecular structure solution. Acta Crystallogr D Biol Crystallogr *66*, 213-221. 10.1107/S0907444909052925.

Agrawal, R.K., Penczek, P., Grassucci, R.A., Li, Y., Leith, A., Nierhaus, K.H., and Frank, J. (1996). Direct visualization of A-, P-, and E-site transfer RNAs in the Escherichia coli ribosome. Science *271*, 1000-1002. 10.1126/science.271.5251.1000.

Agris, P.F. (1991). Wobble position modified nucleosides evolved to select transfer RNA codon recognition: a modified-wobble hypothesis. Biochimie *73*, 1345-1349. 10.1016/0300-9084(91)90163-u.

Aitken, C.E., and Lorsch, J.R. (2012). A mechanistic overview of translation initiation in eukaryotes. Nat Struct Mol Biol *19*, 568-576. 10.1038/nsmb.2303.

Algire, M.A., Maag, D., and Lorsch, J.R. (2005). Pi release from eIF2, not GTP hydrolysis, is the step controlled by start-site selection during eukaryotic translation initiation. Mol Cell *20*, 251-262. 10.1016/j.molcel.2005.09.008.

Alkalaeva, E.Z., Pisarev, A.V., Frolova, L.Y., Kisselev, L.L., and Pestova, T.V. (2006). In vitro reconstitution of eukaryotic translation reveals cooperativity between release factors eRF1 and eRF3. Cell *125*, 1125-1136. 10.1016/j.cell.2006.04.035.

Anderson, J.S., and Parker, R.P. (1998). The 3' to 5' degradation of yeast mRNAs is a general mechanism for mRNA turnover that requires the SKI2 DEVH box protein and 3' to 5' exonucleases of the exosome complex. EMBO J *17*, 1497-1506. 10.1093/emboj/17.5.1497.

Archer, S.K., Shirokikh, N.E., Hallwirth, C.V., Beilharz, T.H., and Preiss, T. (2015). Probing the closed-loop model of mRNA translation in living cells. RNA Biol *12*, 248-254. 10.1080/15476286.2015.1017242.

Aylett, C.H., and Ban, N. (2017). Eukaryotic aspects of translation initiation brought into focus. Philos Trans R Soc Lond B Biol Sci *372*. 10.1098/rstb.2016.0186.

Bai, X.C., Fernandez, I.S., McMullan, G., and Scheres, S.H. (2013). Ribosome structures to near-atomic resolution from thirty thousand cryo-EM particles. Elife *2*, e00461. 10.7554/eLife.00461.

Ban, N., Freeborn, B., Nissen, P., Penczek, P., Grassucci, R.A., Sweet, R., Frank, J., Moore, P.B., and Steitz, T.A. (1998). A 9 A resolution X-ray crystallographic map of the large ribosomal subunit. Cell *93*, 1105-1115. 10.1016/s0092-8674(00)81455-5.

Ban, N., Nissen, P., Hansen, J., Moore, P.B., and Steitz, T.A. (2000). The complete atomic structure of the large ribosomal subunit at 2.4 A resolution. Science *289*, 905-920. 10.1126/science.289.5481.905.

Becker, T., Armache, J.P., Jarasch, A., Anger, A.M., Villa, E., Sieber, H., Motaal, B.A., Mielke, T., Berninghausen, O., and Beckmann, R. (2011). Structure of the no-go mRNA decay complex Dom34-Hbs1 bound to a stalled 80S ribosome. Nat Struct Mol Biol *18*, 715-720. 10.1038/nsmb.2057.

Becker, T., Franckenberg, S., Wickles, S., Shoemaker, C.J., Anger, A.M., Armache, J.P., Sieber, H., Ungewickell, C., Berninghausen, O., Daberkow, I., *et al*. (2012). Structural basis of highly conserved ribosome recycling in eukaryotes and archaea. Nature *482*, 501-506. 10.1038/nature10829.

Behrmann, E., Loerke, J., Budkevich, T.V., Yamamoto, K., Schmidt, A., Penczek, P.A., Vos, M.R., Burger, J., Mielke, T., Scheerer, P., and Spahn, C.M. (2015). Structural snapshots of actively translating human ribosomes. Cell *161*, 845-857. 10.1016/j.cell.2015.03.052.

Ben-Shem, A., Jenner, L., Yusupova, G., and Yusupov, M. (2010). Crystal structure of the eukaryotic ribosome. Science *330*, 1203-1209. 10.1126/science.1194294.

Benne, R., and Hershey, J.W. (1978). The mechanism of action of protein synthesis initiation factors from rabbit reticulocytes. J Biol Chem *253*, 3078-3087.

Bepler, T., Morin, A., Rapp, M., Brasch, J., Shapiro, L., Noble, A.J., and Berger, B. (2019). Positive-unlabeled convolutional neural networks for particle picking in cryo-electron micrographs. Nat Methods *16*, 1153-1160. 10.1038/s41592-019-0575-8.

Berg, P., and Offengand, E.J. (1958). An Enzymatic Mechanism for Linking Amino Acids to RNA. Proc Natl Acad Sci U S A *44*, 78-86. 10.1073/pnas.44.2.78.

Best, K., Ikeuchi, K., Kater, L., Best, D., Musial, J., Matsuo, Y., Berninghausen, O., Becker, T., Inada, T., and Beckmann, R. (2022). Clearing of ribosome collisions by the ribosome quality control trigger complex RQT. bioRxiv, 2022.2004.2019.488791. 10.1101/2022.04.19.488791.

Beznoskova, P., Gunisova, S., and Valasek, L.S. (2016). Rules of UGA-N decoding by near-cognate tRNAs and analysis of readthrough on short uORFs in yeast. RNA *22*, 456-466. 10.1261/rna.054452.115.

Biederer, T., Volkwein, C., and Sommer, T. (1997). Role of Cue1p in ubiquitination and degradation at the ER surface. Science *278*, 1806-1809. 10.1126/science.278.5344.1806.

Blombach, F., Launay, H., Snijders, A.P., Zorraquino, V., Wu, H., de Koning, B., Brouns, S.J., Ettema, T.J., Camilloni, C., Cavalli, A., *et al*. (2014). Archaeal MBF1 binds to 30S and 70S ribosomes via its helix-turn-helix domain. Biochem J *462*, 373-384. 10.1042/BJ20131474.

Booth, C. (2012). K2: A super-resolution electron counting direct detection camera for cryo-EM. Microscopy and Microanalysis *18*, 78-79.

Brandman, O., and Hegde, R.S. (2016). Ribosome-associated protein quality control. Nat Struct Mol Biol *23*, 7-15. 10.1038/nsmb.3147.

Brandman, O., Stewart-Ornstein, J., Wong, D., Larson, A., Williams, C.C., Li, G.W., Zhou, S., King, D., Shen, P.S., Weibezahn, J., *et al*. (2012). A ribosome-bound quality control complex triggers degradation of nascent peptides and signals translation stress. Cell *151*, 1042-1054. 10.1016/j.cell.2012.10.044.

Brickner, J.R., Soll, J.M., Lombardi, P.M., Vagbo, C.B., Mudge, M.C., Oyeniran, C., Rabe, R., Jackson, J., Sullender, M.E., Blazosky, E., *et al*. (2017). A ubiquitin-dependent signalling axis specific for ALKBH-mediated DNA dealkylation repair. Nature *551*, 389-393. 10.1038/nature24484.

Brilot, A.F., Chen, J.Z., Cheng, A., Pan, J., Harrison, S.C., Potter, C.S., Carragher, B., Henderson, R., and Grigorieff, N. (2012). Beam-induced motion of vitrified specimen on holey carbon film. J Struct Biol *177*, 630-637. 10.1016/j.jsb.2012.02.003.

Brink, J., and Chiu, W. (1994). Applications of a slow-scan CCD camera in protein electron crystallography. J Struct Biol *113*, 23-34. 10.1006/jsbi.1994.1029.

Brown, A., Long, F., Nicholls, R.A., Toots, J., Emsley, P., and Murshudov, G. (2015a). Tools for macromolecular model building and refinement into electron cryo-microscopy reconstructions. Acta Crystallogr D Biol Crystallogr *71*, 136-153. 10.1107/S1399004714021683.

Brown, A., Shao, S., Murray, J., Hegde, R.S., and Ramakrishnan, V. (2015b). Structural basis for stop codon recognition in eukaryotes. Nature *524*, 493-496. 10.1038/nature14896.

Brown, C.E., and Sachs, A.B. (1998). Poly(A) tail length control in Saccharomyces cerevisiae occurs by message-specific deadenylation. Mol Cell Biol *18*, 6548-6559. 10.1128/MCB.18.11.6548.

Budkevich, T., Giesebrecht, J., Altman, R.B., Munro, J.B., Mielke, T., Nierhaus, K.H., Blanchard, S.C., and Spahn, C.M. (2011). Structure and dynamics of the mammalian ribosomal pretranslocation complex. Mol Cell *44*, 214-224. 10.1016/j.molcel.2011.07.040.

Buttner, K., Nehring, S., and Hopfner, K.P. (2007). Structural basis for DNA duplex separation by a superfamily-2 helicase. Nat Struct Mol Biol *14*, 647-652. 10.1038/nsmb1246.

Campbell, M.G., Cheng, A., Brilot, A.F., Moeller, A., Lyumkis, D., Veesler, D., Pan, J., Harrison, S.C., Potter, C.S., Carragher, B., and Grigorieff, N. (2012). Movies of ice-embedded particles enhance resolution in electron cryo-microscopy. Structure *20*, 1823-1828. 10.1016/j.str.2012.08.026.

Cardone, G., Heymann, J.B., and Steven, A.C. (2013). One number does not fit all: mapping local variations in resolution in cryo-EM reconstructions. J Struct Biol *184*, 226-236. 10.1016/j.jsb.2013.08.002.

Carter, A.P., Clemons, W.M., Brodersen, D.E., Morgan-Warren, R.J., Wimberly, B.T., and Ramakrishnan, V. (2000). Functional insights from the structure of the 30S ribosomal subunit and its interactions with antibiotics. Nature *407*, 340-348. 10.1038/35030019.

Cate, J.H., Yusupov, M.M., Yusupova, G.Z., Earnest, T.N., and Noller, H.F. (1999). X-ray crystal structures of 70S ribosome functional complexes. Science *285*, 2095-2104. 10.1126/science.285.5436.2095.

Cech, T.R. (2000). Structural biology. The ribosome is a ribozyme. Science *289*, 878-879. 10.1126/science.289.5481.878.

Cerullo, F., Filbeck, S., Patil, P.R., Hung, H.C., Xu, H., Vornberger, J., Hofer, F.W., Schmitt, J., Kramer, G., Bukau, B., *et al*. (2022). Bacterial ribosome collision sensing by a MutS DNA repair ATPase paralogue. Nature *603*, 509-514. 10.1038/s41586-022-04487-6.

Chandrasekaran, V., Juszkiewicz, S., Choi, J., Puglisi, J.D., Brown, A., Shao, S., Ramakrishnan, V., and Hegde, R.S. (2019). Mechanism of ribosome stalling during translation of a poly(A) tail. Nat Struct Mol Biol *26*, 1132-1140. 10.1038/s41594-019-0331-x.

Chapat, C., Jafarnejad, S.M., Matta-Camacho, E., Hesketh, G.G., Gelbart, I.A., Attig, J., Gkogkas, C.G., Alain, T., Stern-Ginossar, N., Fabian, M.R., *et al*. (2017). Cap-binding protein 4EHP effects translation silencing by microRNAs. Proc Natl Acad Sci U S A *114*, 5425-5430. 10.1073/pnas.1701488114.

Chen, V.B., Arendall, W.B., 3rd, Headd, J.J., Keedy, D.A., Immormino, R.M., Kapral, G.J., Murray, L.W., Richardson, J.S., and Richardson, D.C. (2010). MolProbity: all-atom structure validation for macromolecular crystallography. Acta Crystallogr D Biol Crystallogr *66*, 12-21. 10.1107/S0907444909042073.

Cheng, Y., Grigorieff, N., Penczek, P.A., and Walz, T. (2015). A primer to single-particle cryo-electron microscopy. Cell *161*, 438-449. 10.1016/j.cell.2015.03.050.

Chiu, W.F., and Glaeser, R.M. (1977). Factors affecting high resolution fixed-beam transmission electron microscopy. Ultramicroscopy. doi: 10.1016/s0304-3991(76)91334-6.

Cho, P.F., Poulin, F., Cho-Park, Y.A., Cho-Park, I.B., Chicoine, J.D., Lasko, P., and Sonenberg, N. (2005). A new paradigm for translational control: inhibition via 5'-3' mRNA tethering by Bicoid and the eIF4E cognate 4EHP. Cell *121*, 411-423. 10.1016/j.cell.2005.02.024.

Choe, Y.J., Park, S.H., Hassemer, T., Korner, R., Vincenz-Donnelly, L., Hayer-Hartl, M., and Hartl, F.U. (2016). Failure of RQC machinery causes protein aggregation and proteotoxic stress. Nature *531*, 191-195. 10.1038/nature16973.

Chu, J., Hong, N.A., Masuda, C.A., Jenkins, B.V., Nelms, K.A., Goodnow, C.C., Glynne, R.J., Wu, H., Masliah, E., Joazeiro, C.A., and Kay, S.A. (2009). A mouse forward genetics screen identifies LISTERIN as an E3 ubiquitin ligase involved in neurodegeneration. Proc Natl Acad Sci U S A *106*, 2097-2103. 10.1073/pnas.0812819106.

Clemons, W.M., Jr., May, J.L., Wimberly, B.T., McCutcheon, J.P., Capel, M.S., and Ramakrishnan, V. (1999). Structure of a bacterial 30S ribosomal subunit at 5.5 A resolution. Nature *400*, 833-840. 10.1038/23631.

Collart, M.A., and Weiss, B. (2020). Ribosome pausing, a dangerous necessity for co-translational events. Nucleic Acids Res *48*, 1043-1055. 10.1093/nar/gkz763.

Conard, S.E., Buckley, J., Dang, M., Bedwell, G.J., Carter, R.L., Khass, M., and Bedwell, D.M. (2012). Identification of eRF1 residues that play critical and complementary roles in stop codon recognition. RNA *18*, 1210-1221. 10.1261/rna.031997.111.

Crick, F.H. (1966). Codon--anticodon pairing: the wobble hypothesis. J Mol Biol *19*, 548-555. 10.1016/s0022-2836(66)80022-0.

Crick, F.H., Barnett, L., Brenner, S., and Watts-Tobin, R.J. (1961). General nature of the genetic code for proteins. Nature *192*, 1227-1232. 10.1038/1921227a0.

Culbertson, M.R., Gaber, R.F., and Cummins, C.M. (1982). Frameshift suppression in Saccharomyces cerevisiae. V. Isolation and genetic properties of nongroup-specific suppressors. Genetics *102*, 361-378. 10.1093/genetics/102.3.361.

D'Orazio, K.N., Wu, C.C., Sinha, N., Loll-Krippleber, R., Brown, G.W., and Green, R. (2019). The endonuclease Cue2 cleaves mRNAs at stalled ribosomes during No Go Decay. Elife *8*. 10.7554/eLife.49117.

Dango, S., Mosammaparast, N., Sowa, M.E., Xiong, L.J., Wu, F., Park, K., Rubin, M., Gygi, S., Harper, J.W., and Shi, Y. (2011). DNA unwinding by ASCC3 helicase is coupled to ALKBH3-dependent DNA alkylation repair and cancer cell proliferation. Mol Cell *44*, 373-384. 10.1016/j.molcel.2011.08.039.

Daugeron, M.C., Prouteau, M., Lacroute, F., and Seraphin, B. (2011). The highly conserved eukaryotic DRG factors are required for efficient translation in a manner redundant with the putative RNA helicase Slh1. Nucleic Acids Res *39*, 2221-2233. 10.1093/nar/gkq898.

Davis, I.W., Leaver-Fay, A., Chen, V.B., Block, J.N., Kapral, G.J., Wang, X., Murray, L.W., Arendall, W.B., 3rd, Snoeyink, J., Richardson, J.S., and Richardson, D.C. (2007). MolProbity: all-atom contacts and structure validation for proteins and nucleic acids. Nucleic Acids Res *35*, W375-383. 10.1093/nar/gkm216.

Defenouillere, Q., Yao, Y., Mouaikel, J., Namane, A., Galopier, A., Decourty, L., Doyen, A., Malabat, C., Saveanu, C., Jacquier, A., and Fromont-Racine, M. (2013). Cdc48-associated complex bound to 60S particles is required for the clearance of aberrant translation products. Proc Natl Acad Sci U S A *110*, 5046-5051. 10.1073/pnas.1221724110.

Demeshkina, N., Jenner, L., Westhof, E., Yusupov, M., and Yusupova, G. (2012). A new understanding of the decoding principle on the ribosome. Nature *484*, 256-259. 10.1038/nature10913.

Deptuch, G., Besson, A., Rehak, P., Szelezniak, M., Wall, J., Winter, M., and Zhu, Y. (2007). Direct electron imaging in electron microscopy with monolithic active pixel sensors. Ultramicroscopy *107*, 674-684. 10.1016/j.ultramic.2007.01.003.

Dever, T.E., Dinman, J.D., and Green, R. (2018). Translation Elongation and Recoding in Eukaryotes. Cold Spring Harb Perspect Biol *10*. 10.1101/cshperspect.a032649.

Diament, A., Feldman, A., Schochet, E., Kupiec, M., Arava, Y., and Tuller, T. (2018). The extent of ribosome queuing in budding yeast. PLoS Comput Biol *14*, e1005951. 10.1371/journal.pcbi.1005951.

Dintzis, H.M. (1961). ASSEMBLY OF THE PEPTIDE CHAINS OF HEMOGLOBIN. Proceedings of the National Academy of Sciences *47*, 247-261. doi:10.1073/pnas.47.3.247.

Doma, M.K., and Parker, R. (2006). Endonucleolytic cleavage of eukaryotic mRNAs with stalls in translation elongation. Nature *440*, 561-564. 10.1038/nature04530.

Downing, K.H., and Grano, D.A. (1982). Analysis of photographic emulsions for electron microscopy of two-dimensional crystalline specimens. Ultramicroscopy *7*, 381-403. https://doi.org/10.1016/0304-3991(82)90262-5.

Dubochet, J., Adrian, M., Chang, J.J., Homo, J.C., Lepault, J., McDowall, A.W., and Schultz, P. (1988). Cryo-electron microscopy of vitrified specimens. Q Rev Biophys *21*, 129-228. 10.1017/s0033583500004297.

Dubochet, J., Ducommun, M., Zollinger, M., and Kellenberger, E. (1971). A new preparation method for dark-field electron microscopy of biomacromolecules. J Ultrastruct Res *35*, 147-167. 10.1016/s0022-5320(71)80148-x.

Edenberg, E.R., Downey, M., and Toczyski, D. (2014). Polymerase stalling during replication, transcription and translation. Curr Biol *24*, R445-452. 10.1016/j.cub.2014.03.060.

Emsley, P., Lohkamp, B., Scott, W.G., and Cowtan, K. (2010). Features and development of Coot. Acta Crystallogr D Biol Crystallogr *66*, 486-501. 10.1107/S0907444910007493.

Ermantraut, E., Wohlfart, K., and Tichelaar, W. (1998). Perforated support foils with pre-defined hole size, shape and arrangement. Ultramicroscopy *74*, 75-81.

Farabaugh, P.J. (1996). Programmed translational frameshifting. Microbiol Rev *60*, 103-134. 10.1128/mr.60.1.103-134.1996.

Faruqi, A.R., Cattermole, D.M., and Raeburn, C. (2003). Direct electron detection methods in electron microscopy. Nuclear Instruments and Methods in Physics Research Section A: Accelerators, Spectrometers, Detectors and Associated Equipment *513*, 317-321. https://doi.org/10.1016/j.nima.2003.08.055.

Faruqi, A.R., and McMullan, G. (2011). Electronic detectors for electron microscopy. Q Rev Biophys *44*, 357-390. 10.1017/S0033583511000035.

Feathers, J.R., Spoth, K.A., and Fromme, J.C. (2021). Experimental evaluation of super-resolution imaging and magnification choice in single-particle cryo-EM. J Struct Biol X *5*, 100047. 10.1016/j.yjsbx.2021.100047.

Flis, J., Holm, M., Rundlet, E.J., Loerke, J., Hilal, T., Dabrowski, M., Burger, J., Mielke, T., Blanchard, S.C., Spahn, C.M.T., and Budkevich, T.V. (2018). tRNA Translocation by the Eukaryotic 80S Ribosome and the Impact of GTP Hydrolysis. Cell Rep *25*, 2676-2688 e2677. 10.1016/j.celrep.2018.11.040.

Frank, J., and Agrawal, R.K. (2000). A ratchet-like inter-subunit reorganization of the ribosome during translocation. Nature *406*, 318-322. 10.1038/35018597.

Frank, J., and Al-Ali, L. (1975). Signal-to-noise ratio of electron micrographs obtained by cross correlation. Nature *256*, 376-379. 10.1038/256376a0.

Frank, J., Zhu, J., Penczek, P., Li, Y., Srivastava, S., Verschoor, A., Radermacher, M., Grassucci, R., Lata, R.K., and Agrawal, R.K. (1995). A model of protein synthesis based on cryo-electron microscopy of the E. coli ribosome. Nature *376*, 441-444. 10.1038/376441a0.

Frolova, L.Y., Tsivkovskii, R.Y., Sivolobova, G.F., Oparina, N.Y., Serpinsky, O.I., Blinov, V.M., Tatkov, S.I., and Kisselev, L.L. (1999). Mutations in the highly conserved GGQ motif of class 1 polypeptide release factors abolish ability of human eRF1 to trigger peptidyl-tRNA hydrolysis. RNA *5*, 1014-1020. 10.1017/s135583829999043x.

Fujii, K., Kitabatake, M., Sakata, T., Miyata, A., and Ohno, M. (2009). A role for ubiquitin in the clearance of nonfunctional rRNAs. Genes Dev *23*, 963-974. 10.1101/gad.1775609.

Fujii, K., Kitabatake, M., Sakata, T., and Ohno, M. (2012). 40S subunit dissociation and proteasome-dependent RNA degradation in nonfunctional 25S rRNA decay. EMBO J *31*, 2579-2589. 10.1038/emboj.2012.85.

Gamble, C.E., Brule, C.E., Dean, K.M., Fields, S., and Grayhack, E.J. (2016). Adjacent Codons Act in Concert to Modulate Translation Efficiency in Yeast. Cell *166*, 679-690. 10.1016/j.cell.2016.05.070.

Gan, L., Chen, S., and Jensen, G.J. (2008). Molecular organization of Gram-negative peptidoglycan. Proc Natl Acad Sci U S A *105*, 18953-18957. 10.1073/pnas.0808035105.

Garcia-Barrio, M., Dong, J., Ufano, S., and Hinnebusch, A.G. (2000). Association of GCN1-GCN20 regulatory complex with the N-terminus of eIF2alpha kinase GCN2 is required for GCN2 activation. EMBO J *19*, 1887-1899. 10.1093/emboj/19.8.1887.

Garzia, A., Jafarnejad, S.M., Meyer, C., Chapat, C., Gogakos, T., Morozov, P., Amiri, M., Shapiro, M., Molina, H., Tuschl, T., and Sonenberg, N. (2017). The E3 ubiquitin ligase and RNA-binding protein ZNF598 orchestrates ribosome quality control of premature polyadenylated mRNAs. Nat Commun *8*, 16056. 10.1038/ncomms16056.

Gerber, A.P., and Keller, W. (1999). An adenosine deaminase that generates inosine at the wobble position of tRNAs. Science *286*, 1146-1149. 10.1126/science.286.5442.1146.

Glaeser, R.M. (2018). Proteins, Interfaces, and Cryo-Em Grids. Curr Opin Colloid Interface Sci *34*, 1-8. 10.1016/j.cocis.2017.12.009.

Glick, B.R., and Ganoza, M.C. (1975). Identification of a soluble protein that stimulates peptide bond synthesis. Proc Natl Acad Sci U S A *72*, 4257-4260. 10.1073/pnas.72.11.4257.

Glover, M.L., Burroughs, A.M., Monem, P.C., Egelhofer, T.A., Pule, M.N., Aravind, L., and Arribere, J.A. (2020). NONU-1 Encodes a Conserved Endonuclease Required for mRNA Translation Surveillance. Cell Rep *30*, 4321-4331 e4324. 10.1016/j.celrep.2020.03.023.

Goddard, T.D., Huang, C.C., Meng, E.C., Pettersen, E.F., Couch, G.S., Morris, J.H., and Ferrin, T.E. (2018). UCSF ChimeraX: Meeting modern challenges in visualization and analysis. Protein Sci *27*, 14-25. 10.1002/pro.3235.

Grant, T., and Grigorieff, N. (2015). Measuring the optimal exposure for single particle cryo-EM using a 2.6 A reconstruction of rotavirus VP6. Elife *4*, e06980. 10.7554/eLife.06980.

Grant, T., Rohou, A., and Grigorieff, N. (2018). cisTEM, user-friendly software for single-particle image processing. Elife *7*. 10.7554/eLife.35383.

Gregio, A.P., Cano, V.P., Avaca, J.S., Valentini, S.R., and Zanelli, C.F. (2009). eIF5A has a function in the elongation step of translation in yeast. Biochem Biophys Res Commun *380*, 785-790. 10.1016/j.bbrc.2009.01.148.

Grigorieff, N. (2000). Resolution measurement in structures derived from single particles. Acta Crystallogr D Biol Crystallogr *56*, 1270-1277. 10.1107/s0907444900009549.

Gutierrez, E., Shin, B.S., Woolstenhulme, C.J., Kim, J.R., Saini, P., Buskirk, A.R., and Dever, T.E. (2013). eIF5A promotes translation of polyproline motifs. Mol Cell *51*, 35-45. 10.1016/j.molcel.2013.04.021.

Guydosh, N.R., and Green, R. (2014). Dom34 rescues ribosomes in 3' untranslated regions. Cell *156*, 950-962. 10.1016/j.cell.2014.02.006.

Guydosh, N.R., Kimmig, P., Walter, P., and Green, R. (2017). Regulated Ire1-dependent mRNA decay requires no-go mRNA degradation to maintain endoplasmic reticulum homeostasis in S. pombe. Elife *6*. 10.7554/eLife.29216.

Han, P., Shichino, Y., Schneider-Poetsch, T., Mito, M., Hashimoto, S., Udagawa, T., Kohno, K., Yoshida, M., Mishima, Y., Inada, T., and Iwasaki, S. (2020). Genome-wide Survey of Ribosome Collision. Cell Rep *31*, 107610. 10.1016/j.celrep.2020.107610.

Harauz, G., and van Heel, M. (1986). Exact filters for general geometry three dimensional reconstruction. Optik. *73*, 146-156.

Harding, H.P., Ordonez, A., Allen, F., Parts, L., Inglis, A.J., Williams, R.L., and Ron, D. (2019). The ribosomal P-stalk couples amino acid starvation to GCN2 activation in mammalian cells. Elife *8*. 10.7554/eLife.50149.

Hashimoto, S., Sugiyama, T., Yamazaki, R., Nobuta, R., and Inada, T. (2020). Identification of a novel trigger complex that facilitates ribosome-associated quality control in mammalian cells. Sci Rep *10*, 3422. 10.1038/s41598-020-60241-w.

Heel, M.v., Portugal, R.V., and Schatz, M. (2016). Multivariate Statistical Analysis of Large Datasets: Single Particle Electron Microscopy. Open Journal of Statistics *06*, 701-739. 10.4236/ojs.2016.64059.

Henderson, R. (2013). Avoiding the pitfalls of single particle cryo-electron microscopy: Einstein from noise. Proc Natl Acad Sci U S A *110*, 18037-18041. 10.1073/pnas.1314449110.

Heuer, A., Gerovac, M., Schmidt, C., Trowitzsch, S., Preis, A., Kotter, P., Berninghausen, O., Becker, T., Beckmann, R., and Tampe, R. (2017). Structure of the 40S-ABCE1 post-splitting complex in ribosome recycling and translation initiation. Nat Struct Mol Biol *24*, 453-460. 10.1038/nsmb.3396.

Hickey, K.L., Dickson, K., Cogan, J.Z., Replogle, J.M., Schoof, M., D'Orazio, K.N., Sinha, N.K., Hussmann, J.A., Jost, M., Frost, A., *et al*. (2020). GIGYF2 and 4EHP Inhibit Translation Initiation of Defective Messenger RNAs to Assist Ribosome-Associated Quality Control. Mol Cell *79*, 950-962 e956. 10.1016/j.molcel.2020.07.007.

Hilal, T., Yamamoto, H., Loerke, J., Burger, J., Mielke, T., and Spahn, C.M. (2016). Structural insights into ribosomal rescue by Dom34 and Hbs1 at near-atomic resolution. Nat Commun *7*, 13521. 10.1038/ncomms13521.

Ho, B., Baryshnikova, A., and Brown, G.W. (2018). Unification of Protein Abundance Datasets Yields a Quantitative Saccharomyces cerevisiae Proteome. Cell Syst *6*, 192-205 e193. 10.1016/j.cels.2017.12.004.

Horne, R.W. (1964). Some Recent Applications of Negative-Staining Methods to the Study of Biological Structure in the Electron Microscope. J R Microsc Soc *83*, 169-177. 10.1111/j.1365-2818.1964.tb00526.x.

Houston, L., Platten, E.M., Connelly, S.M., Wang, J., and Grayhack, E.J. (2022). Frameshifting at collided ribosomes is modulated by elongation factor eEF3 and by integrated stress response regulators Gcn1 and Gcn20. RNA *28*, 320-339. 10.1261/rna.078964.121.

Hsu, C.L., and Stevens, A. (1993). Yeast cells lacking 5'-->3' exoribonuclease 1 contain mRNA species that are poly(A) deficient and partially lack the 5' cap structure. Mol Cell Biol *13*, 4826-4835. 10.1128/mcb.13.8.4826-4835.1993.

Huter, P., Muller, C., Arenz, S., Beckert, B., and Wilson, D.N. (2017). Structural Basis for Ribosome Rescue in Bacteria. Trends Biochem Sci *42*, 669-680. 10.1016/j.tibs.2017.05.009.

Ikeuchi, K., Ivic, N., Cheng, J., Buschauer, R., Matsuo, Y., Fröhlich, T., Berninghausen, O., Inada, T., Becker, T., and Beckmann, R. (2021). Recognition and deubiquitination of free 40S for translational reset by Otu2. bioRxiv, 2021.2011.2017.468975. 10.1101/2021.11.17.468975.

Ikeuchi, K., Tesina, P., Matsuo, Y., Sugiyama, T., Cheng, J., Saeki, Y., Tanaka, K., Becker, T., Beckmann, R., and Inada, T. (2019). Collided ribosomes form a unique structural interface to induce Hel2-driven quality control pathways. EMBO J *38*. 10.15252/embj.2018100276.

Inglis, A.J., Masson, G.R., Shao, S., Perisic, O., McLaughlin, S.H., Hegde, R.S., and Williams, R.L. (2019). Activation of GCN2 by the ribosomal P-stalk. Proc Natl Acad Sci U S A *116*, 4946-4954. 10.1073/pnas.1813352116.

Ishikawa, K., Ito, K., Inoue, J., and Semba, K. (2013). Cell growth control by stable Rbg2/Gir2 complex formation under amino acid starvation. Genes Cells *18*, 859-872. 10.1111/gtc.12082.

Ishimura, R., Nagy, G., Dotu, I., Chuang, J.H., and Ackerman, S.L. (2016). Activation of GCN2 kinase by ribosome stalling links translation elongation with translation initiation. Elife *5*. 10.7554/eLife.14295.

J. Dubochet, A.W.M. (1981). Vitrification of pure water for Electron Microscopy. Journal of Microscopy *124*, RP3-RP4.

Jain, T., Sheehan, P., Crum, J., Carragher, B., and Potter, C.S. (2012). Spotiton: a prototype for an integrated inkjet dispense and vitrification system for cryo-TEM. J Struct Biol *179*, 68-75. 10.1016/j.jsb.2012.04.020.

Jamali, K., Kimanius, D., and Scheres, S. (2022). ModelAngelo: Automated Model Building in Cryo-EM Maps. arXiv preprint arXiv:2210.00006.

James, L.K., and Augenstein, L.G. (1966). Adsorption of enzymes at interfaces: film formation and the effect on activity. Adv Enzymol Relat Areas Mol Biol *28*, 1-40. 10.1002/9780470122730.ch1.

Jermy, A.J., Willer, M., Davis, E., Wilkinson, B.M., and Stirling, C.J. (2006). The Brl domain in Sec63p is required for assembly of functional endoplasmic reticulum translocons. J Biol Chem *281*, 7899-7906. 10.1074/jbc.M511402200.

Jia, J., Absmeier, E., Holton, N., Pietrzyk-Brzezinska, A.J., Hackert, P., Bohnsack, K.E., Bohnsack, M.T., and Wahl, M.C. (2020). The interaction of DNA repair factors ASCC2 and ASCC3 is affected by somatic cancer mutations. Nat Commun *11*, 5535. 10.1038/s41467-020-19221-x.

Jia, J., Hilal, T., Bohnsack, K., Chernev, A., Tsao, N., Schwarz, J., Arumugam, A., Parmely, L., Holton, N., Loll, B., *et al*. (2022). Extended DNA threading through a dual-engine motor module in the activating signal co-integrator complex. Research Square. 10.21203/rs.3.rs-2007381/v1.

Jindra, M., Gaziova, I., Uhlirova, M., Okabe, M., Hiromi, Y., and Hirose, S. (2004). Coactivator MBF1 preserves the redox-dependent AP-1 activity during oxidative stress in Drosophila. EMBO J *23*, 3538-3547. 10.1038/sj.emboj.7600356.

Joazeiro, C.A.P. (2019). Mechanisms and functions of ribosome-associated protein quality control. Nat Rev Mol Cell Biol *20*, 368-383. 10.1038/s41580-019-0118-2.

Johnson, S.J., and Jackson, R.N. (2013). Ski2-like RNA helicase structures: common themes and complex assemblies. RNA Biol *10*, 33-43. 10.4161/rna.22101.

Jumper, J., Evans, R., Pritzel, A., Green, T., Figurnov, M., Ronneberger, O., Tunyasuvunakool, K., Bates, R., Zidek, A., Potapenko, A., *et al*. (2021). Highly accurate protein structure prediction with AlphaFold. Nature *596*, 583-589. 10.1038/s41586-021-03819-2.

Juszkiewicz, S., Chandrasekaran, V., Lin, Z., Kraatz, S., Ramakrishnan, V., and Hegde, R.S. (2018). ZNF598 Is a Quality Control Sensor of Collided Ribosomes. Mol Cell *72*, 469-481 e467. 10.1016/j.molcel.2018.08.037.

Juszkiewicz, S., and Hegde, R.S. (2017). Initiation of Quality Control during Poly(A) Translation Requires Site-Specific Ribosome Ubiquitination. Mol Cell *65*, 743-750 e744. 10.1016/j.molcel.2016.11.039.

Juszkiewicz, S., Slodkowicz, G., Lin, Z., Freire-Pritchett, P., Peak-Chew, S.Y., and Hegde, R.S. (2020a). Ribosome collisions trigger cis-acting feedback inhibition of translation initiation. Elife *9*. 10.7554/eLife.60038.

Juszkiewicz, S., Speldewinde, S.H., Wan, L., Svejstrup, J.Q., and Hegde, R.S. (2020b). The ASC-1 Complex Disassembles Collided Ribosomes. Mol Cell *79*, 603-614 e608. 10.1016/j.molcel.2020.06.006.

Kang, R.S., Daniels, C.M., Francis, S.A., Shih, S.C., Salerno, W.J., Hicke, L., and Radhakrishnan, I. (2003). Solution structure of a CUE-ubiquitin complex reveals a conserved mode of ubiquitin binding. Cell *113*, 621-630. 10.1016/s0092-8674(03)00362-3.

Kelly, D.F., Dukovski, D., and Walz, T. (2010). Strategy for the use of affinity grids to prepare non-His-tagged macromolecular complexes for single-particle electron microscopy. J Mol Biol *400*, 675-681. 10.1016/j.jmb.2010.05.045.

Kemper, W.M., Berry, K.W., and Merrick, W.C. (1976). Purification and properties of rabbit reticulocyte protein synthesis initiation factors M2Balpha and M2Bbeta. J Biol Chem *251*, 5551-5557.

Kenna, M., Stevens, A., McCammon, M., and Douglas, M.G. (1993). An essential yeast gene with homology to the exonuclease-encoding XRN1/KEM1 gene also encodes a protein with exoribonuclease activity. Mol Cell Biol *13*, 341-350. 10.1128/mcb.13.1.341-350.1993.

Kim, D.H., and Rossi, J.J. (1999). The first ATPase domain of the yeast 246-kDa protein is required for in vivo unwinding of the U4/U6 duplex. RNA *5*, 959-971. 10.1017/s135583829999012x.

Kim, H.J., Yi, J.Y., Sung, H.S., Moore, D.D., Jhun, B.H., Lee, Y.C., and Lee, J.W. (1999). Activating signal cointegrator 1, a novel transcription coactivator of nuclear receptors, and its cytosolic localization under conditions of serum deprivation. Mol Cell Biol *19*, 6323-6332. 10.1128/MCB.19.9.6323.

Kogel, A., Keidel, A., Bonneau, F., Schafer, I.B., and Conti, E. (2022). The human SKI complex regulates channeling of ribosome-bound RNA to the exosome via an intrinsic gatekeeping mechanism. Mol Cell *82*, 756-769 e758. 10.1016/j.molcel.2022.01.009.

Kolosov, P., Frolova, L., Seit-Nebi, A., Dubovaya, V., Kononenko, A., Oparina, N., Justesen, J., Efimov, A., and Kisselev, L. (2005). Invariant amino acids essential for decoding function of polypeptide release factor eRF1. Nucleic Acids Res *33*, 6418-6425. 10.1093/nar/gki927.

Kozak, M. (1986). Point mutations define a sequence flanking the AUG initiator codon that modulates translation by eukaryotic ribosomes. Cell *44*, 283-292. 10.1016/0092-8674(86)90762-2.

Kratzat, H., Mackens-Kiani, T., Ameismeier, M., Potocnjak, M., Cheng, J., Dacheux, E., Namane, A., Berninghausen, O., Herzog, F., Fromont-Racine, M., *et al*. (2021). A structural inventory of native ribosomal ABCE1-43S pre-initiation complexes. EMBO J *40*, e105179. 10.15252/embj.2020105179.

Kucukelbir, A., Sigworth, F.J., and Tagare, H.D. (2014). Quantifying the local resolution of cryo-EM density maps. Nat Methods *11*, 63-65. 10.1038/nmeth.2727.

Kulak, N.A., Pichler, G., Paron, I., Nagaraj, N., and Mann, M. (2014). Minimal, encapsulated proteomic-sample processing applied to copy-number estimation in eukaryotic cells. Nat Methods *11*, 319-324. 10.1038/nmeth.2834.

Laemmli, U.K. (1970). Cleavage of structural proteins during the assembly of the head of bacteriophage T4. Nature *227*, 680-685. 10.1038/227680a0.

Lagerkvist, U. (1978). "Two out of three": an alternative method for codon reading. Proc Natl Acad Sci U S A *75*, 1759-1762. 10.1073/pnas.75.4.1759.

Lareau, L.F., Hite, D.H., Hogan, G.J., and Brown, P.O. (2014). Distinct stages of the translation elongation cycle revealed by sequencing ribosome-protected mRNA fragments. Elife *3*, e01257. 10.7554/eLife.01257.

Letzring, D.P., Dean, K.M., and Grayhack, E.J. (2010). Control of translation efficiency in yeast by codon-anticodon interactions. RNA *16*, 2516-2528. 10.1261/rna.2411710.

Letzring, D.P., Wolf, A.S., Brule, C.E., and Grayhack, E.J. (2013). Translation of CGA codon repeats in yeast involves quality control components and ribosomal protein L1. RNA *19*, 1208-1217. 10.1261/rna.039446.113.

Li, F.Q., Ueda, H., and Hirose, S. (1994). Mediators of activation of fushi tarazu gene transcription by BmFTZ-F1. Mol Cell Biol *14*, 3013-3021. 10.1128/mcb.14.5.3013-3021.1994.

Li, S., Ikeuchi, K., Kato, M., Buschauer, R., Sugiyama, T., Adachi, S., Kusano, H., Natsume, T., Berninghausen, O., Matsuo, Y., *et al*. (2022). Sensing of individual stalled 80S ribosomes by Fap1 for nonfunctional rRNA turnover. Mol Cell *82*, 3424-3437 e3428. 10.1016/j.molcel.2022.08.018.

Li, X., Mooney, P., Zheng, S., Booth, C.R., Braunfeld, M.B., Gubbens, S., Agard, D.A., and Cheng, Y. (2013a). Electron counting and beam-induced motion correction enable near-atomic-resolution single-particle cryo-EM. Nat Methods *10*, 584-590. 10.1038/nmeth.2472.

Li, X., Zheng, S.Q., Egami, K., Agard, D.A., and Cheng, Y. (2013b). Influence of electron dose rate on electron counting images recorded with the K2 camera. Journal of structural biology *184*, 251-260.

Liao, H.Y., and Frank, J. (2010). Definition and estimation of resolution in single-particle reconstructions. Structure *18*, 768-775. 10.1016/j.str.2010.05.008.

Liaud, N., Horlbeck, M.A., Gilbert, L.A., Gjoni, K., Weissman, J.S., and Cate, J.H.D. (2019). Cellular response to small molecules that selectively stall protein synthesis by the ribosome. PLoS Genet *15*, e1008057. 10.1371/journal.pgen.1008057.

Linder, P., and Jankowsky, E. (2011). From unwinding to clamping - the DEAD box RNA helicase family. Nat Rev Mol Cell Biol *12*, 505-516. 10.1038/nrm3154.

Llacer, J.L., Hussain, T., Marler, L., Aitken, C.E., Thakur, A., Lorsch, J.R., Hinnebusch, A.G., and Ramakrishnan, V. (2015). Conformational Differences between Open and Closed States of the Eukaryotic Translation Initiation Complex. Mol Cell *59*, 399-412. 10.1016/j.molcel.2015.06.033.

Loveland, A.B., Demo, G., Grigorieff, N., and Korostelev, A.A. (2017). Ensemble cryo-EM elucidates the mechanism of translation fidelity. Nature *546*, 113-117. 10.1038/nature22397.

Lu, J.R., Su, T.J., and Thomas, R.K. (1999). Structural Conformation of Bovine Serum Albumin Layers at the Air-Water Interface Studied by Neutron Reflection. J Colloid Interface Sci *213*, 426-437. 10.1006/jcis.1999.6157.

Mandon, E.C., Trueman, S.F., and Gilmore, R. (2013). Protein translocation across the rough endoplasmic reticulum. Cold Spring Harb Perspect Biol *5*. 10.1101/cshperspect.a013342.

Marrero Coto, J., Ehrenhofer-Murray, A.E., Pons, T., and Siebers, B. (2011). Functional analysis of archaeal MBF1 by complementation studies in yeast. Biol Direct *6*, 18. 10.1186/1745-6150-6-18.

Marton, L. (1934). Electron Microscopy of Biological Objects. Nature *133*, 911. https://doi.org/10.1038/133911b0.

Matheisl, S., Berninghausen, O., Becker, T., and Beckmann, R. (2015). Structure of a human translation termination complex. Nucleic Acids Res *43*, 8615-8626. 10.1093/nar/gkv909.

Matsuo, Y., Ikeuchi, K., Saeki, Y., Iwasaki, S., Schmidt, C., Udagawa, T., Sato, F., Tsuchiya, H., Becker, T., Tanaka, K., *et al*. (2017). Ubiquitination of stalled ribosome triggers ribosome-associated quality control. Nat Commun *8*, 159. 10.1038/s41467-017-00188-1.

Matsuo, Y., Tesina, P., Nakajima, S., Mizuno, M., Endo, A., Buschauer, R., Cheng, J., Shounai, O., Ikeuchi, K., Saeki, Y., *et al*. (2020). RQT complex dissociates ribosomes collided on endogenous RQC substrate SDD1. Nat Struct Mol Biol *27*, 323-332. 10.1038/s41594-020-0393-9.

Matsuo, Y., Uchihashi, T., and Inada, T. (2022). Decoding of the ubiquitin code for clearance of colliding ribosomes by the RQT complex. bioRxiv, 2022.2009.2012.507701. 10.1101/2022.09.12.507701.

McCaughan, K.K., Brown, C.M., Dalphin, M.E., Berry, M.J., and Tate, W.P. (1995). Translational termination efficiency in mammals is influenced by the base following the stop codon. Proc Natl Acad Sci U S A *92*, 5431-5435. 10.1073/pnas.92.12.5431.

McMullan, G., Chen, S., Henderson, R., and Faruqi, A.R. (2009). Detective quantum efficiency of electron area detectors in electron microscopy. Ultramicroscopy *109*, 1126-1143. 10.1016/j.ultramic.2009.04.002.

Melnikov, S., Ben-Shem, A., Garreau de Loubresse, N., Jenner, L., Yusupova, G., and Yusupov, M. (2012). One core, two shells: bacterial and eukaryotic ribosomes. Nat Struct Mol Biol *19*, 560-567. 10.1038/nsmb.2313.

Merrick, W.C. (2015). eIF4F: a retrospective. J Biol Chem *290*, 24091-24099. 10.1074/jbc.R115.675280.

Meydan, S., and Guydosh, N.R. (2020). Disome and Trisome Profiling Reveal Genome-wide Targets of Ribosome Quality Control. Mol Cell *79*, 588-602 e586. 10.1016/j.molcel.2020.06.010.

Milazzo, A.C., Cheng, A., Moeller, A., Lyumkis, D., Jacovetty, E., Polukas, J., Ellisman, M.H., Xuong, N.H., Carragher, B., and Potter, C.S. (2011). Initial evaluation of a direct detection device detector for single particle cryo-electron microscopy. J Struct Biol *176*, 404-408. 10.1016/j.jsb.2011.09.002.

Milazzo, A.C., Leblanc, P., Duttweiler, F., Jin, L., Bouwer, J.C., Peltier, S., Ellisman, M., Bieser, F., Matis, H.S., Wieman, H., *et al*. (2005). Active pixel sensor array as a detector for electron microscopy. Ultramicroscopy *104*, 152-159. 10.1016/j.ultramic.2005.03.006.

Mindell, J.A., and Grigorieff, N. (2003). Accurate determination of local defocus and specimen tilt in electron microscopy. J Struct Biol *142*, 334-347. 10.1016/s1047-8477(03)00069-8.

Miotto, B., and Struhl, K. (2006). Differential gene regulation by selective association of transcriptional coactivators and bZIP DNA-binding domains. Mol Cell Biol *26*, 5969-5982. 10.1128/MCB.00696-06.

Miyazawa, N., Yoshikawa, H., Magae, S., Ishikawa, H., Izumikawa, K., Terukina, G., Suzuki, A., Nakamura-Fujiyama, S., Miura, Y., Hayano, T., *et al*. (2014). Human cell growth regulator Ly-1 antibody reactive homologue accelerates processing of preribosomal RNA. Genes Cells *19*, 273-286. 10.1111/gtc.12129.

Moazed, D., and Noller, H.F. (1989). Intermediate states in the movement of transfer RNA in the ribosome. Nature *342*, 142-148. 10.1038/342142a0.

Moore, S.D., and Sauer, R.T. (2007). The tmRNA system for translational surveillance and ribosome rescue. Annu Rev Biochem *76*, 101-124. 10.1146/annurev.biochem.75.103004.142733.

Morita, M., Ler, L.W., Fabian, M.R., Siddiqui, N., Mullin, M., Henderson, V.C., Alain, T., Fonseca, B.D., Karashchuk, G., Bennett, C.F., *et al*. (2012). A novel 4EHP-GIGYF2 translational repressor complex is essential for mammalian development. Mol Cell Biol *32*, 3585-3593. 10.1128/MCB.00455-12.

Moriya, T., Saur, M., Stabrin, M., Merino, F., Voicu, H., Huang, Z., Penczek, P.A., Raunser, S., and Gatsogiannis, C. (2017). High-resolution Single Particle Analysis from Electron Cryo-microscopy Images Using SPHIRE. J Vis Exp. 10.3791/55448.

Muller, C., Crowe-McAuliffe, C., and Wilson, D.N. (2021). Ribosome Rescue Pathways in Bacteria. Front Microbiol *12*, 652980. 10.3389/fmicb.2021.652980.

Nakane, T., and Scheres, S.H.W. (2021). Multi-body Refinement of Cryo-EM Images in RELION. Methods Mol Biol *2215*, 145-160. 10.1007/978-1-0716-0966-8_7.

Narita, M., Denk, T., Matsuo, Y., Sugiyama, T., Kikuguchi, C., Ito, S., Sato, N., Suzuki, T., Hashimoto, S., Machova, I., *et al*. (2022). A distinct mammalian disome collision interface harbors K63-linked polyubiquitination of uS10 to trigger hRQT-mediated subunit dissociation. Nat Commun *13*, 6411. 10.1038/s41467-022-34097-9.

Nedialkova, D.D., and Leidel, S.A. (2015). Optimization of Codon Translation Rates via tRNA Modifications Maintains Proteome Integrity. Cell *161*, 1606-1618. 10.1016/j.cell.2015.05.022.

Nirenberg, M. (2004). Historical review: Deciphering the genetic code--a personal account. Trends Biochem Sci *29*, 46-54. 10.1016/j.tibs.2003.11.009.

Nissen, P., Hansen, J., Ban, N., Moore, P.B., and Steitz, T.A. (2000). The structural basis of ribosome activity in peptide bond synthesis. Science *289*, 920-930. 10.1126/science.289.5481.920.

Nurenberg-Goloub, E., Kratzat, H., Heinemann, H., Heuer, A., Kotter, P., Berninghausen, O., Becker, T., Tampe, R., and Beckmann, R. (2020). Molecular analysis of the ribosome recycling factor ABCE1 bound to the 30S post-splitting complex. EMBO J *39*, e103788. 10.15252/embj.2019103788.

Ogle, J.M., Brodersen, D.E., Clemons, W.M., Jr., Tarry, M.J., Carter, A.P., and Ramakrishnan, V. (2001). Recognition of cognate transfer RNA by the 30S ribosomal subunit. Science *292*, 897-902. 10.1126/science.1060612.

Ohi, M., Li, Y., Cheng, Y., and Walz, T. (2004). Negative Staining and Image Classification - Powerful Tools in Modern Electron Microscopy. Biol Proced Online *6*, 23-34. 10.1251/bpo70.

Orlova, E.V., and Saibil, H.R. (2011). Structural analysis of macromolecular assemblies by electron microscopy. Chem Rev *111*, 7710-7748. 10.1021/cr100353t.

Panasenko, O.O., and Collart, M.A. (2012). Presence of Not5 and ubiquitinated Rps7A in polysome fractions depends upon the Not4 E3 ligase. Mol Microbiol *83*, 640-653. 10.1111/j.1365-2958.2011.07957.x.

Pantelic, R.S., Meyer, J.C., Kaiser, U., and Stahlberg, H. (2021). The application of graphene as a sample support in transmission electron microscopy. Solid State Communications *152*, 1375-1382. https://doi.org/10.1016/j.ssc.2012.04.038.

Park, H., and Subramaniam, A.R. (2019). Inverted translational control of eukaryotic gene expression by ribosome collisions. PLoS Biol *17*, e3000396. 10.1371/journal.pbio.3000396.

Pedersen, W.T., and Curran, J.F. (1991). Effects of the nucleotide 3' to an amber codon on ribosomal selection rates of suppressor tRNA and release factor-1. J Mol Biol *219*, 231-241. 10.1016/0022-2836(91)90564-m.

Penczek, P.A. (2010a). Image restoration in cryo-electron microscopy. Methods Enzymol *482*, 35-72. 10.1016/S0076-6879(10)82002-6.

Penczek, P.A. (2010b). Resolution measures in molecular electron microscopy. Methods Enzymol *482*, 73-100. 10.1016/S0076-6879(10)82003-8.

Pintilie, G., Zhang, K., Su, Z., Li, S., Schmid, M.F., and Chiu, W. (2020). Measurement of atom resolvability in cryo-EM maps with Q-scores. Nat Methods *17*, 328-334. 10.1038/s41592-020-0731-1.

Pisarev, A.V., Skabkin, M.A., Pisareva, V.P., Skabkina, O.V., Rakotondrafara, A.M., Hentze, M.W., Hellen, C.U., and Pestova, T.V. (2010). The role of ABCE1 in eukaryotic posttermination ribosomal recycling. Mol Cell *37*, 196-210. 10.1016/j.molcel.2009.12.034.

Pisareva, V.P., Skabkin, M.A., Hellen, C.U., Pestova, T.V., and Pisarev, A.V. (2011). Dissociation by Pelota, Hbs1 and ABCE1 of mammalian vacant 80S ribosomes and stalled elongation complexes. EMBO J *30*, 1804-1817. 10.1038/emboj.2011.93.

Plumb, R., Zhang, Z.R., Appathurai, S., and Mariappan, M. (2015). A functional link between the co-translational protein translocation pathway and the UPR. Elife *4*. 10.7554/eLife.07426.

Pochopien, A.A., Beckert, B., Kasvandik, S., Berninghausen, O., Beckmann, R., Tenson, T., and Wilson, D.N. (2021). Structure of Gcn1 bound to stalled and colliding 80S ribosomes. Proc Natl Acad Sci U S A *118*. 10.1073/pnas.2022756118.

Ponting, C.P. (2000). Proteins of the endoplasmic-reticulum-associated degradation pathway: domain detection and function prediction. Biochem J *351 Pt 2*, 527-535.

Preis, A., Heuer, A., Barrio-Garcia, C., Hauser, A., Eyler, D.E., Berninghausen, O., Green, R., Becker, T., and Beckmann, R. (2014). Cryoelectron microscopic structures of eukaryotic translation termination complexes containing eRF1-eRF3 or eRF1-ABCE1. Cell Rep *8*, 59-65. 10.1016/j.celrep.2014.04.058.

Punjani, A., and Fleet, D.J. (2021). 3D variability analysis: Resolving continuous flexibility and discrete heterogeneity from single particle cryo-EM. J Struct Biol *213*, 107702. 10.1016/j.jsb.2021.107702.

Punjani, A., Rubinstein, J.L., Fleet, D.J., and Brubaker, M.A. (2017). cryoSPARC: algorithms for rapid unsupervised cryo-EM structure determination. Nat Methods *14*, 290-296. 10.1038/nmeth.4169.

Ranjan, N., Pochopien, A.A., Chih-Chien Wu, C., Beckert, B., Blanchet, S., Green, R., M, V.R., and Wilson, D.N. (2021). Yeast translation elongation factor eEF3 promotes late stages of tRNA translocation. EMBO J *40*, e106449. 10.15252/embj.2020106449.

Razinkov, I., Dandey, V., Wei, H., Zhang, Z., Melnekoff, D., Rice, W.J., Wigge, C., Potter, C.S., and Carragher, B. (2016). A new method for vitrifying samples for cryoEM. J Struct Biol *195*, 190-198. 10.1016/j.jsb.2016.06.001.

Rheinberger, H.J., Sternbach, H., and Nierhaus, K.H. (1981). Three tRNA binding sites on Escherichia coli ribosomes. Proc Natl Acad Sci U S A *78*, 5310-5314. 10.1073/pnas.78.9.5310.

Rima, L., Zimmermann, M., Frankl, A., Clairfeuille, T., Lauer, M., Engel, A., Engel, H.A., and Braun, T. (2022). cryoWriter: a blotting free cryo-EM preparation system with a climate jet and cover-slip injector. Faraday Discuss *240*, 55-66. 10.1039/d2fd00066k.

Rohou, A., and Grigorieff, N. (2015). CTFFIND4: Fast and accurate defocus estimation from electron micrographs. J Struct Biol *192*, 216-221. 10.1016/j.jsb.2015.08.008.

Rosenthal, P.B., and Henderson, R. (2003). Optimal determination of particle orientation, absolute hand, and contrast loss in single-particle electron cryomicroscopy. J Mol Biol *333*, 721-745. 10.1016/j.jmb.2003.07.013.

Rosenthal, P.B., and Rubinstein, J.L. (2015). Validating maps from single particle electron cryomicroscopy. Curr Opin Struct Biol *34*, 135-144. 10.1016/j.sbi.2015.07.002.

Ruskin, R.S., Yu, Z., and Grigorieff, N. (2013). Quantitative characterization of electron detectors for transmission electron microscopy. Journal of structural biology *184*, 385-393.

Russo, C.J., and Passmore, L.A. (2014). Electron microscopy: Ultrastable gold substrates for electron cryomicroscopy. Science *346*, 1377-1380. 10.1126/science.1259530.

Saini, P., Eyler, D.E., Green, R., and Dever, T.E. (2009). Hypusine-containing protein eIF5A promotes translation elongation. Nature *459*, 118-121. 10.1038/nature08034.

Saito, K., Kratzat, H., Campbell, A., Buschauer, R., Burroughs, A.M., Berninghausen, O., Aravind, L., Green, R., Beckmann, R., and Buskirk, A.R. (2022). Ribosome collisions induce mRNA cleavage and ribosome rescue in bacteria. Nature *603*, 503-508. 10.1038/s41586-022-04416-7.

Sakata, T., Fujii, K., Ohno, M., and Kitabatake, M. (2015). Crt10 directs the cullin-E3 ligase Rtt101 to nonfunctional 25S rRNA decay. Biochem Biophys Res Commun *457*, 90-94. 10.1016/j.bbrc.2014.12.072.

Santos, K.F., Jovin, S.M., Weber, G., Pena, V., Luhrmann, R., and Wahl, M.C. (2012). Structural basis for functional cooperation between tandem helicase cassettes in Brr2-mediated remodeling of the spliceosome. Proc Natl Acad Sci U S A *109*, 17418-17423. 10.1073/pnas.1208098109.

Scheffner, M., Nuber, U., and Huibregtse, J.M. (1995). Protein ubiquitination involving an E1-E2-E3 enzyme ubiquitin thioester cascade. Nature *373*, 81-83. 10.1038/373081a0.

Scheres, S.H. (2012a). A Bayesian view on cryo-EM structure determination. J Mol Biol *415*, 406-418. 10.1016/j.jmb.2011.11.010.

Scheres, S.H. (2012b). RELION: implementation of a Bayesian approach to cryo-EM structure determination. J Struct Biol *180*, 519-530. 10.1016/j.jsb.2012.09.006.

Scheres, S.H. (2014). Beam-induced motion correction for sub-megadalton cryo-EM particles. Elife *3*, e03665. 10.7554/eLife.03665.

Scheres, S.H., and Chen, S. (2012). Prevention of overfitting in cryo-EM structure determination. Nat Methods *9*, 853-854. 10.1038/nmeth.2115.

Schluenzen, F., Tocilj, A., Zarivach, R., Harms, J., Gluehmann, M., Janell, D., Bashan, A., Bartels, H., Agmon, I., Franceschi, F., and Yonath, A. (2000). Structure of functionally activated small ribosomal subunit at 3.3 angstroms resolution. Cell *102*, 615-623. 10.1016/s0092-8674(00)00084-2.

Schmidt, C., Becker, T., Heuer, A., Braunger, K., Shanmuganathan, V., Pech, M., Berninghausen, O., Wilson, D.N., and Beckmann, R. (2016a). Structure of the hypusinylated eukaryotic translation factor eIF-5A bound to the ribosome. Nucleic Acids Res *44*, 1944-1951. 10.1093/nar/gkv1517.

Schmidt, C., Kowalinski, E., Shanmuganathan, V., Defenouillere, Q., Braunger, K., Heuer, A., Pech, M., Namane, A., Berninghausen, O., Fromont-Racine, M., *et al*. (2016b). The cryo-EM structure of a ribosome-Ski2-Ski3-Ski8 helicase complex. Science *354*, 1431-1433. 10.1126/science.aaf7520.

Schuller, A.P., Wu, C.C., Dever, T.E., Buskirk, A.R., and Green, R. (2017). eIF5A Functions Globally in Translation Elongation and Termination. Mol Cell *66*, 194-205 e195. 10.1016/j.molcel.2017.03.003.

Searfoss, A.M., and Wickner, R.B. (2000). 3' poly(A) is dispensable for translation. Proc Natl Acad Sci U S A *97*, 9133-9137. 10.1073/pnas.97.16.9133.

Seit-Nebi, A., Frolova, L., Justesen, J., and Kisselev, L. (2001). Class-1 translation termination factors: invariant GGQ minidomain is essential for release activity and ribosome binding but not for stop codon recognition. Nucleic Acids Res *29*, 3982-3987. 10.1093/nar/29.19.3982.

Shanmuganathan, V., Schiller, N., Magoulopoulou, A., Cheng, J., Braunger, K., Cymer, F., Berninghausen, O., Beatrix, B., Kohno, K., von Heijne, G., and Beckmann, R. (2019). Structural and mutational analysis of the ribosome-arresting human XBP1u. Elife *8*. 10.7554/eLife.46267.

Shao, S., Brown, A., Santhanam, B., and Hegde, R.S. (2015). Structure and assembly pathway of the ribosome quality control complex. Mol Cell *57*, 433-444. 10.1016/j.molcel.2014.12.015.

Shao, S., Murray, J., Brown, A., Taunton, J., Ramakrishnan, V., and Hegde, R.S. (2016). Decoding Mammalian Ribosome-mRNA States by Translational GTPase Complexes. Cell *167*, 1229-1240 e1215. 10.1016/j.cell.2016.10.046.

Shao, S., von der Malsburg, K., and Hegde, R.S. (2013). Listerin-dependent nascent protein ubiquitination relies on ribosome subunit dissociation. Mol Cell *50*, 637-648. 10.1016/j.molcel.2013.04.015.

Shen, P.S., Park, J., Qin, Y., Li, X., Parsawar, K., Larson, M.H., Cox, J., Cheng, Y., Lambowitz, A.M., Weissman, J.S., *et al*. (2015). Protein synthesis. Rqc2p and 60S ribosomal subunits mediate mRNA-independent elongation of nascent chains. Science *347*, 75-78. 10.1126/science.1259724.

Shigematsu, H., and Sigworth, F.J. (2013). Noise models and cryo-EM drift correction with a direct-electron camera. Ultramicroscopy *131*, 61-69. 10.1016/j.ultramic.2013.04.001.

Shoemaker, C.J., Eyler, D.E., and Green, R. (2010). Dom34:Hbs1 promotes subunit dissociation and peptidyl-tRNA drop-off to initiate no-go decay. Science *330*, 369-372. 10.1126/science.1192430.

Shoemaker, C.J., and Green, R. (2011). Kinetic analysis reveals the ordered coupling of translation termination and ribosome recycling in yeast. Proc Natl Acad Sci U S A *108*, E1392-1398. 10.1073/pnas.1113956108.

Shoemaker, C.J., and Green, R. (2012). Translation drives mRNA quality control. Nat Struct Mol Biol *19*, 594-601. 10.1038/nsmb.2301.

Sigworth, F.J. (2016). Principles of cryo-EM single-particle image processing. Microscopy (Oxf) *65*, 57-67. 10.1093/jmicro/dfv370.

Simms, C.L., Kim, K.Q., Yan, L.L., Qiu, J., and Zaher, H.S. (2018). Interactions between the mRNA and Rps3/uS3 at the entry tunnel of the ribosomal small subunit are important for no-go decay. PLoS Genet *14*, e1007818. 10.1371/journal.pgen.1007818.

Simms, C.L., Yan, L.L., Qiu, J.K., and Zaher, H.S. (2019). Ribosome Collisions Result in +1 Frameshifting in the Absence of No-Go Decay. Cell Rep *28*, 1679-1689 e1674. 10.1016/j.celrep.2019.07.046.

Simms, C.L., Yan, L.L., and Zaher, H.S. (2017). Ribosome Collision Is Critical for Quality Control during No-Go Decay. Mol Cell *68*, 361-373 e365. 10.1016/j.molcel.2017.08.019.

Singleton, M.R., Dillingham, M.S., and Wigley, D.B. (2007). Structure and mechanism of helicases and nucleic acid translocases. Annu Rev Biochem *76*, 23-50. 10.1146/annurev.biochem.76.052305.115300.

Sinha, N.K., Ordureau, A., Best, K., Saba, J.A., Zinshteyn, B., Sundaramoorthy, E., Fulzele, A., Garshott, D.M., Denk, T., Thoms, M., *et al*. (2020). EDF1 coordinates cellular responses to ribosome collisions. Elife *9*. 10.7554/eLife.58828.

Sitron, C.S., Park, J.H., and Brandman, O. (2017). Asc1, Hel2, and Slh1 couple translation arrest to nascent chain degradation. RNA *23*, 798-810. 10.1261/rna.060897.117.

Sorensen, M.A., and Pedersen, S. (1991). Absolute in vivo translation rates of individual codons in Escherichia coli. The two glutamic acid codons GAA and GAG are translated with a threefold difference in rate. J Mol Biol *222*, 265-280. 10.1016/0022-2836(91)90211-n.

Spahn, C.M., Beckmann, R., Eswar, N., Penczek, P.A., Sali, A., Blobel, G., and Frank, J. (2001). Structure of the 80S ribosome from Saccharomyces cerevisiae--tRNA-ribosome and subunit-subunit interactions. Cell *107*, 373-386. 10.1016/s0092-8674(01)00539-6.

Stadler, M., and Fire, A. (2011). Wobble base-pairing slows in vivo translation elongation in metazoans. RNA *17*, 2063-2073. 10.1261/rna.02890211.

Steiger, M., Carr-Schmid, A., Schwartz, D.C., Kiledjian, M., and Parker, R. (2003). Analysis of recombinant yeast decapping enzyme. RNA *9*, 231-238. 10.1261/rna.2151403.

Stoneley, M., Harvey, R.F., Mulroney, T.E., Mordue, R., Jukes-Jones, R., Cain, K., Lilley, K.S., Sawarkar, R., and Willis, A.E. (2022). Unresolved stalled ribosome complexes restrict cell-cycle progression after genotoxic stress. Mol Cell *82*, 1557-1572 e1557. 10.1016/j.molcel.2022.01.019.

Su, T., Izawa, T., Thoms, M., Yamashita, Y., Cheng, J., Berninghausen, O., Hartl, F.U., Inada, T., Neupert, W., and Beckmann, R. (2019). Structure and function of Vms1 and Arb1 in RQC and mitochondrial proteome homeostasis. Nature *570*, 538-542. 10.1038/s41586-019-1307-z.

Sugiyama, T., Li, S., Kato, M., Ikeuchi, K., Ichimura, A., Matsuo, Y., and Inada, T. (2019). Sequential Ubiquitination of Ribosomal Protein uS3 Triggers the Degradation of Non-functional 18S rRNA. Cell Rep *26*, 3400-3415 e3407. 10.1016/j.celrep.2019.02.067.

Sundaramoorthy, E., Leonard, M., Mak, R., Liao, J., Fulzele, A., and Bennett, E.J. (2017). ZNF598 and RACK1 Regulate Mammalian Ribosome-Associated Quality Control Function by Mediating Regulatory 40S Ribosomal Ubiquitylation. Mol Cell *65*, 751-760 e754. 10.1016/j.molcel.2016.12.026.

Takemaru, K., Harashima, S., Ueda, H., and Hirose, S. (1998). Yeast coactivator MBF1 mediates GCN4-dependent transcriptional activation. Mol Cell Biol *18*, 4971-4976. 10.1128/MCB.18.9.4971.

Takemaru, K., Li, F.Q., Ueda, H., and Hirose, S. (1997). Multiprotein bridging factor 1 (MBF1) is an evolutionarily conserved transcriptional coactivator that connects a regulatory factor and TATA element-binding protein. Proc Natl Acad Sci U S A *94*, 7251-7256. 10.1073/pnas.94.14.7251.

Tan, Y.Z., Baldwin, P.R., Davis, J.H., Williamson, J.R., Potter, C.S., Carragher, B., and Lyumkis, D. (2017). Addressing preferred specimen orientation in single-particle cryo-EM through tilting. Nat Methods *14*, 793-796. 10.1038/nmeth.4347.

Tesina, P., Heckel, E., Cheng, J., Fromont-Racine, M., Buschauer, R., Kater, L., Beatrix, B., Berninghausen, O., Jacquier, A., Becker, T., and Beckmann, R. (2019). Structure of the 80S ribosome-Xrn1 nuclease complex. Nat Struct Mol Biol *26*, 275-280. 10.1038/s41594-019-0202-5.

Tesina, P., Lessen, L.N., Buschauer, R., Cheng, J., Wu, C.C., Berninghausen, O., Buskirk, A.R., Becker, T., Beckmann, R., and Green, R. (2020). Molecular mechanism of translational stalling by inhibitory codon combinations and poly(A) tracts. EMBO J *39*, e103365. 10.15252/embj.2019103365.

Thoms, M., Buschauer, R., Ameismeier, M., Koepke, L., Denk, T., Hirschenberger, M., Kratzat, H., Hayn, M., Mackens-Kiani, T., Cheng, J., *et al*. (2020). Structural basis for translational shutdown and immune evasion by the Nsp1 protein of SARS-CoV-2. Science *369*, 1249-1255. 10.1126/science.abc8665.

Thon, F. (1966). Notizen: Zur Defokussierungsabhängigkeit des Phasenkontrastes bei der elektronenmikroskopischen Abbildung. Zeitschrift für Naturforschung A *21*, 476-478. doi:10.1515/zna-1966-0417.

Tkach, J.M., Yimit, A., Lee, A.Y., Riffle, M., Costanzo, M., Jaschob, D., Hendry, J.A., Ou, J., Moffat, J., Boone, C., *et al*. (2012). Dissecting DNA damage response pathways by analysing protein localization and abundance changes during DNA replication stress. Nat Cell Biol *14*, 966-976. 10.1038/ncb2549.

Tocilj, A., Schlunzen, F., Janell, D., Gluhmann, M., Hansen, H.A., Harms, J., Bashan, A., Bartels, H., Agmon, I., Franceschi, F., and Yonath, A. (1999). The small ribosomal subunit from Thermus thermophilus at 4.5 A resolution: pattern fittings and the identification of a functional site. Proc Natl Acad Sci U S A *96*, 14252-14257. 10.1073/pnas.96.25.14252.

Tollenaere, M.A.X., Tiedje, C., Rasmussen, S., Nielsen, J.C., Vind, A.C., Blasius, M., Batth, T.S., Mailand, N., Olsen, J.V., Gaestel, M., and Bekker-Jensen, S. (2019). GIGYF1/2-Driven Cooperation between ZNF598 and TTP in Posttranscriptional Regulation of Inflammatory Signaling. Cell Rep *26*, 3511-3521 e3514. 10.1016/j.celrep.2019.03.006.

Trainor, B.M., Komar, A.A., Pestov, D.G., and Shcherbik, N. (2021). Cell-free Translation: Preparation and Validation of Translation-competent Extracts from Saccharomyces cerevisiae. Bio Protoc *11*, e4093. 10.21769/BioProtoc.4093.

Tsuboi, T., Kuroha, K., Kudo, K., Makino, S., Inoue, E., Kashima, I., and Inada, T. (2012). Dom34:hbs1 plays a general role in quality-control systems by dissociation of a stalled ribosome at the 3' end of aberrant mRNA. Mol Cell *46*, 518-529. 10.1016/j.molcel.2012.03.013.

Tucker, M., Valencia-Sanchez, M.A., Staples, R.R., Chen, J., Denis, C.L., and Parker, R. (2001). The transcription factor associated Ccr4 and Caf1 proteins are components of the major cytoplasmic mRNA deadenylase in Saccharomyces cerevisiae. Cell *104*, 377-386. 10.1016/s0092-8674(01)00225-2.

Tzamarias, D., Roussou, I., and Thireos, G. (1989). Coupling of GCN4 mRNA translational activation with decreased rates of polypeptide chain initiation. Cell *57*, 947-954. 10.1016/0092-8674(89)90333-4.

van den Elzen, A.M., Schuller, A., Green, R., and Seraphin, B. (2014). Dom34-Hbs1 mediated dissociation of inactive 80S ribosomes promotes restart of translation after stress. EMBO J *33*, 265-276. 10.1002/embj.201386123.

van Dijk, E., Cougot, N., Meyer, S., Babajko, S., Wahle, E., and Seraphin, B. (2002). Human Dcp2: a catalytically active mRNA decapping enzyme located in specific cytoplasmic structures. EMBO J *21*, 6915-6924. 10.1093/emboj/cdf678.

Varadi, M., Anyango, S., Deshpande, M., Nair, S., Natassia, C., Yordanova, G., Yuan, D., Stroe, O., Wood, G., Laydon, A., *et al*. (2022). AlphaFold Protein Structure Database: massively expanding the structural coverage of protein-sequence space with high-accuracy models. Nucleic Acids Res *50*, D439-D444. 10.1093/nar/gkab1061.

Verma, R., Reichermeier, K.M., Burroughs, A.M., Oania, R.S., Reitsma, J.M., Aravind, L., and Deshaies, R.J. (2018). Vms1 and ANKZF1 peptidyl-tRNA hydrolases release nascent chains from stalled ribosomes. Nature *557*, 446-451. 10.1038/s41586-018-0022-5.

Voss, N.R., Gerstein, M., Steitz, T.A., and Moore, P.B. (2006). The geometry of the ribosomal polypeptide exit tunnel. J Mol Biol *360*, 893-906. 10.1016/j.jmb.2006.05.023.

Wade, R.H. (1992). A brief look at imaging and contrast transfer. Ultramicroscopy *46*, 145-156.

Wagner, T., Merino, F., Stabrin, M., Moriya, T., Antoni, C., Apelbaum, A., Hagel, P., Sitsel, O., Raisch, T., Prumbaum, D., *et al*. (2019). SPHIRE-crYOLO is a fast and accurate fully automated particle picker for cryo-EM. Commun Biol *2*, 218. 10.1038/s42003-019-0437-z.

Walker, J.E., Saraste, M., Runswick, M.J., and Gay, N.J. (1982). Distantly related sequences in the alpha- and beta-subunits of ATP synthase, myosin, kinases and other ATP-requiring enzymes and a common nucleotide binding fold. EMBO J *1*, 945-951. 10.1002/j.1460-2075.1982.tb01276.x.

Wang, J., Zhou, J., Yang, Q., and Grayhack, E.J. (2018). Multi-protein bridging factor 1(Mbf1), Rps3 and Asc1 prevent stalled ribosomes from frameshifting. Elife *7*. 10.7554/eLife.39637.

Wang, Z., Fang, P., and Sachs, M.S. (1998). The evolutionarily conserved eukaryotic arginine attenuator peptide regulates the movement of ribosomes that have translated it. Mol Cell Biol *18*, 7528-7536. 10.1128/MCB.18.12.7528.

Waters, M.G., and Blobel, G. (1986). Secretory protein translocation in a yeast cell-free system can occur posttranslationally and requires ATP hydrolysis. J Cell Biol *102*, 1543-1550. 10.1083/jcb.102.5.1543.

Watson, Z.L., Ward, F.R., Meheust, R., Ad, O., Schepartz, A., Banfield, J.F., and Cate, J.H. (2020). Structure of the bacterial ribosome at 2 A resolution. Elife *9*. 10.7554/eLife.60482.

Weissenberger, G., Henderikx, R.J.M., and Peters, P.J. (2021). Understanding the invisible hands of sample preparation for cryo-EM. Nat Methods *18*, 463-471. 10.1038/s41592-021-01130-6.

Wells, J.N., Buschauer, R., Mackens-Kiani, T., Best, K., Kratzat, H., Berninghausen, O., Becker, T., Gilbert, W., Cheng, J., and Beckmann, R. (2020). Structure and function of yeast Lso2 and human CCDC124 bound to hibernating ribosomes. PLoS Biol *18*, e3000780. 10.1371/journal.pbio.3000780.

Wimberly, B.T., Brodersen, D.E., Clemons, W.M., Jr., Morgan-Warren, R.J., Carter, A.P., Vonrhein, C., Hartsch, T., and Ramakrishnan, V. (2000). Structure of the 30S ribosomal subunit. Nature *407*, 327-339. 10.1038/35030006.

Wolin, S.L., and Walter, P. (1988). Ribosome pausing and stacking during translation of a eukaryotic mRNA. EMBO J *7*, 3559-3569. 10.1002/j.1460-2075.1988.tb03233.x.

Wu, C.C., Peterson, A., Zinshteyn, B., Regot, S., and Green, R. (2020). Ribosome Collisions Trigger General Stress Responses to Regulate Cell Fate. Cell *182*, 404-416 e414. 10.1016/j.cell.2020.06.006.

Xiol, J., Spinelli, P., Laussmann, M.A., Homolka, D., Yang, Z., Cora, E., Coute, Y., Conn, S., Kadlec, J., Sachidanandam, R., *et al.* (2014). RNA clamping by Vasa assembles a piRNA amplifier complex on transposon transcripts. Cell *157*, 1698-1711. 10.1016/j.cell.2014.05.018.

Xue, X., Mutyam, V., Thakerar, A., Mobley, J., Bridges, R.J., Rowe, S.M., Keeling, K.M., and Bedwell, D.M. (2017). Identification of the amino acids inserted during suppression of CFTR nonsense mutations and determination of their functional consequences. Hum Mol Genet *26*, 3116-3129. 10.1093/hmg/ddx196.

Yang, C., Liu, X., Cheng, T., Xiao, R., Gao, Q., Ming, F., Jin, M., Chen, H., and Zhou, H. (2019). LYAR Suppresses Beta Interferon Induction by Targeting Phosphorylated Interferon Regulatory Factor 3. J Virol *93*. 10.1128/JVI.00769-19.

Yip, M.C.J., Keszei, A.F.A., Feng, Q., Chu, V., McKenna, M.J., and Shao, S. (2019). Mechanism for recycling tRNAs on stalled ribosomes. Nat Struct Mol Biol *26*, 343-349. 10.1038/s41594-019-0211-4.

Yoo, H.M., Kang, S.H., Kim, J.Y., Lee, J.E., Seong, M.W., Lee, S.W., Ka, S.H., Sou, Y.S., Komatsu, M., Tanaka, K., *et al.* (2014). Modification of ASC1 by UFM1 is crucial for ERalpha transactivation and breast cancer development. Mol Cell *56*, 261-274. 10.1016/j.molcel.2014.08.007.

Young, D.J., Makeeva, D.S., Zhang, F., Anisimova, A.S., Stolboushkina, E.A., Ghobakhlou, F., Shatsky, I.N., Dmitriev, S.E., Hinnebusch, A.G., and Guydosh, N.R. (2018). Tma64/eIF2D, Tma20/MCT-1, and Tma22/DENR Recycle Post-termination 40S Subunits In Vivo. Mol Cell *71*, 761-774 e765. 10.1016/j.molcel.2018.07.028.

Young, D.J., Meydan, S., and Guydosh, N.R. (2021). 40S ribosome profiling reveals distinct roles for Tma20/Tma22 (MCT-1/DENR) and Tma64 (eIF2D) in 40S subunit recycling. Nat Commun *12*, 2976. 10.1038/s41467-021-23223-8.

Yusupova, G.Z., Yusupov, M.M., Cate, J.H., and Noller, H.F. (2001). The path of messenger RNA through the ribosome. Cell *106*, 233-241. 10.1016/s0092-8674(01)00435-4.

Zeitler, E. (1992). The photographic emulsion as analog recorder for electrons. Ultramicroscopy *46*, 405-416. https://doi.org/10.1016/0304-3991(92)90027-H.

Zeng, F., Li, X., Pires-Alves, M., Chen, X., Hawk, C.W., and Jin, H. (2021). Conserved heterodimeric GTPase Rbg1/Tma46 promotes efficient translation in eukaryotic cells. Cell Rep *37*, 109877. 10.1016/j.celrep.2021.109877.

Zhang, K. (2016). Gctf: Real-time CTF determination and correction. J Struct Biol *193*, 1-12. 10.1016/j.jsb.2015.11.003.

Zheng, S.Q., Palovcak, E., Armache, J.P., Verba, K.A., Cheng, Y., and Agard, D.A. (2017). MotionCor2: anisotropic correction of beam-induced motion for improved cryo-electron microscopy. Nat Methods *14*, 331-332. 10.1038/nmeth.4193.

Zhong, E.D., Bepler, T., Berger, B., and Davis, J.H. (2021). CryoDRGN: reconstruction of heterogeneous cryo-EM structures using neural networks. Nature Methods *18*, 176-185. 10.1038/s41592-020-01049-4.

Zhu, J., Penczek, P.A., Schroder, R., and Frank, J. (1997). Three-dimensional reconstruction with contrast transfer function correction from energy-filtered cryoelectron micrographs: procedure and application to the 70S Escherichia coli ribosome. J Struct Biol *118*, 197-219. 10.1006/jsbi.1997.3845.

Zinoviev, A., Ayupov, R.K., Abaeva, I.S., Hellen, C.U.T., and Pestova, T.V. (2020). Extraction of mRNA from Stalled Ribosomes by the Ski Complex. Mol Cell *77*, 1340-1349 e1346. 10.1016/j.molcel.2020.01.011.

Zivanov, J., Nakane, T., Forsberg, B.O., Kimanius, D., Hagen, W.J., Lindahl, E., and Scheres, S.H. (2018). New tools for automated high-resolution cryo-EM structure determination in RELION-3. Elife *7*. 10.7554/eLife.42166.

Zivanov, J., Nakane, T., and Scheres, S.H.W. (2019). A Bayesian approach to beam-induced motion correction in cryo-EM single-particle analysis. IUCrJ *6*, 5-17. 10.1107/S205225251801463X.

Zivanov, J., Nakane, T., and Scheres, S.H.W. (2020). Estimation of high-order aberrations and anisotropic magnification from cryo-EM data sets in RELION-3.1. IUCrJ *7*, 253-267. 10.1107/S2052252520000081.

Acknowledgements

This has been a long journey full of surprises, some very good and some.. well… let's call them educational? But looking back to where I was 5 years ago, I feel like the PhD was a defining period of personal growth (not to be confused with maturing though) and I am immensely grateful for the opportunities to both learn and teach new stuff almost every day. First of all, I would like to thank Roland for the opportunity to join his lab as a PhD student and to work in this great environment, for advice, encouragement and insightful discussions, for believing we would eventually solve RQT even when I had my doubts. Additionally, I would like to thank Prof. Dr. Klaus Förstemann for agreeing to be my second advisor, and naturally the rest of my Thesis committee: Prof. Dr. Julian Stingele, Dr. Gregor Witte, Dr. Dietmar Martin and Prof. Dr. Karl-Peter Hopfner.
Exciting science is better when shared and with that in mind, I would like to express my thanks to Prof. Dr. Toshifumi Inada, Dr. Yoshitaka Matsuo, Dr. Niladri Sinha and Prof. Dr. Rachel Green, for collaborations on both RQT and EDF1. During the PhD I had the opportunity to join two graduate schools, QBM and Grk1721. Thank you for organizing memorable events, courses and of course for funding parts of this journey.

When I joined the lab I was amazed how many reasons one can find to celebrate together: paper-, PhD- and birthday celebrations, Thirstdays, Starkbierfest and Oktoberfest visits, kitchen parties, roof-top parties, pool-side BBQs and goodbyes. Now that it's my time to say farewell to the Beckmann Lab, I want to express my gratitude to all members of the lab, both present and past. All of you made my time here a fun one and you always managed to lift my spirits even if experiments were frustrating. Andrea, Joanna, Heidi, and most recently Alicia, you are the best technicians a lab can hope for and I learned a lot from you. You managed to make me feel like there are no stupid questions (although there probably were plenty) and always took time to explain things. Joanna, thanks to you our flat and my parents place is now home to two small, adorable monsters that love to wake you up at ungodly hours in order to pretend they have never seen food in their lives. I definitely count that as one of the very good surprises. Please never stop being the Lab-Mom, taking newer students under your wing and then surprising them with the contends of your phone (and mind). Regarding me asking (probably) stupid questions, I would also like to thank Dr. Thomas Becker and Dr. Birgitta Beatrix. I will always be grateful for your guidance during my time as a PhD student, for the roof-top coffee breaks and all the (sometimes even scientific) advice. Supervising the MuZ course with you was loads of fun. Actually, partaking in this course as a Master student set me on this path and I wouldn't have it any other way. Gitti, I am still convinced that the Gin we prepared for the BBQ was definitely the superior one. Thomas, I hope there will still be whisky evenings in the future and keep rocking! Talking about constants in the Lab, a big 'Thank you!' goes out to the EM-facility. Susi and Charlotte: you are the Cryo-Queens, keepers of samples and rescuers of grids. Thank you for patiently freezing all these RQT samples, for teaching me how to do this on my own and for fun discussions while doing so. I know we students usually bring chaos to your cryo-domain but you still suffer that intrusion regally. Dr. Otto Burninghome, you are the keeper of the microscope. Thank you for the patient explanations on how to collect data, and for rescuing me and Hanna when we kept losing the beam on Spirit. I am grateful for our discussions during the data collections and for the all the advice on (lab)life.

Sometimes you meet people and instantly hit it off. Sporadic coffee breaks turn into daily lunches, which turn into full-fledged cookouts, gin-tastings, hikes, vacations and more. Much to some people's chagrin, we often managed to fill the floor with the distinct smell of frying onions or garlic and occupied the kitchen during the lunch rush. Hanna, Lukas and Michi, I really miss our daily (lunch) shenanigans and I can't imagine a better lunch crew. Hanna, you were the first in the lab that was a good friend rather than a colleague (although the others followed shortly). I do miss our depresso sessions, the baking, the fun we had in the back-lab and the hikes, but also your input to the more scientific side of things. I still owe you a Bob-Ross paint-along evening… Michi and Lukas, thank you for whisky and 'safari' events, looking for trolls in Norway, being trolls in Norway, game-nights, birthdays, Christmas markets, bouldering… I could go on and on there, but point is, you became close friends, I am very grateful that you guys were there for me during the PhD and I am looking forward to all our future adventures. Lukas, thank you for getting back into the wet-lab business to tackle RQT with me and (I guess…) for making me the partner-in-crime in all the IT (mis-)adventures, sometimes causing, but mostly solving all sorts of IT trouble. Of course here, I also need to mention Lydi. What started as a stand-in-boulder-partnership while some people went to San Diego for 'scientific-reasons', quickly developed into the best-boulder-partnership ever, and into an off-key-singing-PUNK-very-late-at-night kind of sistership. I am still slightly upset that Basel is not closer to Munich… on the other hand, this might slow down the chicken-war a bit.

Getting back to people in the lab, I would like to thank Dr. Ken Ikeuchi for his support regarding all the RQT stuff. You were a well of information on protein purification, generation of yeast strains, ubiquitination and overall scientific expertise. I profited immensely from you joining the lab and freely sharing all your knowledge. Another very important member making the back-lab, THE back-lab is Timur. When you and Hanna were discussing things I often whished for popcorn. I will miss the sea-shanties, BBQ poem recitations, hat creation, really good 'Wichtel'-poems, the amazing cakes, the dry humor and the vest. To the newer members of the back-lab, Leona, Shuangshuang and Hanna (the younger): I hope your time there will be as much fun as mine was, but from what I have seen so far, you are more than worthy successors. Now for the people in the front-lab… well, I guess no one should be judged by having the misfortune of not being placed in the right part of the lab so a shout-out to Ivan, Cristian, Dandan, Jakub, Dr. Tesina, Rob, Matt and Timo. I am glad I could be on this journey with you. I also want to mention some more of the past members: Andre, Kadda, Alex, Aleks, Chris, Tsai, Ting, Jen, Vivek…. you introduced me to the Beckmann lab and made me feel welcome and I am glad there was an overlap in our respective journeys.

What is certainly true, is that all journeys have to end eventually. I could go on mentioning people, reminiscing about all the events and small moments defining this PhD but I will stop at this point. In the end I would like to thank my family. Mom, Dad, Daniel, Matze, I am ever grateful for your vast support and encouragement, independent of success or failures, for fostering the curiosity needed to get here, for making me feel loved. You mean the world to me. Matze, I know there were plenty of late evenings and weekend processing sessions and I am glad you put up with that. Thank you for anchoring me, for listening to the weird scientific stuff and for always having my back. I am glad that we are on this road together, let's see where this will lead next…

Appendix

Maps of the staller plasmids

>6xHis_V5_TEV_SDD1_pEX (2950 bp)

TEV-site, AmpR, V5-tag, 6x His, T7 promoter, SDD1 101-218, 3x STOP

tcgcggccgcaagctaatacgactcactataggggaccaaacaaaacaaataaaacaaaaacacaATGcatcatcatcatcatcatggcaaaccgattccgaac
ccgctgctgggcctggatagcaccgaaggtggcgaagagaatctttattttcagtccgatcaagttttaaagttacaagctacacttttttcccaatgccatactgaa
acaggttcatctcgacaatgccaacatagaaaacaagagaattctgaaggaaattacatataaataccttccaacgaaaactgtaaagaggagaacaaattcg
gaacattcatcgtaaagagaatttttttttggtgacttatcactcggggtttccgtgttaatcaaccgtattgctttcgaatcggccacatcatccattatggtagtgag
aagttcatttattgaaagtgatttcttttatgaagattatttgattttcgattgcagagcgaaacgacgaaaaaaattgaagaggaaaatttttgtttaaataaataa
aggatccgaattcctgtgtgaaattgttatccgctcacaattccacacaacatacgagccggaagcataaagtgtaaagcctggggtgcctaatgagtgagctaa
ctcacattaattgcgttgcgctcactgcccgctttccagtcgggaaacctgtcgtgccagctgcattaatgaatcggccaacgcgcggggagaggcggtttgcgta
ttgggcgctcttccgcttcctcgctcactgactcgctgcgctcggtcgttcggctgcggcgagcggtatcagctcactcaaaggcggtaatacggttatccacagaa
tcaggggataacgcaggaaagaacatgtgagcaaaaggccagcaaaaggccaggaaccgtaaaaaggccgcgttgctggcgtttttccataggctccgccccc
ctgacgagcatcacaaaaatcgacgctcaagtcagaggtggcgaaacccgacaggactataaagataccaggcgtttcccccctggaagctccctcgtgcgctct
cctgttccgaccctgccgcttaccggatacctgtccgcctttctcccttcgggaagcgtggcgctttctcatagctcacgctgtaggtatctcagttcggtgtaggtcg
ttcgctccaagctgggctgtgtgcacgaaccccccgttcagcccgaccgctgcgccttatccggtaactatcgtcttgagtccaacccggtaagacacgacttatc
gccactggcagcagccactggtaacaggattagcagagcgaggtatgtaggcggtgctacagagttcttgaagtggtggcctaactacggctacactagaagga
cagtatttggtatctgcgctctgctgaagccagttaccttcggaaaaagagttggtagctcttgatccggcaaacaaaccaccgctggtagcggtggttttttgttt
gcaagcagcagattacgcgcagaaaaaaaggatctcaagaagatcctttgatcttttctacggggtctgacgctcagtggaacgaaaactcacgttaagggattt
tggtcatgagattatcaaaaaggatcttcacctagatccttttaaattaaaaatgaagttttaaatcaatctaaagtatatatgagtaaacttggtctgacagttacc
aatgcttaatcagtgaggcacctatctcagcgatctgtctatttcgttcatccatagttgcctgactccccgtcgtgtagataactacgatacgggagggcttaccat
ctggccccagtgctgcaatgataccgcgagacccacgctcaccggctccagatttatcagcaataaaccagccagccggaagggccgagcgcagaagtggtcc
tgcaactttatccgcctccatccagtctattaattgttgccgggaagctagagtaagtagttcgccagttaatagtttgcgcaacgttgttgccattgctacaggcat
cgtggtgtcacgctcgtcgtttggtatggcttcattcagctccggttcccaacgatcaaggcgagttacatgatcccccatgttgtgcaaaaaagcggttagctcctt
cggtcctccgatcgttgtcagaagtaagttggccgcagtgttatcactcatggttatggcagcactgcataattctcttactgtcatgccatccgtaagatgcttttct
gtgactggtgagtactcaaccaagtcattctgagaatagtgtatgcggcgaccgagttgctcttgcccggcgtcaatacgggataataccgcgccacatagcaga
actttaaaagtgctcatcattggaaaacgttcttcggggcgaaaactctcaaggatcttaccgctgttgagatccagttcgatgtaacccactcgtgcacccaactg
atcttcagcatcttttactttcaccagcgtttctgggtgagcaaaaacaggaaggcaaaatgccgcaaaaaagggaataagggcgacacggaaatgttgaatac
tcatactcttcctttttcaatattattgaagcatttatcagggttattgtctcatgagcggatacatatttgaatgtatttagaaaaataaacaaataggggttccgcg
cacatttccccgaaaagtgccacctgacgtctaagaaaccattattatcatgacattaacctataaaaataggcgtatcacgaggccctttcgtctcgcgcgtttcg
gtgatgacggtgaaaacctctgacacatgcagctcccggagacggtcacagcttgtctgtaagcggatgccgggagcagacaagcccgtcagggcgcgtcagc
gggtgttggcgggtgtcggggctggcttaactatgcggcatcagagcagattgtactgagagtgcaccatatgggtaccgagc

>6xHis_V5_TEV_Rpl4A_pEX (2950 bp)

TEV-site, AmpR, V5-tag, 6x His, T7 promoter, Rpl4A 4-64, 12x CGN, 3x STOP

tcgcggccgcaagctaatacgactcactatagggaccaaacaaaacaaataaaacaaaaacacaATGcatcatcatcatcatcatggcaaaccgattccgaac
ccgctgctgggcctggatagcaccgaaggtggcgaagagaatctttattttcagtcccgtccacaagttactgttcactctttgactggtgaagctactgccaatgc
cttgccattgccagctgtcttctccgctcctatccgtccagacattgtccacactgttttcacctctgtgaacaagaacaagagacaagcttacgctgtttctgaaaa
ggctggtcaccaaacctccgctgaatcctgggaacggcgacgacggcgccgccggcgacgacggcgccgctaaataaataaaggatccgaattcctgtgtgaa
attgttaacctgcttttgctcgcttggatccgaattcaaaggtgaaattgttatccgctcacaattccacacaacatacgagccggaagcataaagtgtaaagcctg
gggtgcctaatgagtgagctaactcacattaattgcgttgcgctcactgcccgctttccagtcgggaaacctgtcgtgccagctgcattaatgaatcggccaacgc
gcggggagaggcggtttgcgtattgggcgctcttccgcttcctcgctcactgactcgctgcgctcggtcgttcggctgcggcgagcggtatcagctcactcaaagg
cggtaatacggttatccacagaatcaggggataacgcaggaaagaacatgtgagcaaaaggccagcaaaaggccaggaaccgtaaaaaggccgcgttgctg
gcgtttttccataggctccgccccccctgacgagcatcacaaaaatcgacgctcaagtcagaggtggcgaaacccgacaggactataaagataccaggcgtttcc
ccctggaagctccctcgtgcgctctcctgttccgaccctgccgcttaccggatacctgtccgcctttctcccttcgggaagcgtggcgctttctcatagctcacgctgt
aggtatctcagttcggtgtaggtcgttcgctccaagctgggctgtgtgcacgaaccccccgttcagcccgaccgctgcgccttatccggtaactatcgtcttgagtc
caacccggtaagacacgacttatcgccactggcagcagccactggtaacaggattagcagagcgaggtatgtaggcggtgctacagagttcttgaagtggtggc
ctaactacggctacactagaaggacagtatttggtatctgcgctctgctgaagccagttaccttcggaaaaagagttggtagctcttgatccggcaaacaaaccac
cgctggtagcggtggtttttttgtttgcaagcagcagattacgcgcagaaaaaaaggatctcaagaagatcctttgatcttttctacggggtctgacgctcagtgga
acgaaaactcacgttaagggattttggtcatgagattatcaaaaggatcttcacctagatccttttaaattaaaaatgaagttttaaatcaatctaaagtatatat
gagtaaacttggtctgacagttaccaatgcttaatcagtgaggcacctatctcagcgatctgtctatttcgttcatccatagttgcctgactccccgtcgtgtagata
actacgatacgggagggcttaccatctggccccagtgctgcaatgataccgcgagacccacgctcaccggctccagatttatcagcaataaaccagccagccgg
aagggccgagcgcagaagtggtcctgcaactttatccgcctccatccagtctattaattgttgccgggaagctagagtaagtagttcgccagttaatagtttgcgc
aacgttgttgccattgctacaggcatcgtggtgtcacgctcgtcgtttggtatggcttcattcagctccggttcccaacgatcaaggcgagttacatgatcccccatg
ttgtgcaaaaaagcggttagctccttcggtcctccgatcgttgtcagaagtaagttggccgcagtgttatcactcatggttatggcagcactgcataattctcttact
gtcatgccatccgtaagatgcttttctgtgactggtgagtactcaaccaagtcattctgagaatagtgtatgcggcgaccgagttgctcttgcccggcgtcaatacg
ggataataccgcgccacatagcagaactttaaaagtgctcatcattggaaaacgttcttcggggcgaaaactctcaaggatcttaccgctgttgagatccagttcg
atgtaacccactcgtgcacccaactgatcttcagcatcttttactttcaccagcgtttctgggtgagcaaaaacaggaaggcaaaatgccgcaaaaaagggaata
agggcgacacggaaatgttgaatactcatactcttccttttcaatattattgaagcatttatcagggttattgtctcatgagcggatacatatttgaatgtatttaga
aaaataaacaaatagggttccgcgcacatttccccgaaaagtgccacctgacgtctaagaaaccattattatcatgacattaacctataaaaataggcgtatca
cgaggccctttcgtctcgcgcgtttcggtgatgacggtgaaaacctctgacacatgcagctcccggagacggtcacagcttgtctgtaagcggatgccgggagca
gacaagcccgtcagggcgcgtcagcgggtgttggcgggtgtcggggctggcttaactatgcggcatcagagcagattgtactgagagtgcaccatatgggtacc
gagc

Sorting schemes RQT datasets

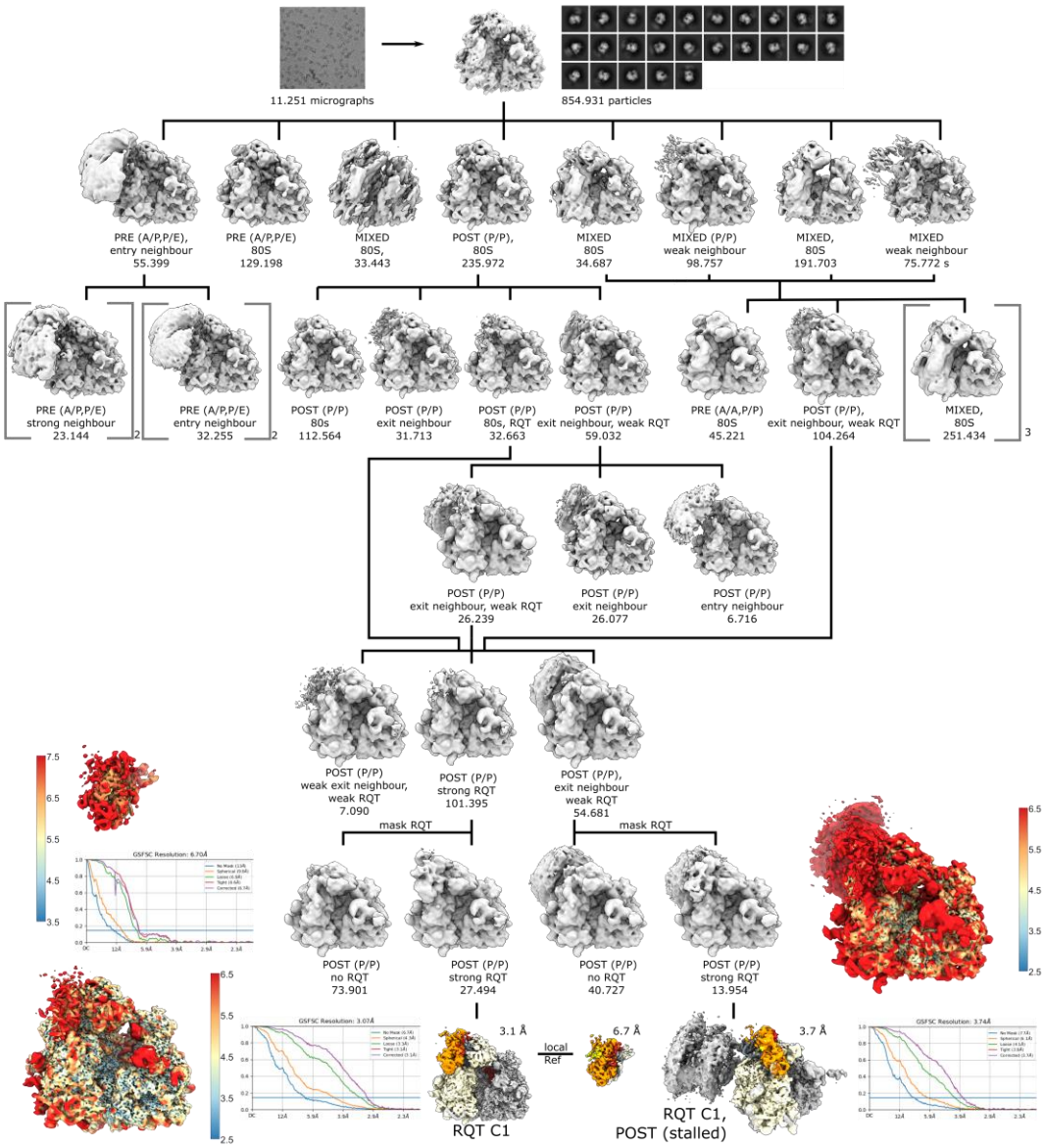

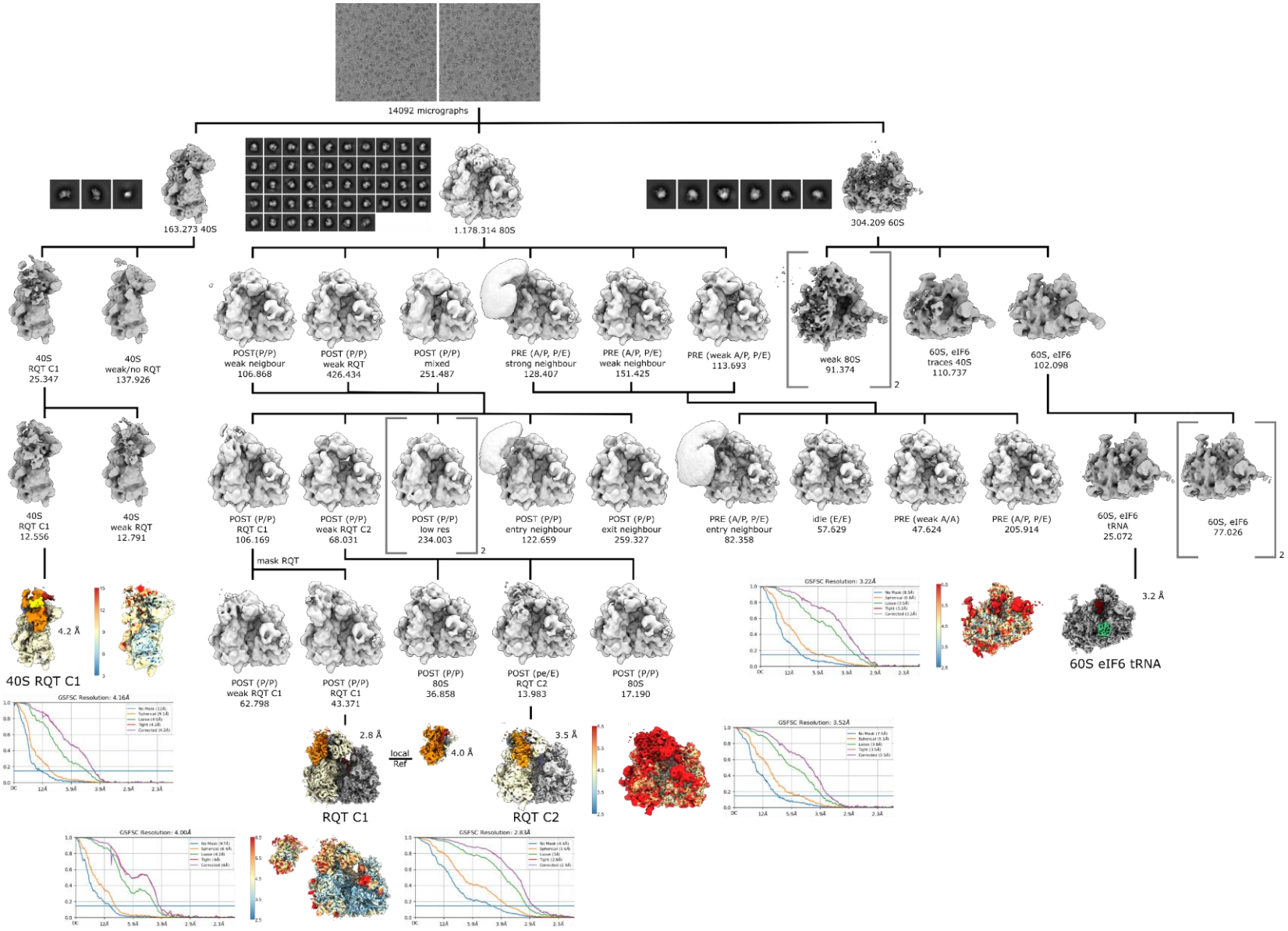
14092 micrographs
163.273 40S
1.178.314 80S
304.209 60S
40S RQT C1 25.347
40S weak/no RQT 137.926
POST(P/P) weak neigbour 106.868
POST (P/P) weak RQT 426.434
POST (P/P) mixed 251.487
PRE (A/P, P/E) strong neighbour 128.407
PRE (A/P, P/E) weak neighbour 151.425
PRE (weak A/P, P/E) 113.693
weak 80S 91.374
60S, eIF6 traces 40S 110.737
60S, eIF6 102.098
40S RQT C1 12.556
40S weak RQT 12.791
POST (P/P) RQT C1 106.169
POST (P/P) weak RQT C2 68.031
POST (P/P) low res 234.003
POST (P/P) entry neighbour 122.659
POST (P/P) exit neighbour 259.327
PRE (A/P, P/E) entry neighbour 82.358
idle (E/E) 57.629
PRE (weak A/A) 47.624
PRE (A/P, P/E) 205.914
60S, eIF6 tRNA 25.072
60S, eIF6 77.026
mask RQT
4.2 Å
40S RQT C1
POST (P/P) weak RQT C1 62.798
POST (P/P) RQT C1 43.371
POST (P/P) 80S 36.858
POST (pe/E) RQT C2 13.983
POST (P/P) 80S 17.190
2.8 Å
local Ref
4.0 Å
3.5 Å
RQT C1
RQT C2
3.2 Å
60S eIF6 tRNA

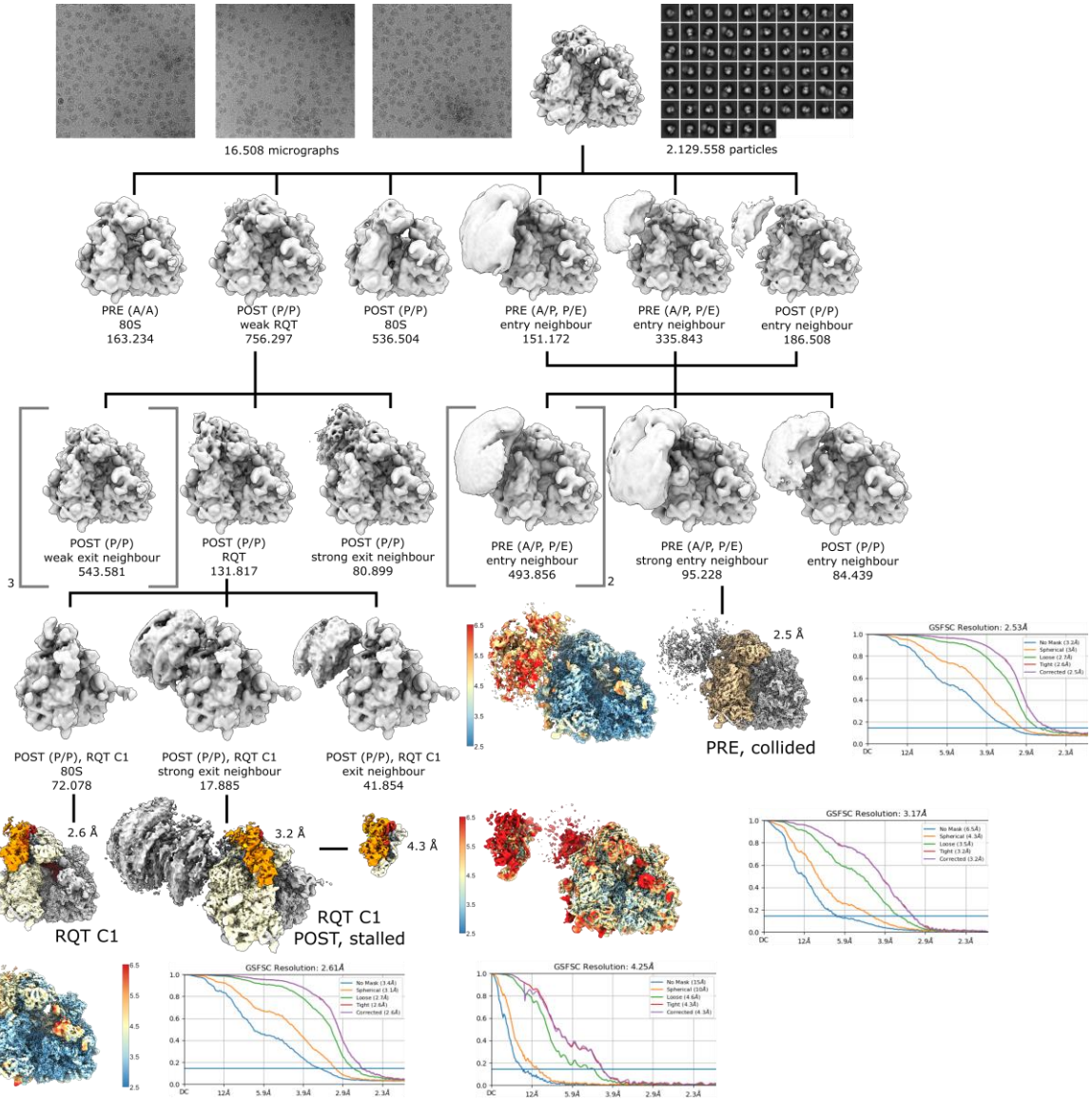
16.508 micrographs
2.129.558 particles
PRE (A/A)
80S
163.234
POST (P/P)
weak RQT
756.297
POST (P/P)
80S
536.504
PRE (A/P, P/E)
entry neighbour
151.172
PRE (A/P, P/E)
entry neighbour
335.843
POST (P/P)
entry neighbour
186.508
3
POST (P/P)
weak exit neighbour
543.581
POST (P/P)
RQT
131.817
POST (P/P)
strong exit neighbour
80.899
PRE (A/P, P/E)
entry neighbour
493.856
2
PRE (A/P, P/E)
strong entry neighbour
95.228
POST (P/P)
entry neighbour
84.439
POST (P/P), RQT C1
80S
72.078
POST (P/P), RQT C1
strong exit neighbour
17.885
POST (P/P), RQT C1
exit neighbour
41.854
2.5 Å
PRE, collided
GSFSC Resolution: 2.53Å
2.6 Å
3.2 Å
4.3 Å
RQT C1
RQT C1
POST, stalled
GSFSC Resolution: 3.17Å
GSFSC Resolution: 2.61Å
GSFSC Resolution: 4.25Å

Table cryoEM

RQT

Data collection and processing	RQTC1, PDB ID : 7ZPQ EMDB: 14861	RQTC2,PDB ID: 7ZRS, EMDB: 14921	60S,PDB ID 7ZS5, EMD-14926	RQTC1 stalled, PDB ID 7ZUW, EMD-14978	collided, PDB ID 7ZUX, EMD-14979
Camera	Gatan K2 summit	Gatan K2 summit	Gatan K2 summit	Gatan K2 summit	Gatan K2 summit
Magnification	130,000	130,000	130,000	130,000	130,000
Voltage [kV]	300	300	300	300	300
Electron exposure [e-Å-2]	43.6	43.6	46.4	44.0	44.0
Defocus range [μm]	0.5-3.0	0.5-3.0	0.5-3.0	0.5-3.0	0.5-3.0
Symetry imposed	C1	C1	C1	C1	C1
Micrographs collected	21,171	21,171	14,092	16,508	16,508
Initial particle images	2,415,630	2,415,630	304,209	2,129,558	2,129,558
Final particle images	194,186	20,380	25,072	17,885	95,228
Map resolution (80s)	2.4	3.0	3.2	3.2	2.5
FSC theshold	0.143	0.143	0.143	0.143	0.143
Map resolution (RQT)	3.5	4.8		4.3	
Refinement					
initial model used [PDB code]	6snt, alphafold	6snt, alphafold	6hd7, 6snt, 1G62	6snt, alphafold	6snt,6i7o
Model resolution	2.85	2.98	3.42	3.16	2.93
FSC threshold	0.5	0.5	0.5	0.5	0.5
Map sharpening Bfactor	-66	-40	-10	-38	-59
Model composition					
Non-hydrogen atoms	218512	218376	127849	218512	203400
Protein residues	13293	13289	6416	13293	11140
Nucleotide residues	5310	5309	3603	5310	5414
Ligands	95	13	24	95	93
R.m.s deviations					
Bond lengths	0.003	0.004	0.002	0.009	0.009
Bond angles	0.569	0.594	0.534	0.823	0.732
Validation					
Molprobity score	1.74	1.75	1.76	2.05	1.92
Clash score	8.73	9.42	12.25	15.09	12.87
Poor rotamers	0.03	0.03	0.02	0.05	0.03
Ramachandran plot					
Favored	96.10	96.21	97.12	94.74	95.72
Allowed	3.69	3.57	2.50	5.04	4.07
Disallowed	0.21	0.21	0.38	0.21	0.21

Mbf1

	EDF1-ribosome PDB 6ZVH EMDB:11456	Mbf1-ribosome PDB 6ZVI EMDB:11457
Ribosomal state	Post State	Rotated state
Microscope	FEI Titan Krios	FEI Titan Krios
Camera	Gatan K2 summit	Gatan K2 summit
Voltage (kV)	300	300
Pixel size (Å)	1.059	1.059
Electron dose (e-/Å^2)	42	42
Defocus range (μm)	0.5 - 2.5	0.5 - 2.5
Particles after 2D (no.)	95832	398371
Final particles (no.)	81976	57350
Model Composition		
Protein residues	5074	4918
RNA bases	1815	1946
Resolution (Å)	2.9	3.0
FSC threshold	0.143	0.143
Map CC	0.88	0.84
Map sharpening B-factor (Å^2)	-20	-30
RMS Deviations		
Bond lengths (Å)	0.008	0.007
Bond angles (°)	0.945	0.969
Validation		
MolProbity score	1.67	1.69
Clashscore	5.79	5.92
Poor rotamers (%)	0.00	0.02
Ramachandran Plot		
Disallowed (%)	0.18	0.21
Allowed (%)	4.88	5.16
Favored (%)	94.94	94.64

List of plasmids and strains

***S.Cerevisiae* strains**		
ski2Δ uS10-3HA	MATa ade2 his3 leu2 trp1 ura3 can1 ski2Δ::kanMX4 uS10-3HA::HISMX6	Matsuo *et al*. (2020)
xrn1Δ, slh1Δ, cue2Δ	MATa his3Δ1 leu2Δ0 met15Δ0 ura3Δ0 can1Δ::STE2pr-his5+ lyp1Δ xrn1Δ::kanMX cue2::NatMX4 slh1::hphMX6 ade2::RFP_Pgal_GFP-2A-FLHIS3-CGA12-HIS3_MET17	D'Orazio *et al*. (2019)
Cell line (*H.sapiens*)		
HEK293-Flp-In T-REx-3xFLAG-3C-EDF1	HEK293-Flp-In T-Rex co-transfected with pcDNA5-FRT-tetO-3xFLAG-3C-EDF1 and pOG44 Flp-recombinase expression vectors, and selected with hygromycin.	(Sinha *et al.*, 2020)
Plasmids		
p415GPD-Hel2-Flag	CEN, LEU2, GPD promoter, HEL2-FLAG	Matsuo *et al*. (2017)
p425GAL-Rqt2-FTP	2μ, LEU2, GAL1 promoter, RQT2-FTP	Matsuo *et al*. (2020)
p425GAL-Rqt2K316R-FTP	2μ, LEU2, GAL1 promoter, RQT2K316R-FTP	Matsuo *et al*. (2020)
p424GAL-Rqt3	2μ, TRP1, GAL1 promoter, RQT3	Matsuo *et al*. (2020)
p426GAL-Rqt4	2μ, URA3, GAL1 promoter, RQT4	Matsuo *et al*. (2020)
p7XC3GH-eIF6	pET26b, CmR, KanR, T7 promoter,eIF6-3D-GFP-10xHis	Wells *et al*. (2020)
pGEX-UBC4	pGEX, AmpR, tac promoter, GST-3C-UBC4	Ikeuchi *et al*. (2019)
pEX-His-v5-Rpl4a-CGN12	pEX, AmpR, T7 promoter, 6xHis-V5-TEV-Rpl4A 4-64-CGN12	(Best *et al*., 2022)
pEX-His-v5-Rpl4a-SDD1	pEX, AmpR, T7 promoter, 6xHis-V5-TEV-SDD1 101-218	Matsuo *et al*. (2020)
p425GAL-Rqt2K316R-FTP	2μ, LEU2, GAL1 promoter, RQT2K316R-FTP	Matsuo *et al*. (2017)
p425GAL-Rqt2E428Q-FTP	2μ, LEU2, GAL1 promoter, RQT2E428Q-FTP	This thesis
p425GAL-Rqt2E1267Q-FTP	2μ, LEU2, GAL1 promoter, RQT2E1267Q-FTP	This thesis
p425GAL-Rqt2D1266E-FTP	2μ, LEU2, GAL1 promoter, RQT2D1266E-FTP	This thesis
p425GAL-Rqt2K1168R-FTP	2μ, LEU2, GAL1 promoter, RQT2K1168R-FTP	This thesis